Environmental Effects on the ISM of Star-Forming Galaxies

The Effects of Environment on the Atomic and Molecular Gas Properties of Star-Forming Galaxies

By

Angus King Fai Mok, M. Sc., B. Sc.

A Thesis

Submitted to the School of Graduate Studies

in Partial Fulfilment of the Requirements

for the Degree

Doctor of Philospophy

McMaster University

DOCTOR OF PHILOSPOPHY (2017) McMaster University

(Physics and Astronomy) Hamilton, Ontario

TITLE: The Effects of Environment on the Atomic and Molecular Gas Properties of Star-Forming Galaxies

AUTHOR: Angus Mok, M. Sc., B. Sc. (University of Waterloo)

SUPERVISORS: Christine Wilson

NUMBER OF PAGES: xx, 201

Abstract

Where a galaxy is located has a strong effect on its properties. The dense cluster environment is home to a large population of red, quiescent elliptical galaxies, whereas blue, star-forming, spiral galaxies are common in lower-density environments. This difference is intricately linked to the ability of the galaxy to form new stars and therefore ultimately to the fuel for star formation, the atomic and molecular gas. In this thesis, I use two large JCMT surveys to explore the effects of environment on the atomic gas, molecular gas, and star formation properties of a large sample of nearby gas-rich galaxies.

From the NGLS and follow-up studies, I select a sub-sample of 98 H I-flux selected spiral galaxies. I measure their total molecular gas mass using the CO $J = 3 - 2$ line and combine this data with measurements of their total atomic gas mass using the 21-cm line and star formation rate using attenuation-corrected Hα luminosity. I find an enhancement in the mean H_2 mass and a higher H_2-to-H I ratio for the Virgo Cluster sample. Virgo Cluster galaxies also have longer molecular gas depletion times (H_2/SFR), which suggests that they are forming stars at a lower rate relative to their molecular gas reservoirs than non-Virgo galaxies.

Next, I collect VLA 21 cm line maps from the VIVA survey and follow-up VLA studies of selected galaxies in the NGLS. I measure the surface density maps of the atomic gas, molecular gas, and star formation rate in order to determine radial trends. I find that the H_2 distribution is enhanced near the centre for Virgo Cluster galaxies, along with a steeper total gas (H I + H_2) radial profile. I suggest that this is due to the effects of moderate ram pres-

sure stripping, which would strip away low-density gas in the outskirts while enhancing high-density gas near the centre. There are no trends with radius for the molecular gas depletion times, but the longer depletion times for the Virgo Cluster sample is still present.

Finally, I use 850 μm continuum observations for 105 star-forming galaxies and CO $J = 2 - 1$ line observations for 35 galaxies in the initial data release (DR1) of the JINGLE survey. I match the JINGLE galaxies to a SDSS group catalogue and measure environmental parameters such as the host halo mass, environment density, and location in phase space. I find that the molecular gas masses estimated from the 850 μm and CO $J = 2 - 1$ line observations are well-correlated. The H_2-to-H I ratio and the molecular gas depletion times do not appear to vary with stellar mass. I did not find any significant variation with environment in the DR1 sample, but I will apply this framework to the full JINGLE sample once the complete dataset is available.

Acknowledgements

I would like to acknowledge all the friends, co-workers, and family members who have helped and supported me throughout this process. I appreciate the many contributions from the supervisory committee, including Laura Parker, James Wadsley, and my PhD advisor, Christine Wilson. Thanks especially to Dr. Wilson, who is always patient, helpful, and meticulous in correcting mistakes.

Also invaluable to the process is the hard work and tireless effort made by the many members of scientific collaborations, working to reveal the mysteries of the Universe, including VIVA, NGLS, JINGLE, and many others. Finally, this work would not be possible without the people who built and operate these wonderful telescopes and the generosity of the public who fund and support the quest for the acquisition of new knowledge.

Co-Authorship

In this thesis, Chapter 2, 3, 4 contains original research and results written by Angus Mok. This includes Chapter 2 and Chapter 3, which has been published in the peer-reviewed journal Monthly Notices of the Royal Astronomical Society (MNRAS). Chapter 4 is a paper which has not yet been submitted.

Chapter 2 has been published in the peer-reviewed journal Monthly Notices of the Royal Astronomical Society (MNRAS). The reference is presented here: Angus Mok, C. D. Wilson, J. Golding, B. E. Warren, F. P. Israel, S. Serjeant, J. H. Knapen, J. R. Sánchez-Gallego, P. Barmby, G. J. Bendo, E. Rosolowsky, and P. van der Werf, MNRAS, 2016, 456, 4384.

The first and second authors are myself and my PhD supervisor, Dr. Christine Wilson. J. Golding performed some initial data-reduction and analysis on the NGLS sample data. B. E. Warren wrote a VLA H I proposal for NGLS galaxies. J. H. Knapen and J. R. Sánchez-Gallego provided the Hα maps used for the star formation rate analysis and comments and suggestions on the draft of the paper. The remaining authors are part of the NGLS team and provided comments and suggestions on the draft of the paper.

Chapter 3 has been published in the peer-reviewed journal MNRAS. The reference is presented here: Angus Mok, C. D. Wilson, J. H. Knapen, J. R. Sánchez-Gallego, E. Brinks, and E. Rosolowsky, MNRAS, 2017, 467, 4282.

The first and second authors are myself and my PhD supervisor, Dr. Christine Wilson. J. H. Knapen and J. R. Sánchez-Gallego provided the Hα maps used for the star formation rate analysis and comments and suggestions on the draft of the paper. The remaining authors are part of the NGLS team and provided comments and suggestions on the draft of the paper.

Chapter 4 is written in preparation to be submitted to MNRAS. At this time, the first and second authors are myself and my PhD supervisor, Dr. Christine Wilson. The remaining authors will be made up of the JINGLE collaboration, in accordance to the guidelines set out by the team. They will likely provide comments and suggestions on the draft of the paper.

Finally, I grant an irrevocable, non-exclusive license to McMaster University and the National Library of Canada to reproduce this material as part of this thesis.

List of Abbreviations

ALFALFA – Arecibo Legacy Fast ALFA survey

CAAPR – Comprehensive Adjustable Aperture Photometry Routine

CMB – Cosmic Microwave Background

CO – Carbon Monoxide

COLD GASS – CO Legacy Database for Galex Arecibo SDSS Survey

GMC – Giant Molecular Cloud

Jy – Jansky (Units of flux density [10^{-23} ergs m^{-2} Hz^{-1}])

K-S – Kolmogorov-Smirnov (Test)

H I – Atomic Hydrogen

H_2 – Molecular Hydrogen

H-ATLAS – Herschel-Astrophysical Terahertz Large Area Survey

HeViCS – Herschel Virgo Cluster Survey

HRS – Herschel Reference Survey

IMF – Initial Mass Function

ISM – Interstellar Medium

JINGLE – The JCMT dust and gas In Nearby Galaxies Legacy Exploration (Survey)

M_* – Stellar Mass (of a Galaxy)

MAGPHYS – Multi-wavelength Analysis of Galaxy Physical Properties

MaNGA – Mapping Nearby Galaxies at APO

MNRAS – Monthly Notices of the Royal Astronomical Society

NGLS – Nearby Galaxies Legacy Survey

SAMI – Sydney-Australian-Astronomical-Observatory Multi-object Integral-

Field Spectrograph (Survey)

SFR – Star Formation Rate

sSFR – Specific Star Formation Rate (Star Formation Rate / Stellar Mass)

VIVA – VLA Imaging of Virgo in Atomic gas (VIVA)

VLA – Jansky Very Large Array

Table of Contents

List of Figures

List of Tables

Chapter 1

Introduction

According to the Lambda-Cold Dark Matter (ΛCDM) model, named for its two dominant components, the Universe at the present day consists of a mixture of radiation, baryonic matter, dark matter, and dark energy (Ryden, 2003; Carroll & Ostlie, 2006). The mysterious dark energy, which is responsible for the accelerated expansion of the Universe, is usually parametrized in this model as a cosmological constant (Λ).

The main parameters of this model have been measured to great precision with experiments such as the Wilkinson Microwave Anisotropy Probe (WMAP) (Komatsu et al., 2009) and the Planck satellite (Planck Collaboration et al., 2016). Their results show that $\sim 70\%$ of the mass-energy density in the present day Universe is in the form of mysterious 'dark energy' and the remaining $\sim 30\%$ in the form of matter. Furthermore, 'normal' baryonic matter makes up roughly a sixth of the total matter content in the Universe, with the rest in the form of 'dark matter', which does not emit electromagnetic radiation that we can detect.

Under the ΛCDM model, gravitationally-bound structures called haloes are formed hierarchically from the merger of smaller haloes. Dark matter, which dominates the process of gravitational collapse, cannot be detected directly using their electromagnetic radiation. Gravitational lensing, which measures the bending of light from background objects due to gravity, can provide an accurate measurement of the dark matter distributions in nearby galaxies and clusters (Refregier, 2003; Treu, 2010). Alternatively, astronomers have looked at the baryonic component, and in particular the luminous stars, to trace out these haloes. We call this luminous counterpart a galaxy and they are a key area of study for many fields of astronomy. For example, galaxies have been used historically to infer the existence of dark matter from their rotational velocities (Rubin et al., 1980) or from their movements inside the Coma Cluster (Zwicky, 1937).

Galaxies are plentiful in the Universe and range widely in terms of size, shape, composition, and other properties. The original method of classifying galaxies came from the seminal work by Edwin Hubble. After discovering that galaxies were exterior to our own Milky Way Galaxy, he created the Hubble sequence (or the Hubble tuning fork diagram) to organize the observed variety of spiral, elliptical, and irregular galaxies (Hubble, 1926). Figure 1.1 compiles sample optical images of galaxies along the sequence from the Hubble Space Telescope, showing the great diversity in their morphology and appearance.

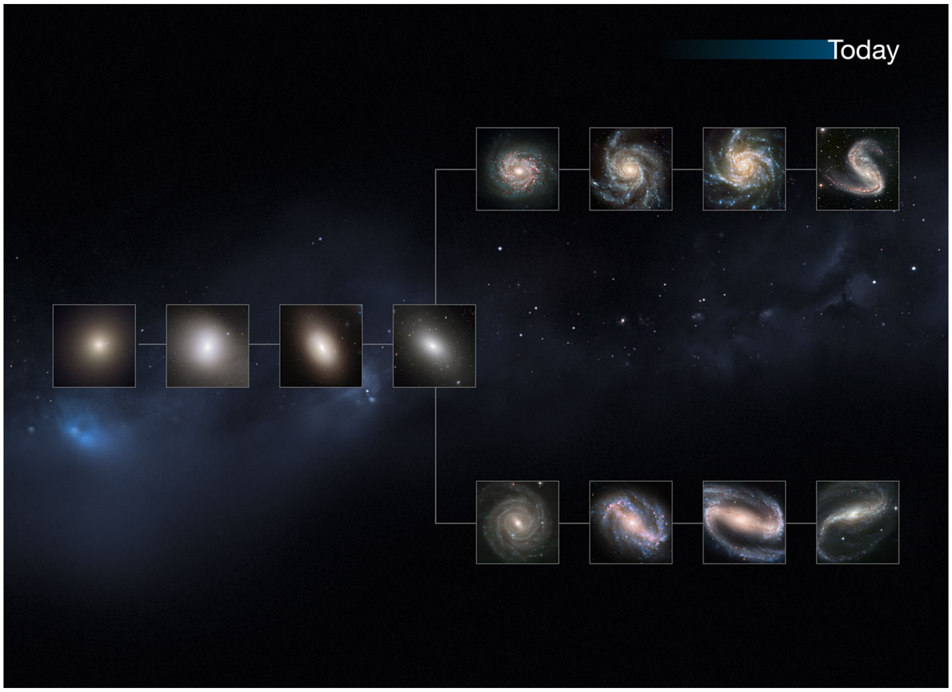

Figure 1.1 Example of galaxies along the Hubble sequence, also known as the Hubble tuning fork. Optical images were taken using the Hubble Space Telescope (HST). Image courtesy of NASA, ESA, and M. Kornmesser. Original file can be found at: *https://www.spacetelescope.org/images/heic1315b/*.

Although his proposal for an evolutionary sequence proved to be incorrect, we still classify galaxies into morphological types according to his original diagram. Some of the terminology that continues to be used today are the terms 'late-type' for spirals and 'early-type' for ellipticals. Furthermore, the correlation between morphology and other galaxy properties, such as star formation rate, gas content, and stellar mass, remains an area of ongoing research.

The advent of systematic redshift surveys of galaxies in the late 1990s and early 2000s opened up a valuable new window into the nature of galaxies and their evolution. Studies such as the Two Degree Field (2dF) Galaxy Redshift Survey (e.g. Cross et al., 2001; Colless et al., 2001) and the Sloan Digital

Sky Survey (SDSS) (e.g. York et al., 2000) have collected multi-wavelength photometry and spectroscopy for millions of individual galaxies, mapping the large scale structure of the Universe and providing a large statistical sample of galaxies to constrain theoretical models of galaxy structure and their evolution.

The properties of galaxies evolve greatly with time, from the birth of the first galaxies at a redshift of $z \gtrsim 11$ (Oesch et al., 2016), to the sample of familiar galaxies found in the local Universe. The cosmic star formation rate density peaked at $z \sim 2$ and has been declining ever since (Cucciati et al., 2012; Madau & Dickinson, 2014). Inside galaxy clusters, there has also been a strong increase in the fraction of red galaxies and a corresponding decrease in the fraction of blue galaxies since $z \sim 0.5$ (Butcher & Oemler, 1984). Molecular gas observations of high redshift normal star-forming galaxies ($z \sim 1-3$) show a similar molecular gas-star formation rate correlation as nearby galaxies, but with a significant decrease in their molecular gas depletion times (Genzel et al., 2010). Herschel observations of a large sample of galaxies up to $z \sim 2.5$ have also found that high-redshift galaxies at the same stellar mass possess higher star formation rates and are forming stars more efficiently than present day galaxies (Santini et al., 2014). In addition, because of the tight correlation between dust mass and star formation rate, high-redshift galaxies also possess higher dust masses.

In a thorough review of recent observations of nearby galaxies by Blanton & Moustakas (2009), galaxies can span a wide range of environments and properties. Their masses range from small dwarf galaxies to normal spiral galaxies to enormous galaxies that live at the centre of clusters. Colour-magnitude dia-

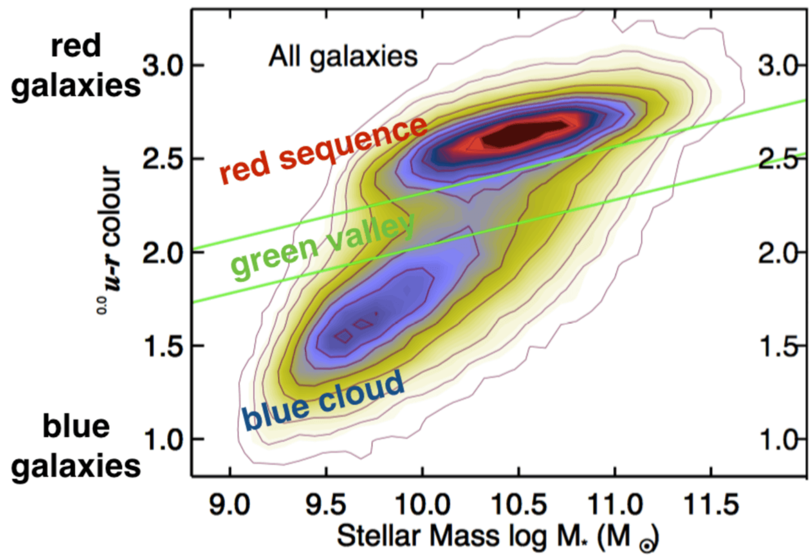

Figure 1.2 SDSS Galaxies in a colour-stellar mass plot (Schawinski et al., 2014). The location of the blue cloud, green valley, and red sequence locations are labelled. Figure released under a CC BY-ND license and the original file can be found at: *https://theconversation.com/is-our-milky-way-galaxy-a-zombie-already-dead-and-we-dont-know-it-52732*.

grams (e.g Bell et al., 2003) and spectroscopic measurements (e.g Brinchmann et al., 2004) have shown that galaxies are separated into two main populations, a 'red sequence' of quiescent, non star-forming galaxies and a 'blue cloud' of actively star-forming galaxies. There is a smaller population between the two main peaks commonly referred to as the 'green valley'. The location of these populations of galaxies on a colour-stellar mass plot is shown in Figure 1.2 (Schawinski et al., 2014). These categories are also well-correlated with their morphology, with the red sequence dominated by ellipticals and the blue cloud by spiral galaxies (Blanton & Moustakas, 2009).

Analysis of the properties of this star-forming population has also revealed the existence of a 'star-forming main sequence', where most star-forming galaxies live in the stellar mass-star formation rate plane (e.g Noeske et al., 2007; Whitaker et al., 2012). It is likely that the transition from the actively star-forming phase to the quiescent phase could explain the overall decline in the cosmic star formation rate from $z \sim 2$ to the present.

On top of the general evolution with redshift, it is also observed that this transition is strongly affected by the galaxy's environment. Dressler (e.g 1980) showed that denser environments tend to have an increasing percentage of elliptical or lenticular (also known as S0) galaxies and a lower proportion of spiral galaxies compared to the general field population. SDSS-derived stellar mass functions also show this systematic trend between early- and late-type galaxies in isolated, group, and cluster environments (Blanton & Moustakas, 2009). Why and how this 'quenching' process occurs, as well as its variations with the environment of a galaxy, is important to the understanding of the overall process of galaxy evolution.

Theoretical models have tried separate the evolution due to factors within the galaxy ('mass quenching') and evolution due to external factors ('environment quenching') (Peng et al., 2010). Some examples of internal quenching processes include the presence of a supermassive black holes (Somerville et al., 2008) and the transition to a bulge dominated system (Bell et al., 2012). In this analysis, we seek to create a sample of normal star-forming spiral galaxies to measure the effects of the environmental component.

However, any analysis based solely on the stellar component will miss one key ingredient. Stars are born from gravitational collapse inside giant clouds of molecular hydrogen, with contributions from helium and heavier elements. In a normal spiral galaxy, such as the Milky Way, the molecular gas component is concentrated near the galactic centre, with an exponential profile which declines sharply outside the solar radius (Tielens, 2005). Conversely, the more diffuse Interstellar Medium (ISM) in the atomic form can extend to much greater distances and hence be more easily affected by any environmental processes (Fumagalli & Gavazzi, 2008; Bekki, 2014). Ultimately, both of these components must be important to the process of star formation, as the molecular gas content can be continually replenished by the larger atomic gas reservoir in the host galaxy.

1.1 Observations of the Star Formation Process in Nearby Galaxies

In order to study the star formation process, we will need careful measurements of both the star formation rate and the multiple components of the ISM in nearby galaxies.

1.1.1 Star Formation Rate Observations

There are multiple ways to measure the star formation rate inside galaxies, which are thoroughly outlined in a comprehensive review by Kennicutt & Evans (2012), an updated version of the earlier review by Kennicutt (1998).

Astronomers often use star formation indicators (or tracers) to measure star formation rates, as stars can take millions of years to form. Three common indicators for nearby galaxies include measurements of their ultraviolet (UV) luminosity, infrared (IR) luminosity, and the strength of their emission lines.

UV emission comes from the photosphere of young stars and is a direct measurement of star formation rate over the past ~ 10 Myr, with minor contributions from stellar populations up to an age of 100 Myr (Kennicutt & Evans, 2012). The launch of the Galaxy Evolution Explorer (GALEX) UV satellite has made possible efficient measurements of a large number of nearby galaxies. For example, the Nearby Galaxies Survey (NGS) obtained detailed maps and UV surface density profiles for over 1000 nearby galaxies (Gil de Paz et al., 2007). The main drawback to the use of UV is the effect of dust attenuation, which requires a correction term or combining the UV measurements with infrared emission from the same object.

Infrared emission is largely due to dust attenuation, where dust particles in the ISM absorb shorter-wavelength UV and optical light and re-emit it in the form of longer wavelength infrared photons. Since the UV and IR are closely linked, infrared-based star formation rate indicators also measure the star formation rate over a similar timescale (Kennicutt & Evans, 2012). Analyses of the dust spectral energy distribution (SED) in nearby galaxies have provided calibrated star formation rate indicators using the mid-infrared (MIR) bands, such as the 24 μm band measured by the Spitzer Space Telescope, with a spread around the mean value of up to a factor of 2 (Calzetti et al., 2007). The far-infrared (FIR) bands, such as the 70 μm and 160 μm bands measured by the Herschel Space Observatory, can also be used, but with a 25% increased scatter due to the contribution from heating due to the older stellar populations (Calzetti et al., 2010). Updated formulas for the conversion between MIR/FIR luminosity and the total infrared luminosity are provided in Galametz et al. (2013).

Infrared space telescopes, such as Spitzer and Herschel, have opened up new windows into the star formation process. For example, a large Herschel survey measured the star formation rates for objects in the Great Observatories Origins Deep Survey (GOODS) fields, which include thousands of star-forming galaxies from $0 < z < 2.5$ (Elbaz et al., 2011). The Spitzer Infrared Telescope Nearby Galaxies Survey (SINGS) measured infrared photometry and spectroscopy of 75 nearby galaxies (Kennicutt et al., 2003). The drawbacks to the use of IR as a star formation indicator include the missing flux from the percentage of UV light not absorbed by dust (the main reason why UV and IR indicators are often combined together), infrared emission from old stars, and the dependence of IR emission with metallicity and the dust content of the host galaxy (Kennicutt & Evans, 2012). One common prescription which combines together FUV and total infrared (TIR) emission is found in Hao et al. (2011):

$$\mathrm{L(FUV_{corr})}\ [\mathrm{erg\ s^{-1}}] = \mathrm{L(FUV)}\ [\mathrm{erg\ s^{-1}}] + (0.46 \pm 0.12) \times \mathrm{L(TIR)}\ [\mathrm{erg\ s^{-1}}] \tag{1.1}$$

Another common star formation indicator is the strength of emission lines from the ionized gas around young stars. In nearby galaxies, Hα is the line that is most often used. Hα is an electronic transition of hydrogen from the $n = 3$

to the $n = 2$ levels. The photon is emitted at a wavelength of 656.3 nm, and can be observed using optical telescopes. Since only the most massive stars produce radiation which can ionize hydrogen gas and these massive stars are very short-lived, this star formation rate indicator measures a shorter timescale of ~ 10 Myr (Kennicutt & Evans, 2012). Some drawbacks to the use of the Hα line include the presence of [N II] line contamination (654.8 nm and 658.4 nm) and the necessity of correcting for dust attenuation (Sánchez-Gallego et al., 2012). One important survey of Hα in nearby galaxies is the Hα3 survey by Gavazzi et al. (2012), which looked at a sample of more than 400 galaxies from the HI Arecibo Legacy Fast ALFA Survey (ALFALFA). We can use the prescription of Kennicutt et al. (2009) to convert to star formation rate, which assumes a Kroupa IMF (Kroupa & Weidner, 2003):

$$\mathrm{SFR}\ [\mathrm{M}_\odot\ \mathrm{yr}^{-1}] = 5.5 \times 10^{-42}\ \mathrm{L(H}\alpha)\ [\mathrm{erg\ s}^{-1}] \tag{1.2}$$

These three star formation indicators for nearby galaxies measure different processes and have different advantages and disadvantages. However, each has been carefully calibrated and is widely used for extra-galactic research (Kennicutt & Evans, 2012). A complementary method of using the available multi-wavelength data is the technique of Spectral Energy Distribution (SED) fitting, which is summarized in the review by Walcher et al. (2011). These models attempt to match the data available for a galaxy, including UV and IR bands, to model SEDs and derive the physical properties of the object.

1.1.2 Atomic Gas Observations

Measurements of the ISM components important to the process of star formation include atomic gas, molecular gas, and dust. The atomic gas component is the easiest to measure and can be directly observed using the hyperfine transition of atomic hydrogen. Located at a frequency of 1.420 GHz (or a wavelength of ~ 21 cm), the line is unaffected by dust attenuation and can be observed using ground-based radio telescopes. Detected first in the early 1950s (Muller & Oort, 1951), the 21 cm line has been used to create detailed pictures of the cold gas distribution inside the Milky Way and local spiral galaxies. One caveat is that at column densities of greater than 10^{21} cm^{-1}, the line could become optically thick, such as in dense clouds or at low galactic latitudes (Dickey & Lockman, 1990). For most galaxies, we can convert observed intensity of the 21 cm line into mass using a relation from Draine (2011), where z is the redshift, $\mathrm{D_L}$ is the luminosiy distance is in units of megaparsecs, and $\int \mathrm{S}_\nu \mathrm{dv}$ is the H I integrated intensity in units of Jansky km s^{-1}:

$$\mathrm{M(H\,I)}\ [\mathrm{M}_\odot] = 2.343 \times 10^5 (1+\mathrm{z})^{-1}\, \mathrm{D_L^2} \int \mathrm{S}_\nu \mathrm{dv} \tag{1.3}$$

An important large scale survey is the Arecibo Legacy Fast ALFA Survey (ALFALFA), which aimed to map over 7000 square degrees of the sky using the Arecibo radio telescope (Giovanelli et al., 2005). There are also many follow-up studies that use ALFALFA data, including looking at very gas-rich galaxies in HIghMass (Huang et al., 2014) and nearby galaxies in the GALEX Arecibo SDSS Survey (GASS) (Catinella et al., 2010). Smaller scale H I surveys using high resolution radio interferometers like the Karl G. Jansky Very Large Array (VLA), include the H I Nearby Galaxy Survey (THINGS), which looked at over

34 objects within 15 megaparsecs (Walter et al., 2008) and the VLA Imaging of Virgo in Atomic Gas (VIVA), which compiled VLA observations for 53 Virgo galaxies (Chung et al., 2009).

1.1.3 Molecular Gas Observations

Detection of molecular gas has been more difficult compared to the atomic gas. The dominant molecular species in molecular clouds is H_2, which is a symmetric molecule with no permanent dipole moment and only weak rotational quadrupole transitions. The lowest allowed rotational $J = 2-0$ line, at a wavelength of 28.2 μm, requires an excitation temperature of 510 Kelvins (Tielens, 2005). The lowest vibrational transitions of the H_2 molecular have excitation temperatures of $\sim$ 3000 Kelvins (Wolfire & Konigl, 1991). These high temperatures are common in shocks and other extreme environments, but rare inside normal cold molecular clouds conditions of $\sim$ 10 Kelvins (Tielens, 2005).

As a result, astronomers have often used carbon monoxide (CO) as a key tracer of the molecular gas component. It is a common molecule in molecular clouds, with H_2/CO ratios of between $10^4 - 10^5$ (Tielens, 2005). Carbon monoxide also possesses a ladder of rotational transition lines with excitation temperatures comparable to physical conditions inside of these clouds. As a result, CO is often used as a mass tracer, when combined with an appropriate CO-to-H_2 conversion factor (Bolatto et al., 2013). Astronomers often use the lowest energy transition for this purpose, CO $J = 1 - 0$, which emits photons at a frequency of 115 GHz or a wavelength of 2.6 mm. The formula to convert CO luminosity to molecular mass, after a 36% correction factor for the presence of helium and heavier elements (Bolatto et al., 2013), is presented here:

$$\mathrm{M(H_2)\ [M_\odot]} = \alpha_{\mathrm{CO}} \mathrm{L_{CO}} = 4.3 \times \mathrm{L_{CO}\ [K\ km\ s^{-1}\ pc^{-2}]} \tag{1.4}$$

In this case, α_{CO} is the conversion factor between molecular mass and luminosity, with units of $\mathrm{M_\odot}$ $(\mathrm{K\ km\ s^{-1}\ pc^{-2}})^{-1}$. This straightforward formula is applicable because most molecular gas inside galaxies is found in gravitationally bound structures called giant molecular clouds. These virialized clouds are observed to follow a size-linewidth relation (Larson, 1981), which leads to a linear relationship between luminosity and mass.

The general uncertainty for this conversion factor from Bolatto et al. (2013) is 0.3 dex (or a factor of ~ 2) for normal star-forming galaxies. This conversion factor can vary for objects with different physical conditions, including temperature, surface densities, and metallicities. For example, starburst galaxies may have a lower conversion factor of ~ 0.8 $\mathrm{M_\odot}$ $(\mathrm{K\ km\ s^{-1}\ pc^{-2}})^{-1}$ (Downes & Solomon, 1998). In this thesis, we consider only nearby star-forming spiral galaxies and thus do not expect any systematic differences in the conversion factor. Although the scatter is larger than the usual instrumental or calibration uncertainties, the use of a large sample of galaxies will allow us determine trends within our sample, such as in the mean properties of selected subsamples.

For extra-galactic objects, $\mathrm{L_{CO}}$ can be found using the following formula from Solomon & Vanden Bout (2005), where $\mathrm{S_{CO}\Delta v}$ is the integrated CO line flux density in Jansky km s^{-1} and D_L is the luminosity distance in units of megaparsecs:

$$L_{CO}\ [\mathrm{K\ km\ s^{-1}\ pc^{-2}}] = 2453 \int S_{CO} \Delta v\ D_L^2\ (1+z)^{-1} \tag{1.5}$$

Despite enormous advances in sub-mm telescope technology, efficient line measurements of large numbers of extragalactic objects remain difficult and time consuming. Consequently, previous work has often focused on clouds inside the Milky Way or very small number of galaxies (especially compared to similar optical surveys).

One of the earliest Milky Way surveys was the Massachusetts-Stony Brook Galactic CO Survey using the Five College Radio Astronomy Observatory (FCRAO) (Scoville et al., 1987). The group mapped out most of the CO emission regions in the first quadrant (galactic longitude of between 0 and 90 degrees) of the Milky Way. Heyer et al. (1998) performed a similar survey of the outer Galaxy using the same FCRAO array. The first full Galactic plane survey, in a strip up to 10 degrees wide using the CfA 1.2 m telescope, provided a beautiful and complete view of the molecular gas distribution in the Milky Way (Dame et al., 2001). These surveys mapped the distribution of giant molecular clouds in the sky and constrained many of their properties, including the column density and the CO-to-H_2 conversion factor.

The first large survey of the molecular gas in nearby galaxies also came from FCRAO, with the FCRAO Extragalactic CO Survey of 300 galaxies. The dataset showed interesting trends between CO-to-optical diameters and morphology (Young et al., 1995). Next, the Berkeley-Illinois-Maryland Association (BIMA) Survey of Nearby Galaxies (BIMA-SONG) observed 44 galaxies in the CO $J = 1 - 0$ line at much higher angular resolution and measured their radial profiles, finding that they can be well-fitted with an exponential function (Regan et al., 2001).

More recent surveys have greatly expanded both the number of galaxies observed and the quality of the data, including sensitivity and spatial resolution. Examples of large single-pointing samples include the CO Legacy Database for the GASS Survey (COLD GASS) (Saintonge et al., 2011a,b) and the CO portion of the Herschel Reference Survey (HRS) (Boselli et al., 2010, 2014a). COLD GASS observed the CO $J = 1 - 0$ line for 350 galaxies using the IRAM 30 metre telescope. HRS compiled archival and new observations to obtain a sample of 225 galaxies. These surveys have greatly improved our understanding of the ISM and star formation process by measuring important scaling relationships and the close link between molecular gas and star formation. For example, COLD GASS found strong correlations of the molecular gas depletion time with both stellar mass and the specific star formation rate (sSFR) (Saintonge et al., 2011b). The specific star formation rate (sSFR) is the star formation rate of a galaxy divided by its stellar mass. For galaxies in the HRS, the gas content of a galaxy has a strong dependence on its morphological type and sSFR (Boselli et al., 2014b).

Surveys that resolve individual galaxies include the Nearby Galaxies Legacy Survey (NGLS) (Wilson et al., 2009, 2012), the HERA CO Line Extragalactic Survey (HERACLES) (Bigiel et al., 2008; Leroy et al., 2008), and the EDGE-CALIFA Survey (Bolatto et al., 2017). The NGLS, which will be further described in Section 1.3, observed the CO $J = 3 - 2$ line for 155 nearby galaxies. HERACLES compiled new CO $J = 2-1$ maps from the IRAM 30 metre telescope and data from the earlier BIMA-SONG survey for 48 THINGS galaxies. They performed a pixel-by-pixel analysis and found a strong correlation between molecular gas and star formation rate, with a nearly constant molecular gas depletion time ~ 2 Gyr (Bigiel et al., 2008; Leroy et al., 2008). The Extragalactic Database for Galaxy Evolution Survey using the Calar Alto Legacy Integral Field Area sample (EDGE-CALIFA) is a recent ongoing survey to combine CALIFA IFU optical spectroscopy with CARMA CO $J = 1-0$ data for a sample of 126 galaxies (Bolatto et al., 2017).

1.1.4 Dust Observations

The dust component of the ISM consists of carbon and silicate particles in a range of sizes from 50 Å to large grains up to 1 μm (Tielens, 2005). Dust grains are generally not a large fraction of the ISM by mass, as estimates of the total gas-to-dust mass ratio range from ~ 100 in the Milky Way to ~ 600 for some nearby galaxies (Young & Scoville, 1991). More recent results from a study of nearby galaxies with CO, H I, and dust mass maps show an average gas-to-dust ratio of ~ 72 using a pixel-by-pixel analysis (Sandstrom et al., 2013). Even though they are a minor component by mass, dust plays a key role in attenuating and re-radiating light in nearby galaxies. In addition, dust also plays an important part in interstellar chemistry and the creation of molecular hydrogen (Cazaux & Tielens, 2004).

Since dust grains radiate as blackbodies, with temperatures of between 15 to 75 Kelvins (Tielens, 2005), they are typically detected in the infrared and sub-millimetre region of the electromagnetic spectrum. Consequently, emission in nearby galaxies was measured first using the Infrared Astronomical Satellite (IRAS), launched in 1983. A compilation of all the bright nearby IRAS sources was made by Sanders et al. (2003). These infrared measurements have been greatly improved by the subsequent launches of the Spitzer Space Telescope and the Herschel Space Observatory. For example, the Herschel Reference Survey measured the dust content of 323 nearby galaxies using the Herschel 250, 350, and 500 μm bands (Boselli et al., 2010). Herschel-Astrophysical Terahertz Large Area Survey (H-ATLAS) data were used to measure the evolution of dust properties of galaxies up to $z \sim 0.5$ and found that the average dust mass at $z \sim 0.5$ is five times larger than in the local Universe, with the dust-to-stellar mass ratio increasing by a factor of three to four (Dunne et al., 2011). More recently, Genzel et al. (2015) stacked together Herschel observations to measure the cosmic dust scaling ratios for star-forming galaxies between $z = 0$ to $z = 3$.

Continuum measurements of the dust emission can also be performed using ground-based sub-millimetre telescopes, such as the SCUBA-2 bolometer on the JCMT, described further in Section 1.3. For nearby galaxies, millimetre and sub-millimetre telescopes would be measuring the long wavelength end of the dust blackbody spectral energy distribution (SED), which is often referred to as the Rayleigh-Jeans tail.

The Atacama Large milimetre Array (ALMA), with its great sensitivity and angular resolution, can efficiently observe this dust continuum emission from star-forming galaxies at $z = 0$ to $z \sim 6$ (Scoville et al., 2014, 2016).

Scoville et al. found that the CO emission and the rest wavelength 850 μm emission are linearly correlated. Therefore, if we can measure the 850 μm data from nearby galaxies, that would provide another tracer of the molecular gas component of the ISM. The average ratio between these two values found in Scoville et al. (2016) is:

$$\mathrm{M_{mol}[M_\odot]} = \frac{1}{(6.7 \pm 1.7) \times 10^{19}} \times \mathrm{L_{850\mu m}}\ [\mathrm{erg\ s^{-1}\ Hz^{-1}}] \tag{1.6}$$

However, there are many drawbacks to the use of this method, such as uncertainty in the dust temperature (Genzel et al., 2015), the metallicity/gas-to-dust ratio (Young & Scoville, 1991; Sandstrom et al., 2013), and potential contributions from the dust associated with the atomic gas. For example, the mean molecular gas to atomic gas ratio from the COLD GASS survey is 0.30, with a wide range in this measured ratio for individual galaxies (Saintonge et al., 2011a).

1.2 Environmental Effects on the ISM

1.2.1 Environmental Effects on the Atomic Gas Component

From the general introduction to galaxies and their properties presented previously, we find galaxies living in a range of different environments, including inside galaxy groups and clusters. Galaxy groups typically have less than 50 member galaxies and masses of $\sim 10^{13}$ M$_\odot$, with velocity dispersions for individual galaxies of ~ 150 km s^{-1} (Carroll & Ostlie, 2006). On the other hand, clusters can have thousands of member galaxies and masses of $\sim 10^{15}$ M$_\odot$, with velocity dispersions for individual galaxies of $\sim 800 - 1000$ km s^{-1} (Carroll & Ostlie, 2006). There is also a much higher mass-to-light ratio found in galaxy clusters, with most of the baryonic mass associated with a X-ray emitting, ionized intracluster medium (ICM) at a temperature of $10^7 - 10^8$ (Mo et al., 2010). Given the observed changes in the stellar population and morphology of galaxies in different environments discussed previously (e.g Blanton & Moustakas, 2009), we expect that the interstellar medium of these galaxies should also be modified by their environment.

Many past studies of the effects of environment on the interstellar medium have focused on the H I component of these galaxies. Early observations of 56 Virgo Cluster spiral galaxies found that they are deficient in their H I content compared to 110 spiral galaxies in lower density environments (Chamaraux et al., 1980). More recently, this type of analysis with large samples of galaxies has been greatly improved by the Arecibo Legacy Fast ALFA Survey (ALFALFA) (e.g Giovanelli et al., 2005; Martin et al., 2010), which is one of the largest H I surveys, observing $> 40\%$ of the sky. The Arecibo L-band Feed Array (ALFA) on the Arecibo radio telescope allowed for an enormous increase in the ability to perform large-scale surveys of galaxies.

Using the ALFALFA survey and stacking analysis, Fabello et al. (2012) found that the atomic gas fraction decreases as a function of local density and to a larger extent than their specific star formation rate (sSFR). This effect is most prominent in galaxies with stellar masses of less than $10^{10.5}$ M$_\odot$. For individual galaxies, Yoon & Rosenberg (2015) found that although the detection rate for SDSS galaxies in the ALFALFA sample decreases towards the group centre, the H I gas- to stellar-mass ratio does not significantly decline. They attribute this result to the shallow nature of the ALFALFA survey, which would only detect the remaining gas-rich objects inside denser environments. Using a stacking technique for the ALFALFA H I spectra, Brown et al. (2017) found evidence for the depletion of the atomic gas content in satellite galaxies, even in the group environment. This provides evidence for the idea of group pre-processing, where galaxies can be quenched even in the group environment, before falling into a cluster. The ALFALFA analysis is supported by the deeper GALEX Arecibo SDSS Survey (GASS), which measured H I spectra from over 800 galaxies and found that galaxies located in haloes with masses of between $10^{13} - 10^{14}$ $M_\odot$ are significantly deficient compared to galaxies in lower density environments (Catinella et al., 2013).

Detailed analysis of the H I distributions in nearby galaxies have also shown important changes with environment. For example, observations of the M81 group using the Very Large Array (VLA) show the gravitational interaction between M81, M82, and NGC3077, far beyond their optical disks, with long tidal tails and atomic gas bridges (Yun et al., 1994). Figure 1.3 shows the H I map compared to the stellar light distribution for the M81 group.

Initial surveys of H I in the extreme cluster environment have focused on the Virgo Cluster. The Virgo Cluster is a dynamically young cluster, with a large number of infalling gas-rich spiral galaxies. Furthermore, it is the closest cluster to the Milky Way, located at a distance of 16.7 Mpc (Mei et al., 2007). Furthermore, Virgo Cluster spirals have H I distributions that are truncated and often even smaller than their optical disks (Cayatte et al., 1990, 1994).

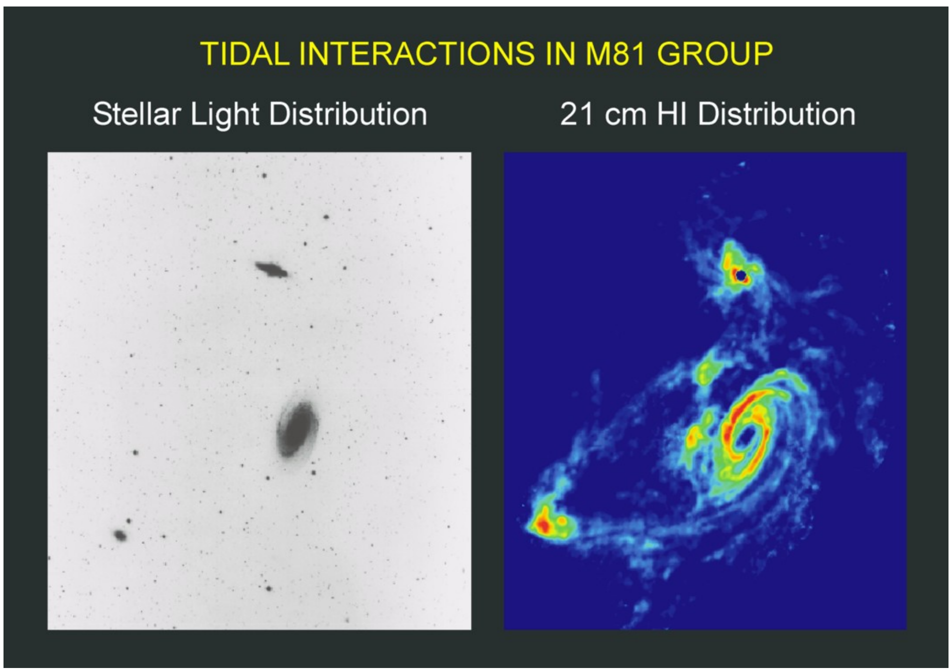

Figure 1.3 H I vs stellar light distribution of the M81 Group. The figure on the left is the visible image from the Digital Sky Survey and the figure on the right is the corresponding H I image from the VLA. The large extent of the atomic gas distribution and its interactions within the group environment are clear. Image courtesy of NRAO/AUI. Original file can be found at: *http://images.nrao.edu/Galaxy/Peculiar/116*.

Many of these spiral galaxies show clear signs of asymmetry and other extended structures in their H I gas.

The VLA Imaging of Virgo in Atomic Gas (VIVA) is a more recent survey of atomic gas in the cluster environment (Chung et al., 2009). The survey includes a combination of archival and new data of 53 Virgo spirals at a range of distances from the cluster centre and H I deficiencies. Figure 1.4 shows a compilation of the galaxies from the VIVA Survey, with the H I data overlaid on top of a ROSAT X-ray image. The VIVA survey found that galaxies near the centre of Virgo have smaller H I disks, whereas galaxies at intermediate distances have long H I tails, providing evidence that they are recent infalling galaxies (Chung et al., 2009).

Theorists have provided many explanations for these properties and how they could lead to the subsequent quenching of star formation. There are three main categories: the starvation of the supply of new gas, the process of galaxy interactions and mergers, and the effects of ram pressure stripping when traveling through the intercluster medium.

First, in order to continue star formation, blue spiral galaxies have to refuel their supply of cold molecular gas. The time it takes to deplete their molecular gas is roughly 2 Gyr for nearby spiral galaxies (Bigiel et al., 2008), a value much less than the age of the Universe. Even accounting for an average molecular to atomic gas ratio of 0.3 (Saintonge et al., 2011a), they would still require additional cold gas infall from the halo to remain star-forming over the age of the Universe. The loss of the atomic gas envelope, either through tidal effects upon entering the cluster environment or the inability to accrete new gas, is

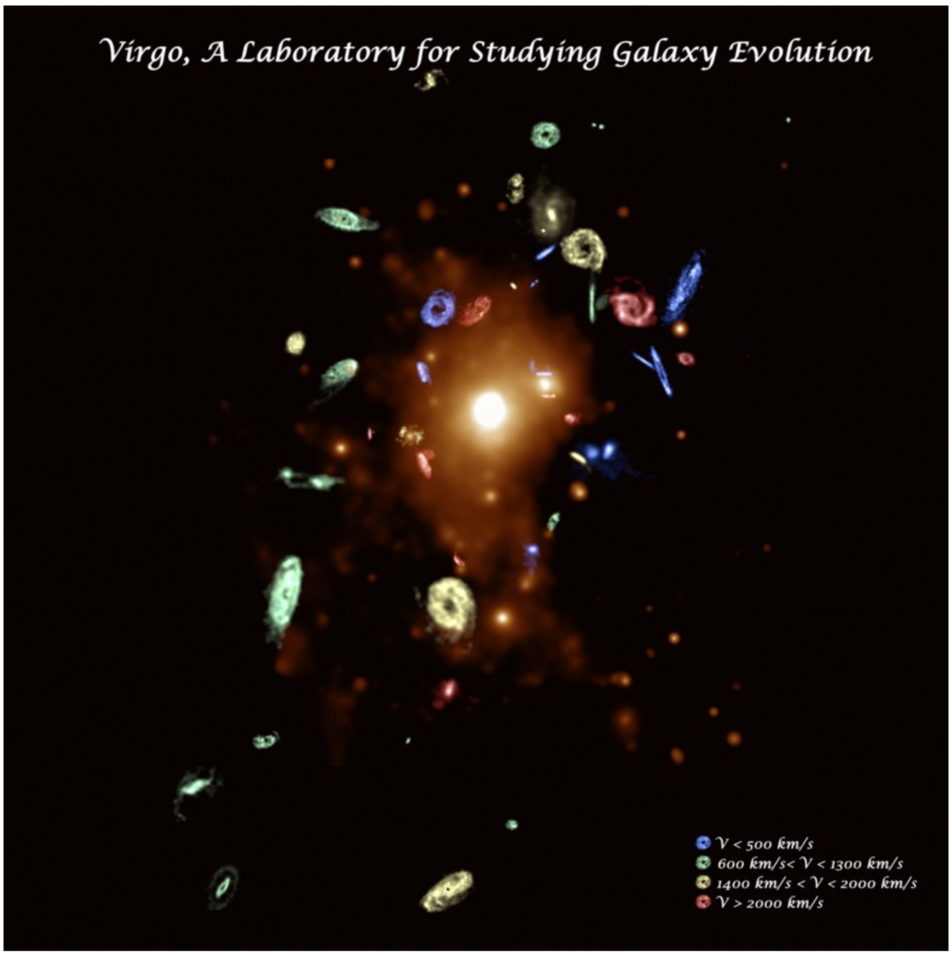

Figure 1.4 Compilation of the H I data from the VIVA Survey, overlaid on top of a ROSAT X-ray data. Image courtesy of NRAO/AUI and Chung et al. (2009), Columbia University. Original file can be found at: *http://images.nrao.edu/528.*

combined with the consumption of their gas reservoirs via the normal process of star formation and provides an explanation for the creation of lenticular (S0) galaxies inside galaxy clusters (Larson et al., 1980). Simulations show that this process, also known as 'strangulation', can be effective even in low-mass groups (Kawata & Mulchaey, 2008).

Second, the cold gas distribution can be disturbed by tidal interactions between member galaxies when they are close enough, which is seen clearly in the H I map for the M81 group (Yun et al., 1994) in Figure 1.3. This series of interactions could lead to morphological transformations, with long tidal tails and debris arcs, in a process called 'harassment' (Moore et al., 1996). In the late stages, interacting galaxies may merge together to form a new galaxy. Mergers can lead to a burst of star formation (a starburst) by transferring gas to the central region and to a post-starburst phase (Bekki, 1999). When the gas clouds inside these mergers collide, they will tend to lose their kinetic energy, leading to a reduction in their angular momentum and orbits which are closer to the centre. The disruption of the fragile gas disks in this process and the transition to a bulge-dominated system will likely quench future star formation in these systems.

Third, an infalling galaxy will feel the 'wind' from its movement through the hot intercluster medium (ICM). This effect may cause removal of gas from the disk of these galaxies, in a process called ram-pressure stripping (Gunn & Gott, 1972). The effectiveness of ram-pressure stripping is proportional to $\rho_{\rm ICM}\, v^2$, which means that it is most effective at high velocities and/or high ICM densities, such as conditions found inside galaxy clusters (Mo et al., 2010). This process is often provided as the cause of the disturbed appearance of several Virgo Cluster spirals (Cayatte et al., 1990, 1994). By stripping away the atomic gas reservoir, ram pressure stripping will remove the fuel for future star formation and lead to its rapid cessation. Figure 1.5 shows the effect of ram pressure stripping on the dust disks of two galaxies in the Virgo Cluster, with the characteristic warping and bowl-shaped appearance as they move through the intercluster medium.

In summary, there is strong observational and theoretical evidence that the group and cluster environment can change the total amount of H I gas and its distribution inside the host galaxy.

1.2.2 Environmental Effects on the Molecular Gas and Dust Components

Despite the vast amount of work done on the environmental effects on the atomic gas distribution, the extent to which the environment can affect the molecular gas is less well-known, partly due to diffculties in compiling large samples of molecular gas measurements. As discussed previously (Scoville et al., 2016), dust emission from nearby galaxies appears to be well-correlated with the molecular gas. Furthermore, SCUBA 850 μm studies of a sample of nearby galaxies show that the scale-length of the dust emission is less than half that of the H I emission (Thomas et al., 2004), suggesting a concentration of dust in the inner regions of spiral galaxies and high gas-to-dust ratio in the outskirts. Therefore, we will discuss the molecular gas and dust components together in this section.

Figure 1.5 HST Images of NGC4522 (top) and NGC4402 (bottom) in the Virgo Cluster, showing the effects of ram pressure stripping. The dust inside galaxies is spatially correlated with the gas, and the warping of the dust disk in these HST images provide visible evidence of the effects of moving through the intercluster medium at high speeds. Image courtesy of NASA & ESA. Original file can be found at: *https://www.spacetelescope.org/images/heic0911a/*.

The study of the effects of molecular gas with environment began with seminal CO observations of galaxies in the Virgo Cluster by Kenney & Young (1989). The data revealed that the molecular gas reservoirs in Virgo spirals are not as depleted as expected, given their H I deficiencies. Large amounts of molecular gas are able to survive inside these galaxies and any reduction in the total gas profiles is mostly driven by the depletion of H I gas in the outskirts (Kenney & Young, 1989). Unfortunately, this work lacked a similar sample of non-cluster spirals, which would allow them to compare Virgo galaxies to field and group galaxies with the same level of H I-deficiency.

More recent work suggests a stronger correlation between atomic gas depletion and removal of the molecular gas and dust components. Using the Herschel Space Observatory, astronomers can analyze the dust properties of nearby galaxies in great detail. Two Herschel studies, the Herschel Virgo Cluster Survey (HeViCS) and the Herschel Reference Survey (HRS), have studied the effects of environment on the dust component.

The Herschel Virgo Cluster Survey (HeViCS) looked at a sample of 15 galaxies with H I maps from the VIVA survey. For those galaxies, Cortese et al. (2010) found a strong link between the truncation of their dust disks and H I-deficiency in the Virgo Cluster. They also showed that ram-pressure stripping can explain both the observed truncation of the dust disks and the metal enrichment of the intracluster medium. The HRS is a similar Herschel survey of a larger sample of 323 galaxies (Boselli et al., 2010), which also includes galaxies in the Virgo Cluster. Cortese et al. (2012) found that HRS galaxies in a higher density environment have higher dust-to-H I ratios than field galaxies, suggesting that their H I disk is more easily removed than the dust disk. On the other hand, cluster galaxies possess lower dust-to-stellar mass ratios, which indicate that the cluster environment can also partially strip away the dust disk.

Follow-up studies of the molecular gas inside HeViCS and HRS galaxies have found similar results. Analysis of archival and new CO $J = 1 - 0$ for 35 HeViCS galaxies shows a strong correlation between molecular gas and the cold dust component (Corbelli et al., 2012). In addition, although the molecular gas mass per stellar mass is reduced for Virgo galaxies, the reduction is smaller than for the dust or atomic gas component (Corbelli et al., 2012). This result implies that the cluster environment affects the molecular gas less strongly than the atomic gas or dust component. Boselli et al. (2014c) used a variety of CO data collected from the literature to study the molecular gas for HRS galaxies. They found a inverse relationship between the size of the molecular disc and H I deficiency. They also found a depletion in the H_2 of Virgo galaxies compared to field galaxies with the same level of H I deficiency and suggest ram pressure stripping as the primary process for the removal of molecular gas (Boselli et al., 2014c).

Outside of the Virgo Cluster, molecular gas surveys of other environments include the Analysis of the Interstellar Medium of Isolated Galaxies (AMIGA) sample (Lisenfeld et al., 2011), galaxies in Hickson Compact Groups (HCG) (Martinez-Badenes et al., 2012), and galaxies in the Abell 1367 cluster (Scott et al., 2013). The AMIGA sample found strong correlations between the molecular gas content and far-infrared luminosity and between the molecular gas to atomic gas ratio and morphological type. In addition, they found enhancements in the ratio of molecular gas to B- and K-band luminosities for interacting galaxies of $0.2 - 0.3$ dex, compared to their isolated sample (Lisenfeld et al., 2011). Analysis of 88 galaxies in 20 HCGs found an excess in the molecular gas mass compared to isolated galaxies and an increase in the molecular gas to atomic gas ratio (Martinez-Badenes et al., 2012). Finally, Scott et al. (2013) looked at the CO $J = 1 - 0$ line for 19 late-type galaxies in the Abell 1367 cluster and found a range of different H I and H_2 deficiencies, including some H_2 rich galaxies.

A K-band (mass-selected) sample in the cluster environment, such as the HeViCS and the HRS, will necessarily include a large number of heavily H I-depleted galaxies. It is clear from studies of these two samples that prolonged exposure to the cluster environment will inevitably remove the dust and to a lesser extent, the H_2 gas. On the other hand, interactions and the overdense environments may also raise the molecular gas content in gas-rich galaxies.

Therefore, given the results of these previous surveys and the strong link between H_2 and H I deficiencies, a complementary strategy is to look at the gas-rich galaxies inside clusters, collect data from a sample of similar gas-rich galaxies in the lower density environments, and compare their ISM and star formation properties. For this thesis, I use data from two large surveys of nearby gas-rich galaxies.

1.3 NGLS and JINGLE

The JCMT Nearby Galaxies Legacy Survey (NGLS) and the JCMT dust and gas in Nearby Galaxies Legacy Exploration (JINGLE) are both large projects undertaken at the James Clerk Maxwell Telescope (JCMT) to study the ISM of nearby galaxies. The JCMT is a 15 metre sub-mm telescope located on the summit of Mauna Kea. There are three main instruments currently mounted on the JMCT[1]: Receiver A3 (RxA3m) – a 230 GHz, single-pixel heterodyne receiver; Heterodyne Array Receiver Program (HARP) – a 350 GHz, 16 pixel heterodyne receiver (Buckle et al., 2009); and the Submilimetre Common-User Bolometer Array (SCUBA-2) – a 450/850 micron 10,000 pixel bolometer (Holland et al., 2013). For the galaxies used in this analysis, RxA3m data will be used to measure the CO $J = 2-1$ line, HARP will be used to measure the CO $J = 3-2$ line, and SCUBA-2 will be used to measure the continuum emission from dust particles in the ISM.

The JCMT Nearby Galaxies Legacy Survey (NGLS) is a HARP and SCUBA-2 survey of a H I-flux (> 6.3 Jy km/s) selected sample of 155 nearby galaxies (within a distance of ~ 25 Mpc) (Wilson et al., 2009, 2012). This thesis will use the CO $J = 3-2$ data to trace the molecular gas distributions for spiral galaxies from the NGLS and the associated Hα images to measure their resolved star formation rates (Sánchez-Gallego et al., 2012). This sample is well-suited to study environmental effects, as it encompasses a wide variety of environments, including galaxies within the Virgo Cluster. Further extensions to the original sample of 155 galaxies include JCMT proposals to observe all

[1] http://www.eaobservatory.org/jcmt/instrumentation

the galaxies in the Virgo Cluster that satisfy the original survey criteria and the addition of galaxies from the Herschel Reference Survey (HRS) that also satisfy the NGLS criteria.

The JCMT dust and gas in Nearby Galaxies Legacy Exploration (JINGLE) is an ongoing large survey at the JCMT to study the evolution of a mass-selected sample of 193 Herschel-detected nearby galaxies with SCUBA-2 850 micron observations[2]. These galaxies have $M_* > 10^9\ M_\odot$, redshifts in the range of $0.01 < z < 0.05$, and detections at the 3σ level in the Herschel 250 and 350 μm bands (Saintonge et al., in prep). As a result, they are likely to be gas-rich, similar to the NGLS sample. A subset of 95 galaxies will also have RxA3m observations to measure the CO $J = 2-1$ line. The JINGLE sample also contains galaxies from a wide variety of environments, including galaxies from the Coma Cluster, a rich cluster located at a distance of $\sim$ 100 Mpc. In this thesis, I use the SCUBA-2 850 μm fluxes for 105 galaxies and the CO $J = 2-1$ data for a subset of 34 galaxies in the initial Data Release 1 (DR1) from the JINGLE survey.

1.4 Thesis Project

In this thesis, I explore the effects of the environment on the ISM (including both the atomic and molecular gas component) and star formation properties of spiral galaxies. I use a multi-wavelength dataset from JINGLE and the NGLS, two large samples of gas-rich galaxies in the nearby Universe that include isolated galaxies, group galaxies, and cluster galaxies. I determine

[2] http://www.eaobservatory.org/jcmt/science/large-programs/jingle/

whether the environment plays a role in modifying the spatial distributions of the ISM inside spiral galaxies, regulate the process in the conversion between atomic and molecular gas, and govern the efficiency in converting its gas into stars.

In Chapter 2, I look at the sample of 98 spiral galaxies from the NGLS, dividing them between the field, group, and Virgo Cluster environment (Mok et al., 2016). Since the CO $J = 3-2$ line for many galaxies was not detected at required signal-to-noise ratio, survival analysis is used to include the effects of upper limits. The molecular gas mass, the star formation rate, the total gas mass (H_2 + H I), the molecular gas depletion time (SFR/H_2), and other properties are compared between the three samples and the effects of environment measured.

In Chapter 3, I use the resolved CO $J = 3-2$, Hα, and H I data to measure the surface density radial profiles for the sample of spiral galaxies in the NGLS (Mok et al., 2017). The H I data come from a compilation of H I observations in the Virgo Cluster called VIVA (Chung et al., 2009) and follow-up proposals at the VLA to observe NGLS galaxies. The same galaxy properties are measured as in Chapter 1, but now I measure and compare their radial distributions between three samples.

In Chapter 4, I use the initial release data-set (DR1) from the JINGLE survey to explore environmental effects. This sample of galaxies is important because we can measure the properties of galaxies in Coma Cluster and haloes of different sizes, as well as galaxies in different stages of infall into the overdense regions. I compare the SCUBA-2 850 μm and RxA3m CO $J = 2-1$

measurements of the molecular gas masses and measure important galaxy scaling relations.

In Chapter 5, I provide a summary of the key results from the 3 previous chapters and describe some future work in this research area.

Bibliography

Bekki K., 1999, ApJ, 510, L15

Bekki K., 2014, MNRAS, 438, 444

Bell E. F., McIntosh D. H., Katz N., Weinberg M. D., 2003, ApJS, 149, 289

Bell E. F., et al., 2012, ApJ, 753, 167

Bigiel F., Leroy A., Walter F., Brinks E., de Blok W. J. G., Madore B., Thornley M. D., 2008, AJ, 136, 2846

Blanton M. R., Moustakas J., 2009, ARA&A, 47, 159

Bolatto A. D., Wolfire M., Leroy A. K., 2013, ARA&A, 51, 207

Bolatto A. D., et al., 2017, preprint, (arXiv:1704.02504)

Boselli A., et al., 2010, PASP, 122, 261

Boselli A., Cortese L., Boquien M., 2014a, A&A, 564, A65

Boselli A., Cortese L., Boquien M., Boissier S., Catinella B., Lagos C., Saintonge A., 2014b, A&A, 564, A66

Boselli A., Cortese L., Boquien M., Boissier S., Catinella B., Gavazzi G., Lagos C., Saintonge A., 2014c, A&A, 564, A67

Brinchmann J., Charlot S., White S. D. M., Tremonti C., Kauffmann G., Heckman T., Brinkmann J., 2004, MNRAS, 351, 1151

Brown T., et al., 2017, MNRAS, 466, 1275

Buckle J. V., et al., 2009, MNRAS, 399, 1026

Butcher H., Oemler Jr. A., 1984, ApJ, 285, 426

Calzetti D., et al., 2007, ApJ, 666, 870

Calzetti D., et al., 2010, ApJ, 714, 1256

Carroll B. W., Ostlie D. A., 2006, An introduction to modern astrophysics and cosmology. Pearson

Catinella B., et al., 2010, MNRAS, 403, 683

Catinella B., et al., 2013, MNRAS, 436, 34

Cayatte V., van Gorkom J. H., Balkowski C., Kotanyi C., 1990, AJ, 100, 604

Cayatte V., Kotanyi C., Balkowski C., van Gorkom J. H., 1994, AJ, 107, 1003

Cazaux S., Tielens A. G. G. M., 2004, ApJ, 604, 222

Chamaraux P., Balkowski C., Gerard E., 1980, A&A, 83, 38

Chung A., van Gorkom J. H., Kenney J. D. P., Crowl H., Vollmer B., 2009, AJ, 138, 1741

Colless M., et al., 2001, MNRAS, 328, 1039

Corbelli E., et al., 2012, A&A, 542, A32

Cortese L., et al., 2010, A&A, 518, L49

Cortese L., et al., 2012, A&A, 540, A52

Cross N., et al., 2001, MNRAS, 324, 825

Cucciati O., et al., 2012, A&A, 539, A31

Dame T. M., Hartmann D., Thaddeus P., 2001, ApJ, 547, 792

Dickey J. M., Lockman F. J., 1990, ARA&A, 28, 215

Downes D., Solomon P. M., 1998, ApJ, 507, 615

Draine B. T., 2011, Physics of the Interstellar and Intergalactic Medium. Princeton University Press

Dressler A., 1980, ApJ, 236, 351

Dunne L., et al., 2011, MNRAS, 417, 1510

Elbaz D., et al., 2011, A&A, 533, A119

Fabello S., Kauffmann G., Catinella B., Li C., Giovanelli R., Haynes M. P., 2012, MNRAS, 427, 2841

Fumagalli M., Gavazzi G., 2008, A&A, 490, 571

Galametz M., et al., 2013, MNRAS, 431, 1956

Gavazzi G., Fumagalli M., Galardo V., Grossetti F., Boselli A., Giovanelli R., Haynes M. P., Fabello S., 2012, A&A, 545, A16

Genzel R., et al., 2010, MNRAS, 407, 2091

Genzel R., et al., 2015, ApJ, 800, 20

Gil de Paz A., et al., 2007, ApJS, 173, 185

Giovanelli R., et al., 2005, AJ, 130, 2598

Gunn J. E., Gott III J. R., 1972, ApJ, 176, 1

Hao C.-N., Kennicutt R. C., Johnson B. D., Calzetti D., Dale D. A., Moustakas J., 2011, ApJ, 741, 124

Heyer M. H., Brunt C., Snell R. L., Howe J. E., Schloerb F. P., Carpenter J. M., 1998, ApJS, 115, 241

Holland W. S., et al., 2013, MNRAS, 430, 2513

Huang S., et al., 2014, ApJ, 793, 40

Hubble E. P., 1926, ApJ, 64, 321

Kawata D., Mulchaey J. S., 2008, ApJ, 672, L103

Kenney J. D. P., Young J. S., 1989, ApJ, 344, 171

Kennicutt Jr. R. C., 1998, ARA&A, 36, 189

Kennicutt R. C., Evans N. J., 2012, ARA&A, 50, 531

Kennicutt Jr. R. C., et al., 2003, PASP, 115, 928

Kennicutt Jr. R. C., et al., 2009, ApJ, 703, 1672

Komatsu E., et al., 2009, ApJS, 180, 330

Kroupa P., Weidner C., 2003, ApJ, 598, 1076

Larson R. B., 1981, MNRAS, 194, 809

Larson R. B., Tinsley B. M., Caldwell C. N., 1980, ApJ, 237, 692

Leroy A. K., Walter F., Brinks E., Bigiel F., de Blok W. J. G., Madore B., Thornley M. D., 2008, AJ, 136, 2782

Lisenfeld U., et al., 2011, A&A, 534, A102

Madau P., Dickinson M., 2014, ARA&A, 52, 415

Martin A. M., Papastergis E., Giovanelli R., Haynes M. P., Springob C. M., Stierwalt S., 2010, ApJ, 723, 1359

Martinez-Badenes V., Lisenfeld U., Espada D., Verdes-Montenegro L., García-Burillo S., Leon S., Sulentic J., Yun M. S., 2012, A&A, 540, A96

Mei S., et al., 2007, ApJ, 655, 144

Mo H., van den Bosch F. C., White S., 2010, Galaxy Formation and Evolution. Cambridge University Press

Mok A., et al., 2016, MNRAS, 456, 4384

Mok A., Wilson C. D., Knapen J. H., Sánchez-Gallego J. R., Brinks E., Rosolowsky E., 2017, MNRAS, 467, 4282

Moore B., Katz N., Lake G., Dressler A., Oemler A., 1996, Nature, 379, 613

Muller C. A., Oort J. H., 1951, Nature, 168, 357

Noeske K. G., et al., 2007, ApJ, 660, L43

Oesch P. A., et al., 2016, ApJ, 819, 129

Peng Y.-j., et al., 2010, ApJ, 721, 193

Planck Collaboration et al., 2016, A&A, 594, A13

Refregier A., 2003, ARA&A, 41, 645

Regan M. W., Thornley M. D., Helfer T. T., Sheth K., Wong T., Vogel S. N., Blitz L., Bock D. C.-J., 2001, ApJ, 561, 218

Rubin V. C., Ford Jr. W. K., Thonnard N., 1980, ApJ, 238, 471

Ryden B., 2003, Introduction to cosmology. Addison-Wesley

Saintonge A., et al., 2011a, MNRAS, 415, 32

Saintonge A., et al., 2011b, MNRAS, 415, 61

Sánchez-Gallego J. R., Knapen J. H., Wilson C. D., Barmby P., Azimlu M., Courteau S., 2012, MNRAS, 422, 3208

Sanders D. B., Mazzarella J. M., Kim D.-C., Surace J. A., Soifer B. T., 2003, AJ, 126, 1607

Sandstrom K. M., et al., 2013, ApJ, 777, 5

Santini P., et al., 2014, A&A, 562, A30

Schawinski K., et al., 2014, MNRAS, 440, 889

Scott T. C., Usero A., Brinks E., Boselli A., Cortese L., Bravo-Alfaro H., 2013, MNRAS, 429, 221

Scoville N. Z., Yun M. S., Sanders D. B., Clemens D. P., Waller W. H., 1987, ApJS, 63, 821

Scoville N., et al., 2014, ApJ, 783, 84

Scoville N., et al., 2016, ApJ, 820, 83

Solomon P. M., Vanden Bout P. A., 2005, ARA&A, 43, 677

Somerville R. S., Hopkins P. F., Cox T. J., Robertson B. E., Hernquist L., 2008, MNRAS, 391, 481

Thomas H. C., Alexander P., Clemens M. S., Green D. A., Dunne L., Eales S., 2004, MNRAS, 351, 362

Tielens A. G. G. M., 2005, The Physics and Chemistry of the Interstellar Medium. Cambridge University Press

Treu T., 2010, ARA&A, 48, 87

Walcher J., Groves B., Budavári T., Dale D., 2011, Ap&SS, 331, 1

Walter F., Brinks E., de Blok W. J. G., Bigiel F., Kennicutt Jr. R. C., Thornley M. D., Leroy A., 2008, AJ, 136, 2563

Whitaker K. E., van Dokkum P. G., Brammer G., Franx M., 2012, ApJ, 754, L29

Wilson C. D., et al., 2009, ApJ, 693, 1736

Wilson C. D., et al., 2012, MNRAS, 424, 3050

Wolfire M. G., Konigl A., 1991, ApJ, 383, 205

Yoon I., Rosenberg J. L., 2015, ApJ, 812, 4

York D. G., et al., 2000, AJ, 120, 1579

Young J. S., Scoville N. Z., 1991, ARA&A, 29, 581

Young J. S., et al., 1995, ApJS, 98, 219

Yun M. S., Ho P. T. P., Lo K. Y., 1994, Nature, 372, 530

Zwicky F., 1937, ApJ, 86, 217

Chapter 2

The JCMT Nearby Galaxies Legacy Survey – X. Environmental Effects on the Molecular Gas and Star Formation Properties of Spiral Galaxies

Angus Mok [1], C. D. Wilson[1], J. Golding[1], B. E. Warren[2], F. P. Israel[3], S. Serjeant[4], J. H. Knapen[5,6], J. R. Sánchez-Gallego[5,6,7], P. Barmby[8], G. J. Bendo[9], E. Rosolowsky[10], and P. van der Werf[11]

[1] Department of Physics & Astronomy, McMaster University, Hamilton, Ontario L8S 4M1, Canada

[2] International Centre for Radio Astronomy Research, M468, University of Western Australia, 35 Stirling Hwy, Crawley, WA 6009, Australia

[3] Sterrewacht Leiden, Leiden University, PO Box 9513, 2300 RA Leiden, The Netherlands

[4] Department of Physics & Astronomy, The Open University, Milton Keynes MK7 6AA, United Kingdom

[5] Instituto de Astrofísica de Canarias, E-38205 La Laguna, Tenerife, Spain

[6] Departamento de Astrofísica, Universidad de La Laguna, E-38200 La Laguna, Tenerife, Spain

[7] Department of Physics and Astronomy, University of Kentucky, 40506-0055, Lexington, Kentucky, United States

[8] Department of Physics & Astronomy, University of Western Ontario, London, Ontario N6A 3K7, Canada

[9] UK ALMA Regional Centre Node, Jodrell Bank Centre for Astrophysics, School of Physics and Astronomy, University of Manchester, Oxford Road, Manchester M13 9PL, United Kingdom

[10] Department of Physics, University of Alberta, Edmonton, Ontario T6G 2R3, Canada

[11] Kapteyn Astronomical Institute, Postbus 800, NL-9700 AV Groningen, The Netherlands

Abstract

We present a study of the molecular gas properties in a sample of 98 H I - flux selected spiral galaxies within ~ 25 Mpc, using the CO $J = 3-2$ line observed with the James Clerk Maxwell Telescope. We use the technique of survival analysis to incorporate galaxies with CO upper limits into our results.

Comparing the group and Virgo samples, we find a larger mean H_2 mass in the Virgo galaxies, despite their lower mean H I mass. This leads to a significantly higher H_2 to H I ratio for Virgo galaxies. Combining our data with complementary Hα star formation rate measurements, Virgo galaxies have longer molecular gas depletion times compared to group galaxies, due to their higher H_2 masses and lower star formation rates. We suggest that the longer depletion times may be a result of heating processes in the cluster environment or differences in the turbulent pressure. From the full sample, we find that the molecular gas depletion time has a positive correlation with the stellar mass, indicative of differences in the star formation process between low and high mass galaxies, and a negative correlation between the molecular gas depletion time and the specific star formation rate.

2.1 Introduction

Star formation in the Universe takes place inside galaxies, where they convert their available gas reservoirs into stars. In particular, stars are born inside cold, dense molecular clouds and so a complete analysis of the star formation process requires the study of a galaxy's molecular gas content. Previous work has shown that star formation is more closely linked to the molecular gas, as compared to either the atomic hydrogen (H I) mass or the total gas (H I + H_2) mass (Bigiel et al., 2008; Leroy et al., 2008). These studies of star formation and molecular gas data for nearby galaxies have also revealed short H_2 depletion times compared to the age of the galaxy (Leroy et al., 2008; Saintonge et al., 2011; Bigiel et al., 2011), which suggests an ongoing need to replenish their molecular gas reservoir.

Spiral galaxies are the primary targets for this type of analysis, as star formation does not take place equally in all galaxies. For example, the morphological classification between early- and late-type galaxies tends to correspond to their stellar population, such as the well-known 'red sequence' and 'blue cloud' found in colour-magnitude diagrams (e.g. Strateva et al., 2001; Bell et al., 2003). The key difference between these two galaxy populations is their typical star formation state: whether they are undergoing active star formation or if they are mostly quiescent objects. Even for spiral galaxies along the Hubble sequence, the star formation rate has been shown to differ greatly (Kennicutt, 1998a).

The local environment of these galaxies can also influence galaxy evolution, from isolated galaxies, to groups of tens of galaxies, to clusters of thousands of galaxies. Denser environments in the Universe are dominated by early-type, red sequence galaxies (Baldry et al., 2006; Blanton & Moustakas, 2009). For spiral galaxies inside clusters, observations have shown a deficiency of atomic hydrogen (Chamaraux et al., 1980; Haynes & Giovanelli, 1986; Solanes et al., 2001; Gavazzi et al., 2005) and a reduction in the scale length of Hα emission (Koopmann et al., 2006), which is linked to young stars and star formation. On a smaller scale, some studies of galaxies with nearby companions have shown that star formation is generally unaffected, other than for the rare cases where mergers and interactions leads to a statistically significant but moderate enhancement in the star formation rate (Knapen & James, 2009;

Knapen et al., 2015). On the other hand, a larger sample of interacting pairs from the SDSS shows signs of a star formation enhancement at the smallest separations (Ellison et al., 2013).

Many possible physical processes have been invoked to explain the effects of environment. For example, galaxies may be affected by harassment from other cluster members (Moore et al., 1996) or be starved from their gas supply (Larson et al., 1980). In more extreme environments, ram-pressure stripping of a galaxy's gas content can take place (Gunn & Gott, 1972), and interactions and mergers can directly increase the gas content of galaxies or change the distribution of their gas. However, it remains unclear whether these processes can directly affect the molecular gas content, with its high surface density and its location deep inside the galaxy's potential well.

A good place to study the effects of environment on galaxy evolution is the Virgo Cluster, due to its close proximity and the large numbers of infalling spiral galaxies. One of the initial studies of molecular gas in Virgo spirals using the CO tracer was performed with the 7 metre Bell Laboratories antenna (Stark et al., 1986), finding correlations between the radio continuum and far-infrared data. Further studies helped determine the conversion ratio between the CO $J = 1-0$ luminosity and the molecular gas mass (Knapp et al., 1987). Subsequent CO observations with the Five College Radio Astronomy Observatory (FCRAO) have shown that the molecular content of Virgo spirals may be quite similar to that of field galaxies (Kenney & Young, 1989), but other groups have found hints of a reduction in the size of the molecular gas disk in Virgo spirals (Fumagalli & Gavazzi, 2008). Recent results from the HeViCS survey indicate a reduction in the amount of molecular gas per unit stellar mass in H I deficient galaxies (Corbelli et al., 2012). Finally, Vollmer et al. (2012) have looked at resolved measurements of 12 Virgo spiral galaxies and found a relationship between molecular gas mass and star formation, but no evidence for environmental differences in the star formation efficiency. A complete picture of the effects of environment on star formation and the molecular gas content of galaxies remains elusive.

This paper uses a large sample of 98 H I - flux selected spiral galaxies, with a majority coming from the original Nearby Galaxies Legacy Survey (Wilson et al., 2012). One of the main objectives of the NGLS is to study the effect of environment on a galaxy's molecular gas content by using CO $J = 3-2$ observations with the James Clerk Maxwell Telescope (JCMT) (Wilson et al., 2009, 2012). The CO $J = 3-2$ line is a tracer for warmer and denser gas than the CO $J = 1-0$ line and appears to be well correlated with the far-infrared luminosity, a proxy for the star formation rate (Iono et al., 2009; Wilson et al., 2012). We supplement the NGLS data with follow up JCMT surveys in the Virgo cluster and some galaxies from the Herschel Reference Survey (HRS) sample. Our analysis also includes data from other sources, including stellar masses and star formation rates.

In § 2, we present our observations and the general properties of our sample. In § 3, we discuss the use of survival analysis for datasets containing censored data (such as the H_2 gas mass) and present our analysis of galaxy properties. We also include a detailed comparison of the group and Virgo populations, as well as the CO detected and non-detected samples. In § 4, we present some specific tests of our results and the correlations found between various properties of the galaxies in our sample.

2.2 Sample Selection, Observations, and Data Processing

2.2.1 Sample Selection

The objective of our analysis is to create a large sample of nearby, gas-rich spiral galaxies. First, we select only spiral galaxies with H I flux > 6.3 Jy km s^{-1}, which corresponds to a log H I mass of 8.61 (in solar units) at the sample's median distance of 16.7 Mpc. The H I flux is identified using the HyperLeda database (Paturel et al., 2003; Makarov et al., 2014), which complies different survey results and produces a weighted average of the results. The database can be found online[1]. We also use the HyperLeda database to select only spiral galaxies using the morphological type code, removing from the sample galaxies that are ellipticals or lenticulars. We identify Virgo galaxies in our sample using the catalog from Binggeli et al. (1985).

Next, we impose a size limit on our galaxies. The non-Virgo sample is limited to galaxies with $D_{25} < 5'$, which at our distance limit of ~ 25 Mpc corresponds to $D_{25} < 36$ kpc. We therefore include only the 39 Virgo spiral galaxies with $D_{25} < 7.4'$ in order to match the physical size limits of of the Virgo and non-Virgo samples. Note that for all galaxies in the Virgo sample, we have assumed a standard distance of 16.7 Mpc (Mei et al., 2007).

[1] http://leda.univ-lyon1.fr/

To subdivide our sample further, we use the Garcia (1993) catalog. They used the LEDA data base to identify a robust set of 485 groups out of a sample of 6392 local galaxies by their 3D projection in space. Comparing our galaxy sample to the groups from their catalog yields a total of 40 galaxies. In addition, we place two galaxies, NGC0450 and NGC2146A, which are known from the Karachentsev (1972) catalog to be in close pairs, into this category as well. This results in a total of 42 spiral galaxies meeting our H I flux and size criterion that are members of groups. The 17 remaining galaxies constitute our field (or non-group) galaxy sample.

A summary of the sample sources, subdivided into the field, group, and Virgo populations, are presented in Table 2.1. There are three main sources of the CO $J = 3-2$ data. The first is the Nearby Galaxies Legacy Survey (Wilson et al., 2012). The second is a follow on study to complete observations in the Virgo cluster (project code M09AC05), using the same criterion as the parent NGLS survey. As a result, we do not expect significant differences between these two sources. Finally, to increase the number of galaxies in our sample, we also include a subset of Herschel Reference Survey (HRS) galaxies that fulfill the criteria listed above and are not already a member of the NGLS (Boselli et al., 2010). One potential different between the three sources of data is that the Herschel Reference Survey also has a K-band (or stellar mass) selection, but we do not expect it to greatly influence the results in this paper. Also, a subset of group galaxies is identified by the HRS as being in the Virgo outskirts, which we have kept in the group category given their local environment is likely more similar to the group than Virgo category. A full discussion of the three sources of our CO $J = 3 - 2$ can be found in Appendix 2.7.

Table 2.1 Sample Sources

Category	Total	Field	Group	Virgo
NGLS	53	12	21	20
Virgo Follow-Up (M09AC05)	17	0	0	17
HRS (M14AC03)	28	5	21	2
Total	98	17	42	39

Finally, due to our sample criteria, we are biased towards gas-rich, nearby, moderately-sized galaxies and to the detriment of H I deficient, far-away, larger, non-spiral galaxies. This is done to ensure a consistent statistical sample and to obtain satisfactory detection rates, as discussed in the observation section below.

2.2.2 Observations

The observations and data processing for the 155 galaxies in the NGLS are described in detail in Wilson et al. (2012), and so only a basic summary is given here. We observed the CO $J = 3-2$ line with the JCMT's HARP instrument (Buckle et al., 2009), which has $\eta_{MB} = 0.6$ and an angular resolution of $14.5''$. All galaxies were mapped out to at least $D_{25}/2$ with a 1 sigma sensitivity of better than 19 mK (T_A^*; 32 mK T_{MB}) at a spectral resolution of 20 km s^{-1}. The CO luminosities are measured on the T_{MB} scale. The internal calibration uncertainty is 10%. The reduced images, noise maps, and spectral cubes are available via the survey website[2] and also via the Canadian Astronomical Data Centre[3].

[2] http://www.physics.mcmaster.ca/~wilson/www_xfer/NGLS/

[3] DOI 10.1111/j.1365-2966.2012.21453.x

For galaxies with CO detections, we used the zeroth moment maps made with a noise cutoff of 2σ to measure the CO $J = 3 - 2$ luminosity (see Wilson et al. (2012) for further details). We use an aperture chosen by eye to capture all of the real emission from the galaxy. For galaxies without detections, 2σ upper limits were calculated from the noise maps assuming a line width of 100 km s^{-1} and using an aperture with a diameter of $1'$. The full sample includes 57 spiral galaxies from the NGLS, 14 spiral galaxies observed with the JCMT in 2009 February-May (JCMT program M09AC05), and 27 spiral galaxies from the Herschel Reference Survey (JCMT program M14AC03). The galaxies were processed using the same methods adopted for the NGLS and the calibration uncertainty for these data is also 10%.

We convert the CO $J = 3 - 2$ luminosities to molecular hydrogen mass adopting a CO-to-H$_2$ conversion factor of $X_{CO} = 2 \times 10^{20}$ cm^{-2} (K km s^{-1})$^{-1}$ (Strong et al., 1988) and a CO $J = 3 - 2/J = 1 - 0$ line ratio of 0.18 (Wilson et al., 2012). This measurement is similar to the CO $J = 3 - 2/J = 1 - 0$ line ratio of Virgo spiral galaxies obtained by other groups (Hafok & Stutzki, 2003). With these assumptions, the molecular hydrogen mass is given by:

$$M_{H_2} = 17.8(R_{31}/0.18)^{-1} L_{CO(3-2)} \tag{2.1}$$

where R_{31} is the CO $J = 3 - 2/J = 1 - 0$ line ratio, M_{H_2} is in $M_\odot$, and $L_{CO(3-2)}$ is in units of K km s^{-1} pc^2.

We note that the assumption of a constant conversion factor may not be correct in all cases. For example, the conversion factor can be affected by the ambient radiation field and the metallicity (Israel, 1997). Adopting a single value for X_{CO} will produce an underestimate of the molecular gas mass in galaxies where the metallicity is more than about a factor of two below solar (Wilson, 1995; Arimoto et al., 1996; Bolatto et al., 2008; Leroy et al., 2012). In a recent review paper on the conversion factor, Bolatto et al. (2013) suggested a possible prescription that is based on the gas surface density and metallicity. However, given the large scatter in their observational results and the fact that our galaxies are all relatively 'normal' spiral galaxies, we have decided to maintain the constant conversion factor used in the previous papers in this series.

We also use data sourced from other surveys. As stated in the section on our sample selections, the H I fluxes and morphological types for all the galaxies are taken from the most recent values of the HyperLeda database. We also use the database for measurements of redshift distances and D_{25} sizes. Stellar masses for individual galaxies are taken from the S^4G survey (Sheth et al., 2010) using the NASA/IPAC Infrared Science Archive, for all the galaxies where they are available. The S^4G survey have calibrated their stellar masses using the two IRAC bands, 3.6 and 4.5 μm, using the prescription from Eskew et al. (2012) and assuming a Salpeter IMF. To convert to a Kroupa IMF, we multiply by a factor of 0.7, which has been used in previous work (e.g. Elbaz et al., 2007). We have also used the distance measurements in the S^4G catalog to adjust the stellar masses to correspond to the distances used in this analysis.

For the 8 galaxies where the stellar mass is unavailable, we substitute K-band luminosities from the 2MASS database using the extended source catalogue (Skrutskie et al., 2006). We have assumed a total mass-to-light ratio of 0.533 in solar units for Sbc/Sc-type spiral galaxies from Table 7 in Portinari et al. (2004) with the Kroupa IMF, as they comprise a majority of the galaxies without masses from the S^4G survey. For comparison, the corresponding value for Sa/Sab-type spiral galaxies is 0.698. The average stellar mass for these galaxies is lower than that of the sample as a whole, but since they only comprise a small percentage of the total sample, we do not expect this difference to have a significant effect on our results.

In addition, Hα-derived star formation rates are taken from Sánchez-Gallego et al. (2012), with typical uncertainties of 18 per cent. We note that the formulas from Kennicutt et al. (2009) assume a stellar initial mass function (IMF) from Kroupa & Weidner (2003). For the additional spiral galaxies from the Virgo cluster observed in the M09AC05 program, we use Hα fluxes from the GOLDmine database (Gavazzi et al., 2003). For the galaxies from the HRS sample, we use the data from a new Hα study of these galaxies (Boselli et al., 2015). The Hα data from all three sources are corrected for extinction and converted into star formation rates using the same procedure as Sánchez-Gallego et al. (2012). We also investigate the effects of including a mid-IR star formation tracer using data from the S^4G survey and find there is moderate scatter between the two measurements. However, we have chosen to present the extinction-corrected Hα data in order to maintain continuity with the previous papers in this series.

Detailed properties for the individual galaxies are presented for the field galaxies in Table 2.7, the group galaxies in Table 2.8, and the Virgo sample in Table 2.9, located in Appendix 2.8. Maps of the CO detected galaxies can be found in Appendix 2.9. The field sample is shown in Figure 2.9, the group

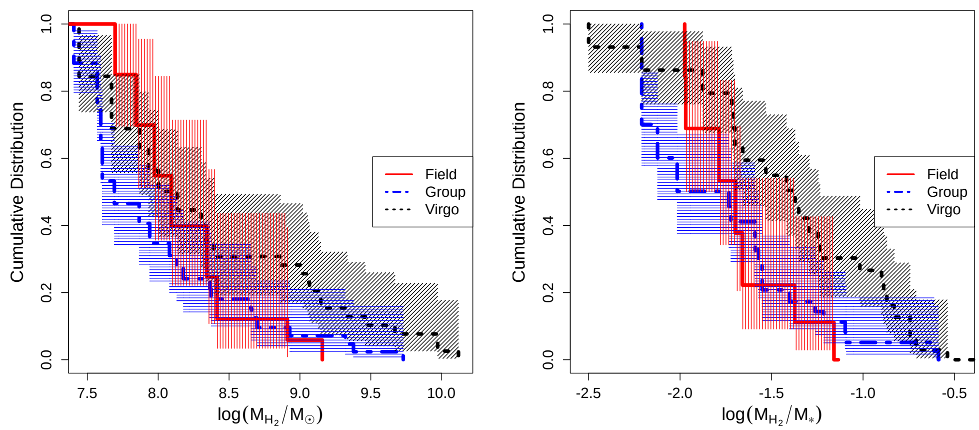

Figure 2.1 **Left:** Survival functions for the molecular hydrogen gas mass in the field (red solid line), group (blue dot-dash line), and Virgo (black dashed line) sample galaxies using the Kaplan-Meier estimator. The 'steps' in the distribution correspond to detections. The 95% confidence intervals are overlaid for the three distributions. **Right:** Survival functions for the molecular hydrogen gas mass divided by the stellar mass in the field, group and Virgo sample galaxies.

sample in Figures 2.10 and 2.11, and the Virgo sample in Figure 2.12. Virgo galaxies observed with two overlapping fields are presented in Figure 2.13, while NGC 4303, observed using the raster method, is presented in Figure 2.14. Note that images of NGC4254 and NGC4579 can be found in Wilson et al. (2012) and are not repeated here.

2.2.3 Survival Analysis and the Kaplan-Meier Estimator

In statistics, survival analysis is often used with censored datasets, i.e. datasets that include upper or lower limits. The original purpose of survival analysis is in medicine, where data censoring is important in clinical trials because patients can either die or potentially leave the trial. This procedure has subsequently been applied to datasets in other scientific fields, such as astronomy, where 'deaths' are replaced with measurements and patients who leave the trial are replaced with censored data, such as upper or lower limits (e.g. Young et al., 2011). This method of survival analysis allows us to determine statistical properties that are difficult to ascertain using classical methods when many of the measurements are censored.

For our sample of galaxies, we first use the Kaplan-Meier estimator to fit survival functions to our data. It is a non-parametric, maximum likelihood statistical estimator (Kaplan & Meier, 1958). In this study, we used the statistical package called SURVIVAL, which is written in R and can be found at the standard R repository[4]. Once we have fit a survival function to our dataset, we can then determine the modified versions of important statistical quantities. For example, we can find the 'median' value of the dataset by finding the point where the survival function is equal to 0.5 and the 'restricted mean' of the dataset by integrating the survival function to the last detected point.

To differentiate between survival functions and determine if they are significantly different from one another, we have used the log-rank test. The log-rank test was first introduced in Mantel (1966) and is often used to compare the effectiveness of new treatments in clinical trials. In our paper, we have applied survival analysis to the H_2 mass and its other derived quantities, such as the molecular gas depletion time (the H_2 gas mass divided by the star formation rate) and the stellar mass normalized H_2 mass. The use of survival analysis and the log-rank test for these cases has the primary advantage of incorporating all

[4] http://cran.r-project.org/web/packages/survival/index.html

the data collected, instead of discarding galaxies without CO detections. For non-censored datasets, we will use the standard Kolmogorov-Smirnov test for distinguishing between two distributions. An example of the application of the Kaplan-Meier estimator to the H_2 masses and the stellar mass normalized H_2 masses is presented in Figure 2.1, where the cumulative distribution functions are plotted.

The application of survival analysis to the total gas mass and its related quantities, such as the total gas depletion time (total gas mass divided by the star formation rate), presents one important difference compared to the H_2 gas mass alone. Since the galaxies without CO detections do have H I gas masses, it is not proper to treat galaxies without CO detections as pure upper limits for their total gas mass. Rather, they should be considered 'interval censored', where the true value is in between two values. In this case, the total gas mass for these galaxies would lie between their measured H I gas masses and the sum of their H I gas mass and the H_2 upper limit. For these datasets, we use the statistical package called INTERVAL, which can be found at the standard R repository[5]. The package also includes an implementation of the log-rank test routine ICTEST for interval censored data. In order to be consistent, we also use this particular INTERVAL routine for our left and right censored data as well. For those cases, we substitute in appropriate interval limits, such as -99 or 99 for the log upper and lower limits.

[5] http://cran.r-project.org/web/packages/interval/index.html

2.3 Results

2.3.1 Overview of Galaxy Properties in the Three Environments

The general properties of the galaxies in our sample, separated into field, group, and Virgo subsets, are presented in Table 2.2. The first three columns are mean H I mass, D_{25} sizes, and distances taken from the HyperLeda database, using velocities corrected for Virgo infall and assuming a cosmology of $H_o = 70$ km s^{-1} Mpc^{-1}, $\Omega_M = 0.27$, $\Omega_\Lambda = 0.73$. The next column is the CO detection rate for each individual sample, followed by the mean H_2 and H_2 + H I masses, with the calculations outlined in the previous section. Finally, we present the mean stellar mass for each of the samples.

The mean log H_2 mass, calculated from the Kaplan-Meier estimator of the survival function, is highest in the Virgo sample, followed by the field and group samples. The log-rank test on the group and Virgo samples shows a p-value of 0.0279, which suggests that there is a difference in the H_2 mass distributions between the two populations, when we take into account the censored data. For the case of atomic hydrogen, the mean H I mass is lowest for the Virgo galaxies, followed by the group and field samples. Relative H I deficiency of Virgo galaxies has been reported in previous studies of Virgo galaxies (e.g. Chamaraux et al., 1980; Haynes & Giovanelli, 1986; Solanes et al., 2001; Gavazzi et al., 2005), so it is not surprising to see this difference in our sample, even when we have selected based on a H I flux limit. The Kolmogorov-Smirnov test, performed for datasets that do not contain censored data, shows that

Table 2.2 Galaxy Properties as a Function of Environment

Type (# of galaxies)	$\overline{\log M_{HI}}$[1] ($M_\odot$)	$\overline{D_{25}}$[1] (kpc)	$\overline{\text{Distance}}$[1] (Mpc)	CO detection rate[2] (%)	$\overline{\log M_{H_2}}$[3] ($M_\odot$)	$\overline{\log M_{H_2+HI}}$[3] ($M_\odot$)	$\overline{\log M_*}$[1] ($M_\odot$)
Field (17)	9.23 ± 0.07	16.1 ± 1.8	20.1 ± 0.8	35 ± 9	8.17 ± 0.07	9.30 ± 0.06	9.58 ± 0.14
Group (42)	9.17 ± 0.04	13.1 ± 0.8	18.6 ± 0.7	40 ± 6	7.98 ± 0.08	9.24 ± 0.04	9.65 ± 0.07
Virgo (39)	8.99 ± 0.05	18.6 ± 2.0	16.7	54 ± 9	8.34 ± 0.13	9.17 ± 0.06	9.65 ± 0.11
CO Detected (44)	9.15 ± 0.05	19.9 ± 1.7	17.5 ± 0.5	100	8.61 ± 0.11	9.35 ± 0.05	9.97 ± 0.06
CO Non-Detected (54)	9.07 ± 0.04	12.5 ± 0.8	18.6 ± 0.5	0	(8.28 ± 0.06)[4]	(9.16 ± 0.03)[4]	9.36 ± 0.07

[1] Standard error of the means

[2] Binomial confidence intervals

[3] Restricted mean and standard errors from the Kaplan-Meier estimator of the survival functions

[4] Mean of the 2σ upper limits for the CO Non-Detected sample

the H I masses of the Virgo and group galaxies are not drawn from the same distribution, with a p-value of 4×10^{-4}.

The Virgo galaxies are all at the same assumed distance of 16.7 Mpc, while the group and field samples have larger mean distances. As a result, the Kolmogorov-Smirnov test reveals that the distribution in the distances of Virgo galaxies can be distinguished from both field and the group galaxies. Replacing the constant 16.7 Mpc with a Gaussian distributed sample with reasonable scatter does not change this result. Although the mean log total gas mass (H I + H_2) is slightly higher for the field galaxies, followed by the group, and Virgo samples, the difference is not statistically significant. The stellar masses of the Virgo and group samples are also quite similar, while the field galaxies have a lower mean value. The Kolmogorov-Smirnov test shows that the stellar mass distributions of the group and Virgo samples cannot be distinguished ($p = 0.4031$).

2.3.2 Group/Virgo Comparison

In Table 2.3, we present a summary of the properties of the group/Virgo, CO detected/CO non-detected samples, and a test case comparing the group and Virgo samples using CO detected galaxies only. In Table 2.4, we present the results from performing the Kolmogorov-Smirnov and log-rank statistical tests in order to determine whether the properties of the galaxies in these samples can be distinguished. We have decided to focus on the comparison between the group and Virgo samples, as they have roughly similar number of galaxies and CO detections, as compared to the field sample, which contains fewer galaxies.

Table 2.3 Selected Properties of the Group, Virgo, CO Detected, and CO Non-Detected Populations

Mean Quantity	Group (42)	Virgo (39)	CO Detected (44)	CO Non-Detected (54)
$\log M_{HI}$ $[M_\odot]$	9.17 ± 0.04	8.99 ± 0.05	9.15 ± 0.05	9.07 ± 0.04
$\log M_{H_2}$ $[M_\odot]$ [1]	7.98 ± 0.08	8.34 ± 0.13	8.61 ± 0.01	$(8.28 \pm 0.06)^2$
$\log M_*$ $[M_\odot]$	9.65 ± 0.07	9.65 ± 0.11	9.97 ± 0.06	9.36 ± 0.07
$\log M_{H_2+HI}$ $[M_\odot]$[1]	9.24 ± 0.04	9.17 ± 0.06	9.35 ± 0.05	$(9.16 \pm 0.03)^2$
M_{H_2}/M_{HI}[1]	0.23 ± 0.09	0.75 ± 0.20	0.87 ± 0.19	$(0.26 \pm 0.03)^2$
M_{H_2}/M_*[1]	0.033 ± 0.008	0.068 ± 0.010	0.07 ± 0.01	$(0.26 \pm 0.07)^2$
M_{HI}/M_*	0.52 ± 0.11	0.50 ± 0.12	0.22 ± 0.03	0.82 ± 0.12
M_{H_2+HI}/M_*[1]	0.57 ± 0.12	0.63 ± 0.14	0.29 ± 0.03	$(1.08 \pm 0.18)^2$
$\log \mathrm{SFR}$ $[M_\odot\ \mathrm{yr}^{-1}]$	-0.49 ± 0.07	-0.69 ± 0.11	-0.35 ± 0.09	-0.72 ± 0.07
$\log \mathrm{sSFR}$ $[\mathrm{yr}^{-1}]$	-10.14 ± 0.06	-10.34 ± 0.06	-10.32 ± 0.06	-10.08 ± 0.06
$\log M_{H_2}/\mathrm{SFR}$ [yr][1]	8.44 ± 0.07	8.97 ± 0.06	8.96 ± 0.08	$(9.00 \pm 0.08)^2$
$\log M_{HI}/\mathrm{SFR}$ [yr]	9.71 ± 0.07	9.67 ± 0.08	9.50 ± 0.07	9.79 ± 0.05
$\log M_{H_2+HI}/\mathrm{SFR}$ [yr][1]	9.73 ± 0.05	9.86 ± 0.07	9.70 ± 0.06	$(9.88 \pm 0.05)^2$

[1] Restricted mean and standard errors from the Kaplan-Meier estimator of the survival functions

[2] Mean of the 2σ upper limits for the CO Non-Detected sample

Future work will focus on further expanding the field sample and creating a sample of isolated galaxies, in order to incorporate these important objects into the analysis.

First, we consider the gas properties of the group and Virgo samples. The mean ratio of H_2 to H I gas mass is higher for the Virgo galaxies compared to the group galaxies. The log-rank test shows a significant difference in the distribution of the ratio of H_2 to H I between the Virgo sample and the field sample. This makes sense given that the Virgo galaxies have a lower mean H I gas masses and higher H_2 gas masses. This seems to follow the general trends from Kenney & Young (1989), who found that the Virgo galaxies are not as H_2 deficient as expected, given their H I deficiencies. The stellar mass normalized quantities, including the mean H_2 gas masses, generally follow the

Table 2.4 Significance Tests Between Different Samples

Mean Quantity	Group/Virgo	Group/Virgo (CO Det. Only)	CO Det./ Non-Det.
$\log M_{H\text{I}}$ $[M_\odot]$	$\mathbf{4 \times 10^{-4}}$	<u>0.0181</u>	0.7680
$\log M_{H_2}$ $[M_\odot]$	<u>0.0279</u>[1]	0.1635	–
$\log M_*$ $[M_\odot]$	0.6304	0.3090	$\mathbf{1 \times 10^{-9}}$
$\log M_{H_2+H\text{I}}$ $[M_\odot]$	0.7720 [1]	0.3653	–
$M_{H_2}/M_{H\text{I}}$	**0.0095** [1]	0.0786	–
M_{H_2}/M_*	<u>0.0272</u> [1]	0.1571	–
$M_{H\text{I}}/M_*$	0.1177	0.0622	$\mathbf{4 \times 10^{-7}}$
$M_{H_2+H\text{I}}/M_*$	0.7483 [1]	0.1571	–
$\log \text{SFR}$ $[M_\odot\ \text{yr}^{-1}]$	<u>0.0239</u>	0.2684	<u>0.0145</u>
$\log \text{sSFR}$ $[\text{yr}^{-1}]$	<u>0.0495</u>	0.1843	**0.012**
$\log M_{H_2}/\text{SFR}$ [yr]	**0.0034** [1]	**0.0036**	–
$\log M_{H\text{I}}/\text{SFR}$ [yr]	0.2406	0.4149	<u>0.0130</u>
$\log M_{H_2+H\text{I}}/\text{SFR}$ [yr]	0.0855 [1]	0.3090	–

[1] Restricted mean and standard errors from the Kaplan-Meier estimator of the survival functions

Note: Underline indicate $p < 0.05$ and values are bolded for $p < 0.01$

same trends as the unnormalized quantities. The difference between the stellar mass normalized H I mass distribution of the group and Virgo galaxies is not as significant as for the unnormalized case. The higher H_2 to H I ratio in the Virgo sample may indicate that these galaxies are more efficient at converting available H I to H_2, perhaps through the various forms of interactions that lead to gas flowing towards the centre of host galaxies and the creation of molecular hydrogen. An alternative explanation is that the cluster environment is more effective at stripping the H I rather than the H_2 gas and thus increasing the global H_2 to H I ratio (Pappalardo et al., 2012). These ideas will be explored in future studies with the resolved data.

With the Hα data available for our galaxies, we can determine the star formation rates and specific star formation rates (star formation rate divided by stellar mass) for our galaxies. We find that both values are lower for Virgo galaxies, compared to the group galaxies. However, the Kolmogorov-Smirnov test shows that while the star formation rate distributions can be distinguished between the group and Virgo samples at higher significance than the specific star formation rates.

A method of measuring the relationship between star formation and the gas content of galaxies is through the gas depletion timescale (M_{H_2}/SFR [yr]) or its reciprocal, the star formation efficiency (SFR/M_{H_2} [yr^{-1}]). The mean log molecular gas depletion timescale is longer for the Virgo sample (8.97 ± 0.06) than for the group sample (8.44 ± 0.07), with the log-rank test showing that the Virgo galaxies can be distinguished from the group galaxies at the $p = 0.01$ level. This is shown graphically in Figure 2.2, where we see large differences in the shapes of the cumulative distribution functions. For the case where we only consider CO detected galaxies from the group and Virgo sample, the differences are still significant. When we calculate the gas depletion times with respect to the atomic hydrogen gas mass or the total gas mass (H_2 + H I), the two samples have similar distributions.

One possible explanation for this difference is metallicity effects on the X_{CO} value, as discussed in Section 2.2.2. If Virgo galaxies have systematically different metallicities than group galaxies, then that would have an effect on the molecular gas mass and hence the gas depletion times. The similar mean stellar mass of the two samples suggests any metallicity effects should not be significant. Other differences in the ISM properties, such as temperature or surface density, would also cause changes in the measured molecular gas mass, assuming a variable X_{CO} conversion factor prescription (Bolatto et al., 2013). However, it seems unlikely that Virgo spirals would have the extreme temperatures or surface densities required to cause a substantial difference in the X_{CO} factor.

Another explanation for the variations in the molecular gas depletion time is that star formation may be inhibited in the more extreme cluster environment, even in the presence of a comparable or even higher amount of H_2 gas, due to other mechanisms such as increasing thermal support in the gas. Turbulent pressure can play a large role in regulating star formation (Krumholz et al., 2009) and this pressure is likely to be different between the three environments. For example, studies of the dense gas tracer HCN in nearby disk galaxies from the HERACLES survey found variations in the star formation efficiency with environment and towards the centre of galaxies (Usero et al., 2015). The authors suggests models where such variations are caused by differences in the Mach number, which can also apply to the Virgo cluster environment. For example, Alatalo et al. (2015) found an increased ^{13}CO/^{12}CO ratio in early-type galaxies in the Virgo cluster, which they attribute to enrichment due to low-mass stars or to variations in the gas pressure in the dense environment. Another possibility is differences in the gravitational stability of spiral disks, which can be parametrized by the Toomre Q parameter (Toomre, 1964; Kennicutt, 1989). Close neighbors and the additional pressure from the cluster environment may cause changes in the disks of spiral galaxies and its star formation efficiency.

Comparing to previous surveys, we note that Leroy et al. (2008) found a constant value of the molecular gas depletion timescale of $(1.90 \pm 0.4) \times 10^9$ (or $\sim 10^{9.27}$) years using resolved maps of 23 galaxies from the HERACLES survey with CO $J = 2-1$ line, FUV + IR star formation rates, and a Kroupa IMF. The study of a sample of 30 galaxies from the HERACLES survey found a H_2 depletion timescale of 2.2×10^9 (or $\sim 10^{9.34}$) years (Leroy et al., 2013). This value is longer than our integrated values for our group and Virgo samples. The COLD GASS survey (Saintonge et al., 2011) found a molecular gas depletion time of ~ 1 Gyr, varying between ~ 0.5 Gyr for low-mass galaxies ($\sim 10^{10} M_{\odot}$) to ~ 3 Gyr for high-mass galaxies ($\sim 10^{11} M_{\odot}$). This is more similar to the results from the analysis of our sample of galaxies.

One reason for the variations in the molecular gas depletion time between our sample and the HERACLES survey may be the difference between integrated and resolved measurements. We have calculated a single value of the molecular gas depletion time for the entire galaxy, as compared to performing pixel by pixel measurements. Leroy et al. (2013) found a median gas depletion time of 2.2 Gyr when weighted by individual measurements, but a lower value of 1.3 Gyr (or $\sim 10^{9.11}$ years) when weighted by galaxy. Second, the presence of lower mass galaxies in our sample could be driving down the mean molecular gas depletion timescale. This is because we are weighting all galaxies equally in this analysis, whereas resolved measurements are dominated by the measurements from larger, higher mass galaxies. Third, our use of the CO $J = 3-2$ line may be another reason, since that line traces a smaller fraction of the molecular gas than the CO $J = 2-1$ line, mainly the warmer and denser component. Although we have included an average line ratio in our calculations, we may still be missing some of the more diffuse gas in the disk. A fourth possibility is the difference in the star formation rate indicator (Hα + extinction correction vs. FUV + IR), though it seems unlikely that the FUV + IR would provide systematically lower star formation rates. This is because the FUV component measures star formation on a longer timescale and both the FUV and IR have contributions not related to recent star formation (Kennicutt & Evans, 2012). Finally, the Hα emission may not fully coincide with the results from the CO maps, which for most observations were concentrated in the inner 2 arcminutes of the galaxy. This may lead to a higher star formation rate (measured over a larger portion of the galaxy) as compared to its gas content. A future extension to this project will look at resolved measurements for the galaxies in this sample, which will then create a more consistent comparison and may help resolve any differences.

2.3.3 CO Detected/Non-Detected Comparison

There are 44 CO detected galaxies in our sample, including 6 field galaxies, 17 group galaxies, and 21 Virgo galaxies. There are 54 CO non-detected galaxies, including 11 field galaxies, 25 group galaxies, and 18 Virgo galaxies. Looking at their gas properties, the two samples have roughly the same H I gas mass, which suggests the lack of a strong correlation between H_2 and H I gas masses in our H I - flux selected sample. The CO detected sample has a larger average stellar masses than the CO non-detected sample, as seen in the left panel of Figure 2.3. There is a very significant difference between their stellar mass distributions, with a corresponding p-value of 1×10^{-7}. The relation-

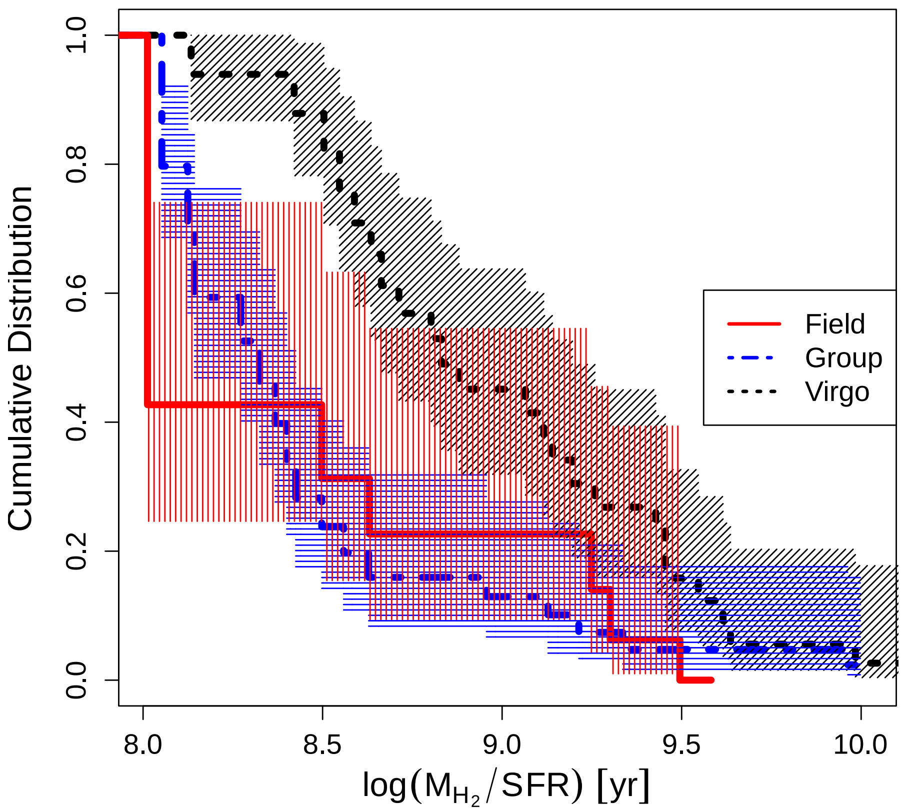

Figure 2.2 Survival functions for the molecular gas depletion time in the field (red solid line), group (blue dot-dash line), and Virgo (black dashed line) sample galaxies using the Kaplan-Meier estimator. The 'steps' in the distribution correspond to detections. The 95% confidence intervals are overlaid for the three distributions.

ship between the stellar mass and CO detection would be expected if the H_2 gas mass is well-correlated with the stellar mass, which has also been seen in Boselli et al. (2014).

We also find that the upper limits for the H_2 and total gas mass in CO non-detected galaxies are lower than the corresponding values for the CO detected sample. However, the results are not as conclusive when considering the stellar mass normalized values. This is likely due to the large difference in the stellar mass of the two samples, with the CO detected galaxies being much more massive than the non-detected galaxies. This results in stellar-mass normalized H_2 and total gas masses that are comparable to the upper limits for CO detected sample. We will need more data to determine if there are any systematic differences between the two samples.

The mean log star formation rate is higher in the CO detected galaxies than in the CO non-detected galaxies (log SFR [$M_\odot$ yr^{-1}] of -0.35 ± 0.09 vs. -0.72 ± 0.07). The corresponding p-value for the Kolmogorov-Smirnov test between the two distributions is 0.0145. This difference in the star formation rates between the two samples is likely caused by the correlation between star formation rate and molecular gas, the material required to form stars. With the stellar masses of the CO detected galaxies substantially higher than those of the CO non-detected galaxies, the Kolmogorov-Smirnov test show a difference in the distribution of sSFR between the two samples, which can also be seen in the right panel of Figure 2.3. This is likely a consequence of the well-known negative correlation between stellar mass and specific star formation rate for star forming galaxies. Finally, the H I gas depletion times are longer in the

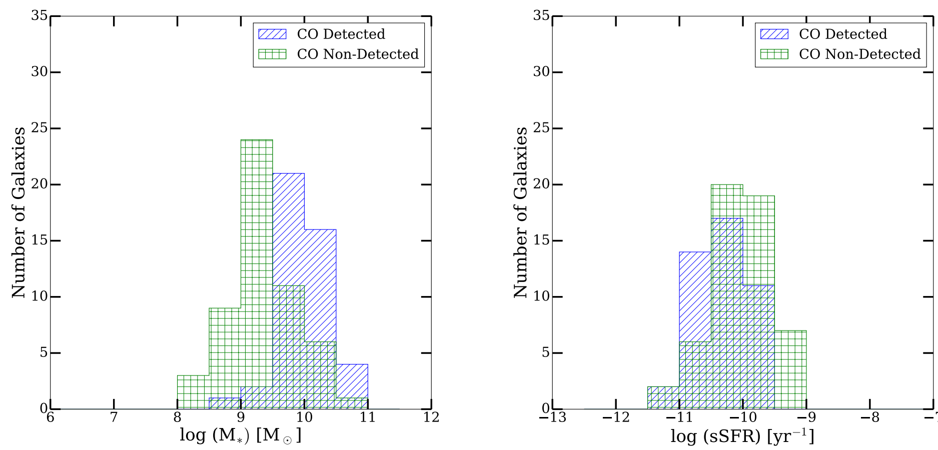

Figure 2.3 **Left:** A histogram showing the significant difference between the stellar mass distributions of the CO detected and non-detected samples ($p = 1 \times 10^{-9}$). **Right:** A histogram showing the difference in the sSFR distribution between the CO detected and non-detected samples ($p = 0.012$).

CO non-detected galaxies compared to the CO non-detected galaxies. This is likely also due to the significant difference in their star formation rates.

2.3.4 CO $J = 3-2$ Detection Rates

The overall detection rate for the sample is 44 per cent. The CO $J = 3-2$ detection rate is slightly lower for the field (35 ± 9 per cent) sample, as compared to the group (40 ± 6 per cent) and Virgo (54 ± 9 per cent) samples. Some of the factors that would cause this difference include the Virgo galaxies being on average closer than the group and field galaxies, which can influence the CO detection rates, since closer galaxies would be easier to detect. Another important factor is sample variance and the smaller number of field galaxies in our sample, only 17 in total. As a result, the detection or non-detection of one or two galaxies can have a large influence on the CO detection rate.

We note that the stellar mass for the field sample is on average lower than the Virgo and group samples. Given the correlation between stellar mass and molecular gas mass (Lisenfeld et al., 2011; Boselli et al., 2014), this difference in the stellar mass will contribute to the difference in the detection rates. These low stellar mass galaxies (below $\sim 10^9 M_\odot$) may even be considered dwarf spirals according to the stellar mass classification from other galaxy surveys (Geha et al., 2012). In addition, if any galaxies in our sample are metal poor, this would also affect the H_2 mass we estimate via the metallicity dependence of the CO-to-H_2 conversion factor (Wilson, 1995), as well as the detection rate. The stellar mass distribution of our field, group, and Virgo sample, with the majority of our galaxies in the mass range of $10^9 - 10^{11} M_\odot$, combined with the observed mass-metallicity relationship fit (Tremonti et al., 2004), would lead to (12 + log(O/H)) values of between $8.63 - 9.11$. It is likely that few of these galaxies have metallicities more than a factor of two below solar (12 + log(O/H) = 8.69), the rough limit at which any metallicity effects would become significant (Wilson, 1995; Arimoto et al., 1996; Israel, 2000; Bolatto et al., 2008).

Finally, the redshift-limited (recessional velocities of between 1500 and 5000 km s^{-1}) AMIGA survey of isolated galaxies detects $51\pm5\%$ in the CO $J = 1-0$ line, a detection rate similar to our Virgo samples and slightly higher than our overall sample (Lisenfeld et al., 2011). In comparison to our sample, their stellar masses (measured by L_K) are roughly in the range of $10^8 - 10^{11} M_\odot$,

Table 2.5 Selected Properties of the Early-type Spiral, Late-Type Spiral, Pair, and Non-Pair Populations

Mean Quantity	Early-type Spirals (40)	Late-type Spirals (57)	Pair (14)	Non-Pair (84)
$\log M_{HI}$ $[M_\odot]$	9.13 ± 0.05	9.09 ± 0.04	9.06 ± 0.08	9.11 ± 0.03
$\log M_{H_2}$ $[M_\odot]$[1]	8.36 ± 0.08	8.00 ± 0.07	8.47 ± 0.13	8.06 ± 0.07
$\log M_*$ $[M_\odot]$	9.86 ± 0.08	9.49 ± 0.07	9.79 ± 0.11	9.61 ± 0.06
$\log M_{H_2+HI}$[1]	9.50 ± 0.07	9.25 ± 0.07	9.36 ± 0.08	9.35 ± 0.06
M_{H_2}/M_{HI}[1]	0.63 ± 0.18	0.28 ± 0.10	1.09 ± 0.48	0.31 ± 0.07
M_{H_2}/M_*[1]	0.055 ± 0.010	0.038 ± 0.007	0.066 ± 0.016	0.041 ± 0.006
M_{HI}/M_*	0.32 ± 0.06	0.70 ± 0.11	0.31 ± 0.07	0.59 ± 0.08
M_{H_2+HI}/M_*[1]	0.40 ± 0.07	0.80 ± 0.13	0.38 ± 0.07	0.67 ± 0.09
$\log SFR$ $[M_\odot$ yr$^{-1}]$	-0.44 ± 0.09	-0.62 ± 0.08	-0.46 ± 0.11	-0.57 ± 0.07
$\log sSFR$ [yr^{-1}]	-10.30 ± 0.07	-10.10 ± 0.06	-10.26 ± 0.12	-10.18 ± 0.05
$\log M_{H_2}/\mathrm{SFR}$ [yr][1]	8.68 ± 0.10	8.55 ± 0.06	8.85 ± 0.20	8.57 ± 0.06
$\log M_{HI}/\mathrm{SFR}$ [yr]	9.57 ± 0.07	9.70 ± 0.05	9.52 ± 0.12	9.68 ± 0.05
$\log M_{H_2+HI}/\mathrm{SFR}$ [yr][1]	9.73 ± 0.06	9.79 ± 0.05	9.73 ± 0.11	9.78 ± 0.04

[1] Restricted mean and standard errors from the Kaplan-Meier estimator of the survival functions

similar in mass to than our sample. Their sample of isolated galaxies is based on the catalogue of Karachentseva (1973) and is chosen to possess no nearby similarly sized neighbours in the sky.

2.4 Discussion

2.4.1 Effects of Morphology

Morphology can have a large effect on the star formation (Kennicutt, 1998a; Bendo et al., 2007) and the molecular gas properties (Kuno et al., 2007) of spiral galaxies. For our sample of galaxies, we have performed a simple comparison of the early-type spirals (a, ab, b, and bc) with the late-type spirals (c, cd, d, and m). As stated in the discussion of our sample selection in Sec-

Table 2.6 Significance Test Between Different Samples

Mean Quantity	Early/Late	Pair/Non-Pair
$\log M_{H\text{I}}$ $[M_\odot]$	0.6553	0.9524
$\log M_{H_2}$ $[M_\odot]^1$	0.0614	0.1799
$\log M_*$ $[M_\odot]$	**0.0013**	0.4489
$\log M_{H_2+H\text{I}}$ $[M_\odot]^1$	0.0504	0.8574
$M_{H_2}/M_{H\text{I}}{}^1$	0.0976	**0.0098**
$M_{H_2}/M_*{}^1$	0.3055	0.1971
$M_{H\text{I}}/M_*$	**0.0014**	<u>0.0450</u>
$M_{H_2+H\text{I}}/M_*{}^1$	<u>0.0066</u>	0.2072
$\log SFR$ $[M_\odot\ \text{yr}^{-1}]$	0.4178	0.4489
$\log sSFR$ $[\text{yr}^{-1}]$	0.0620	0.5856
$\log M_{H_2}/\text{SFR}$ $[\text{yr}]^1$	0.1249	<u>0.0163</u>
$\log M_{H\text{I}}/\text{SFR}$ $[\text{yr}]$	0.2626	0.5856
$\log M_{H_2+H\text{I}}/\text{SFR}$ $[\text{yr}]^1$	0.4890	0.8262

[1] Restricted mean and standard errors from the Kaplan-Meier estimator of the survival functions

Note: Underline indicate $p < 0.05$ and values are bolded for $p < 0.01$

tion 2.2.1, we used the HyperLeda morphological codes for this classification, which employs a weighted average of multiple measurements. One galaxy classified as S?, NGC3077, is excluded from this analysis. In total, there are 40 early-type spirals and 57 late-type spirals. Selected properties for the two samples are presented in Table 2.5, as well as the results from the significance tests in Table 2.6.

The Kolmogorov-Smirnov test shows a significant difference in the stellar mass ($p = 0.0013$), with the mean value being higher for early-type spirals. This results in significantly lower stellar mass normalized H I gas masses and total gas masses for the sample. On the other hand, the Kolmogorov-Smirnov test shows that the distributions of H I mass, star formation rates, and the specific star formation rates are not significantly different between the two samples. Furthermore, the mean molecular gas mass and the molecular gas depletion times are not significantly different between the two samples. This suggests that variations between the early- and late-type spirals in this study should not be an important contributor to the differences observed between the group and Virgo samples.

2.4.2 Effects of Close Pairs

Interacting galaxies and mergers have been linked to more active star formation in their nucleus (Keel et al., 1985) and can lead to inflows of gas towards the centre (Mihos & Hernquist, 1996), increased cooling, and greater fragmentation (Teyssier et al., 2010). From a large sample of SDSS galaxies, Ellison et al. (2008) found that there is a slight statistical enhancement in the star formation rate for close pairs. This enhancement is also seen for cases where these pairs actually undergo mergers and interactions (Knapen & James, 2009; Knapen et al., 2015). However, this effect may be less apparent for galaxies that are inside denser environments (Ellison et al., 2010). Therefore, we decided to investigate the effects on our results of removing any close pairs from the sample. Once again, we use the catalog of Karachentsev (1972) to compare galaxies known to be in pairs with their non-pair counterparts. For the group sample, there are 5 galaxies in pairs (NGC0450, NGC2146A, NGC3507, NGC3455, NGC4123) . For the Virgo sample, there are 9 galaxies in pairs (NGC4294, NGC4298, NGC4302, NGC4411A, NGC4430, NGC4561, NGC4567, NGC4568, NGC4647). Of these, 3 out of the 5 group galaxies and 5 out of 9 of the Virgo galaxies are CO detected. Note that for the galaxies in the Virgo cluster, close pairs may not be true interacting galaxies, due to the close proximity of these galaxies in the sky.

For most of the galaxy properties in this study, such as the stellar mass and atomic gas properties, the pair and non-pair samples are not significantly different. However, the H_2 to H I gas mass ratio is higher and the H_2 gas depletion time is longer in the pair sample. From the significance tests in Table 2.6, the p-values are indicative of a significant difference between the two samples. These differences in the H_2 gas depletion time and the H_2 to H I gas mass ratio are similar to those found when comparing between the group and Virgo galaxies. The various environmental effects, such as stripping of the atomic hydrogen in the outskirts and the interaction effects on the molecular gas, may also occur for the more extreme cases of close pairs.

We have also tested removing these pairs from our group and Virgo samples. Most of the results from our comparison of group and Virgo samples remain the same, such as the stellar masses and atomic gas properties. Virgo galaxies still possess a slightly higher mean molecular gas mass. On the other hand, while the H_2 to H I ratio is higher for Virgo galaxies at 0.48 ± 0.14 compared to 0.25 ± 0.10 for the group galaxies, with the pairs removed the log-rank no longer shows a significant difference between the two distributions ($p = 0.1136$). Similarly, the mean log H_2 gas depletion times [yr] for the Virgo galaxies is longer at 8.97 ± 0.06 compared to 8.44 ± 0.07 for the group sample, but now with a log-rank test value of $p = 0.079$.

These results suggest that these environmental trends in H_2 to H I ratio and H_2 gas depletion times are similar when we make the comparison between the group/Virgo and between the pair/non-pair populations. Removing the presence of the Karachentsev (1972) pairs reduces the overall significance of the differences found between the group and Virgo samples. Physically, the environmental effects discussed in the previous section will likely be amplified for the galaxies that are strongly interacting. The question remains whether the observed variations in the molecular gas and star formation properties in the cluster environment affect all galaxies or whether the difference is mainly due to the denser environment producing more close pairs? A more systematic analysis is require to fully disentangle these two effects, such as increasing the number of galaxies in our sample, the use of a more rigorous method of defining pairs, and observing trends with distance to the cluster center or with multiple nearby clusters (such as the Fornax Cluster).

2.4.2.1 H I Rich Galaxies

We have used the less traditional H I flux as the primary selection in our sample of galaxies. As a result, our full sample includes many galaxies with normal H I mass, but low stellar mass. We can see their presence most readily in the CO non-detected sample or by looking at the specific galaxies with high H I gas mass to stellar mass ratios. In general, these objects will likely be missed by optically-selected surveys and may even exist as an understudied class of galaxies. Similar H I rich objects have been observed recently by the Bluedisks project (Wang et al., 2013) and HIghMass survey (Huang et al., 2014). The HIghMass survey galaxies have high H I gas mass ($M_{HI} > 10^{10} M_\odot$) and high H I fractions compared to galaxies with the same stellar mass. After measuring their star formation rates, they found that the HIghMass galaxies have comparatively high specific star formation rates, which the authors attribute to their more recent formation times. The CO non-detected galaxies in our sample possess similar qualities, with lower stellar masses, high H I to stellar mass ratios, and higher specific star formation rates compared to the CO detected galaxies.

2.4.3 Correlation between Galaxy Properties

We seek to determine the important scaling relationships among the galaxies in our sample by plotting the different physical properties and identifying any possible correlations. For this analysis, we have chosen to use a simple linear fit to the CO detected galaxies, since the measurement errors on these galaxy properties are small compared to the scatter in the data points. To take into account the effects of data censoring for values along the y-axis, the Buckley-James estimator was used (Buckley & James, 1979). To perform the Buckley-James regression, we used the subroutine Bj in the statistical package called Rms, which can be found at the standard R repository[6]. We have decided to use the Buckley-James regression in our analysis because of its similarity to survival analysis, with both techniques attempting to incorporate upper limits into the statistical treatment.

First, we present the relationship between stellar mass and molecular gas mass in Figure 2.4, which shows a positive correlation between the two parameters, with a slope of 1.49 ± 0.15. This result indicates that the more massive

[6] http://cran.r-project.org/web/packages/rms/index.html

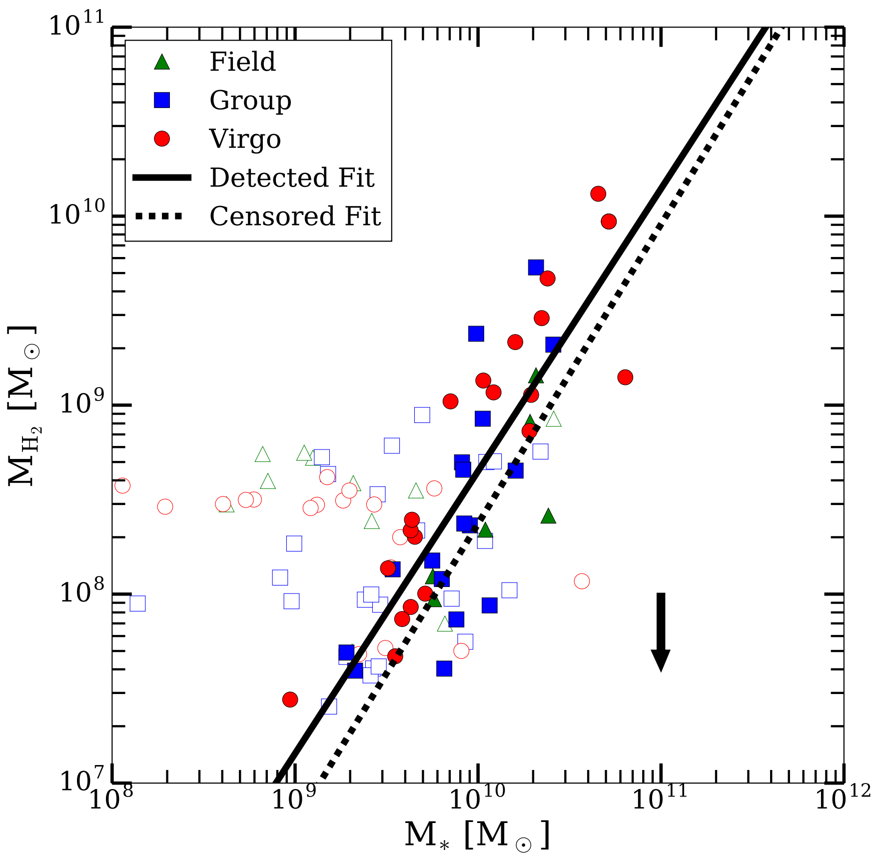

Figure 2.4 The molecular gas mass as a function of the stellar mass for the field, group, and Virgo sample. Filled points are detections while open points are upper limits, with the direction indicated by the large black arrow and a length of 1σ. Also plotted are the linear fit to the detected galaxies in the entire sample, with a slope of 1.49 ± 0.15. The Pearson coefficient is 0.84 ($p = 7 \times 10^{-13}$). The Buckley-James fit produced a slope of 1.58 ± 0.15. This relationship between the molecular gas mass and the stellar mass have been seen in previous survey for spiral galaxies (Lisenfeld et al., 2011; Boselli et al., 2014).

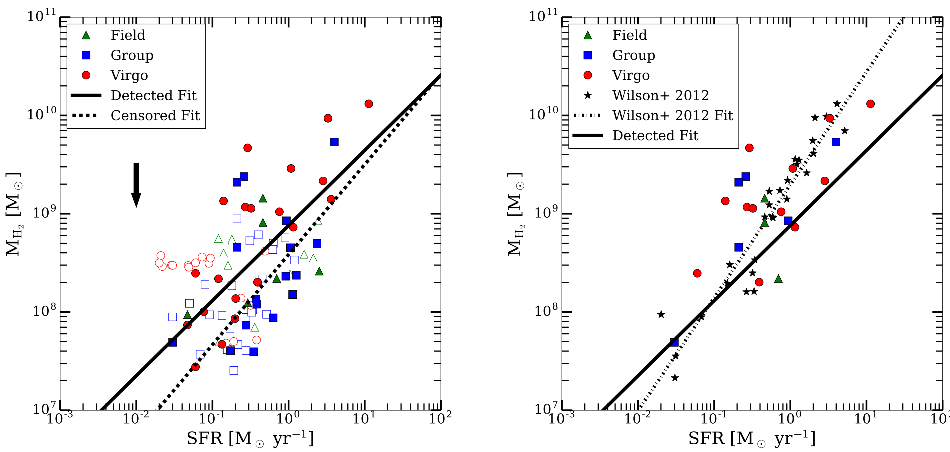

Figure 2.5 **Left:** The molecular gas mass as a function of the star formation rate for the field, group, and Virgo sample. Filled points are detections while open points are upper limits, with the direction indicated by the large black arrow and a length of 1σ. Also plotted are the linear fit to the detected galaxies in the entire sample, with a slope of 0.76 ± 0.14. The corresponding Pearson coefficient is 0.64 ($p = 4 \times 10^{-6}$). The Buckley-James (censored) fit produced a slope of 0.92 ± 0.15. **Right:** The molecular gas mass as a function of the star formation rate for the field, group, and Virgo sample, only including galaxies with a CO S/N ratio greater than 5. Also plotted in black stars are the smaller sample of galaxies from Wilson et al. (2012), which includes all NGLS galaxies that are also part of the Spitzer Infrared Nearby Galaxy Survey, with star formation rates are measured using FIR fluxes. The dotted line is the linear fit to the galaxies from Wilson et al. (2012) ($m = 1.149 \pm 0.005$), with the solid black line from the detected fit to the whole sample plotted for comparison purposes.

galaxies in our sample contain more molecular gas and has been seen previously in Lisenfeld et al. (2011) for late-type galaxies. Boselli et al. (2014), using the Herschel Reference Survey, have also noted relatively constant M_{H_2}/M_* ratios for spiral galaxies. On the whole, this result suggests that those galaxies with more stars have more fuel for future star formation.

Next, we show the relationship between the molecular gas mass and the star formation rate, which is similar to other analyses based on the Kennicutt-Schmidt law (Kennicutt, 1998b). From the left panel in Figure 2.5, we find a considerable scatter around the fit. One difference from similar studies is the use of the CO $J = 3 - 2$ line, which traces denser and warmer molecular gas when compared to the lower transition CO lines. The use of CO and Hα measurements covering different portions of the galaxies, as discussed when comparing integrated H_2 gas depletion times with other surveys, may also contribute to the scatter. Note that we have presented the plot as M_{H_2} vs star formation rate, since our method of calculating the censored data fit only allows for censoring for the variable in the y-axis. Previous studies of resolved molecular gas and star formation rate measurements have found a slope near unity (Bigiel et al., 2008; Leroy et al., 2013), though other groups have found larger values for the slope of the star formation rate vs. molecular gas mass (Kennicutt et al., 2007).

To determine the main cause of the large scatter, we have compared our results to an earlier paper in this series in the right panel of Figure 2.5. The previous paper focused on NGLS galaxies that are also found in the SINGS (Spitzer Infrared Nearby Galaxies Survey) sample. The star formation rates in Wilson et al. (2012) are measured using FIR fluxes instead of Hα measurements, but they have been converted into star formation rates with the SF conversion factor from Kennicutt & Evans (2012), also assuming a Kroupa IMF. The galaxies from our larger sample seem to follow the same trend as the galaxies from Wilson et al. (2012), though with a much larger scatter. This scatter could be due to the marginal nature of some of our CO detections, as we have selected all galaxies with a S/N ratio > 3. When we plot this relationship including only the galaxies in this paper with S/N > 5, we find that the scatter is reduced, though not to the level from the Wilson et al. (2012) paper.

In addition, we can also look at the trends in the H_2 gas depletion time (molecular gas mass divided by the star formation rate) for the galaxies in our sample. In Figure 2.6, we find that there is a positive correlation between the molecular gas depletion time and the stellar mass, a result also noted in other surveys (Saintonge et al., 2011). The Pearson correlation parameter using the detected galaxies is 0.30, which is weaker than the other correlations presented in this study. However, the p-value from the correlation is 0.047, which is a strong hint that a correlation does exist. Saintonge et al. (2011) provide three possible explanations: bursty star formation in low mass galaxies reducing the star formation rates, a quenching mechanism that reduces the star formation efficiency in high mass galaxies, and/or observations not detecting a larger fraction of molecular gas in low mass galaxies. Other groups, such as Leroy et al. (2008), have not found any significant correlations between molecular gas depletion time and stellar mass. Furthermore, it has been suggested that

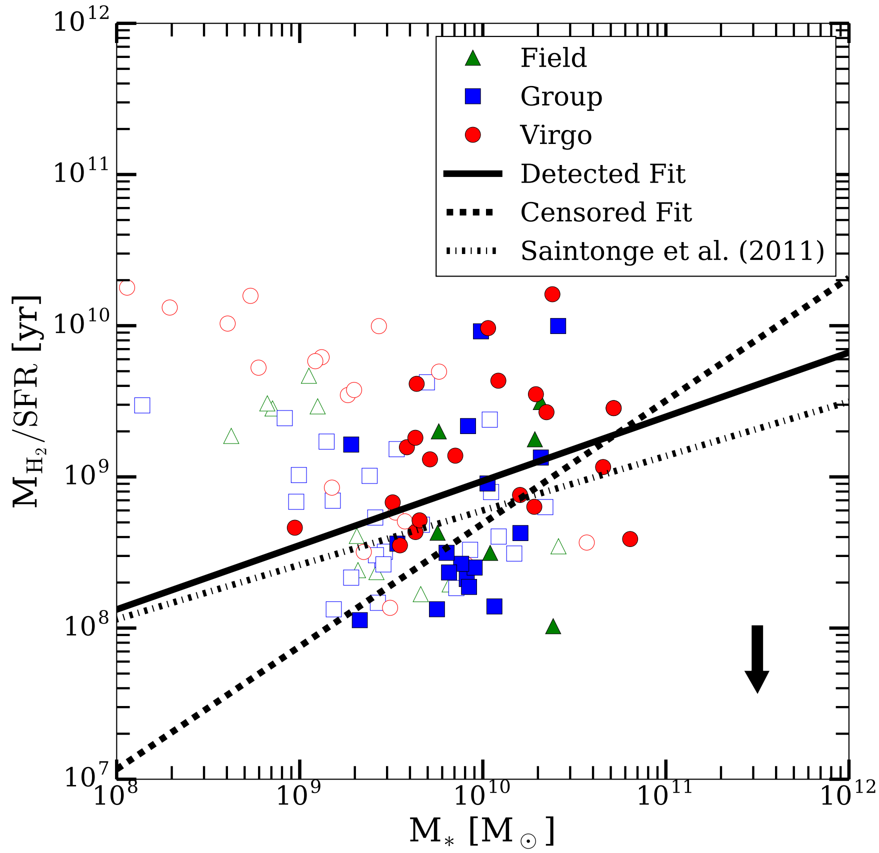

Figure 2.6 The molecular gas depletion time as a function of stellar mass for the field, group, and Virgo sample. Filled points are detections while open points are upper limits, with the direction indicated by the large black arrow and a length of 1σ. Also plotted are the linear fit to the detected galaxies in the entire sample, with a slope of 0.42 ± 0.21 and a Pearson coefficient of 0.30 ($p = 0.047$). The Buckley-James fit produced a steeper slope of 0.81 ± 0.22. The results are compared to the fit from Saintonge et al. (2011) for a sample of 222 galaxies.

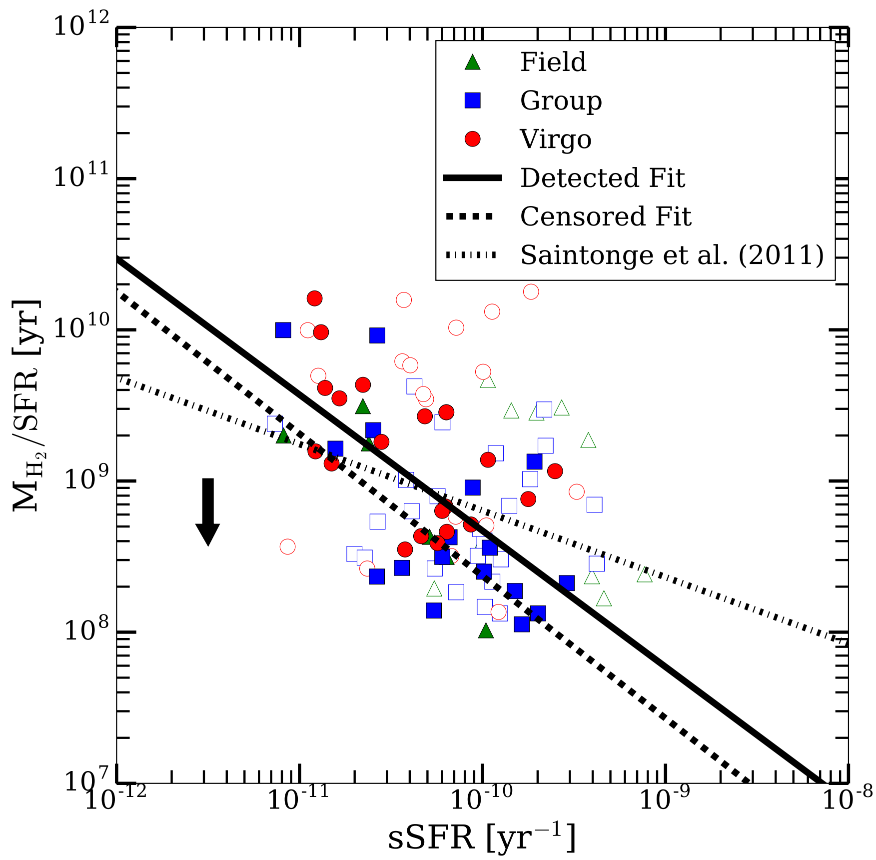

Figure 2.7 The molecular gas depletion time as a function of the specific star formation rate for the field, group, and Virgo sample. Filled points are detections while open points are upper limits, with the direction indicated by the large black arrow and a length of 1σ. Also plotted are the linear fit to the detected galaxies in the entire sample, with a slope of -0.90 ± 0.17 and a Pearson coefficient of -0.65 ($p = 2 \times 10^{-6}$). The Buckley-James fit produced a slope of -0.94 ± 0.16. The results are compared to the fit from Saintonge et al. (2011) for a sample of 222 galaxies.

this correlation would disappear with a mass-dependent CO conversion factor (Leroy et al., 2013).

Finally, in order to tie together three of the main parameters from our study (star formation, molecular gas mass, stellar mass), we explore the correlation between the specific star formation rate (sSFR) and the molecular gas depletion time. In Figure 2.7, we note a negative correlation between those two parameters, consistent with results from Saintonge et al. (2011), Huang & Kauffmann (2014), and Boselli et al. (2014). This correlation suggests that molecular gas is depleted more quickly in galaxies with high specific star formation rates (a high current star formation compared to their stellar mass). In other words, the molecular gas depletion times inside galaxies are dependent on the fraction of new stars compared to the old stellar population. A related study by Kannappan et al. (2013) looked at the tight relationship between the fractional stellar mass growth rate (the mass of new stars formed over the past ~ 1 Gyr) and the gas to stellar mass ratio, which is suggestive of a link between the amount of new stars formed, the old stellar component, and the amount of gas available.

We note that the correlations found between the different galaxy properties in our sample were largely unchanged after subdividing between the group and Virgo sample, as seen in Figure 2.6 and Figure 2.7. The differences in slopes of the total sample and slopes of the group and Virgo sub-samples are within their respective error bars while the differences in the intercepts of these relations are likely related to the variations observed in the properties of the group and Virgo samples in the previous sections.

2.5 Conclusions

This paper presents the results of an analysis of an H I flux limited sample of 98 spiral galaxies from the Nearby Galaxies Legacy Survey (NGLS), a Virgo follow-up program, and selected galaxies from the Herschel Reference Survey (HRS). The sample was further subdivided into group and Virgo galaxies in order to determine any possible environmental effects. We studied their molecular gas content through CO $J = 3-2$ observations using the James Clerk Maxwell Telescope (JCMT) and star formation properties using Hα measurements. We have also used survival analysis in order to incorporate data from galaxies with only upper limits on their CO measurements.

- The overall CO $J = 3-2$ detection rate for the galaxies in our sample is 44 per cent. The CO detected galaxies have a larger mean stellar mass and star formation rate compared to the CO non-detected galaxies. On the other hand, the mean specific star formation rates and H I gas masses are similar between the two samples.

- The mean log H I mass is larger for group galaxies compared to the Virgo galaxies, with the Kolmogorov-Smirnov test showing that the distribution of H I masses in the Virgo and group galaxies are significantly different. Conversely, the H_2 masses are higher in the Virgo compared to the group sample. As a result, the Virgo galaxies possess a significantly higher H_2 to H I ratio than the group sample. These galaxies inside the cluster may be better at converting their H I gas into H_2 gas, perhaps due to environmental effects on inflows towards the centre or the H_2 gas not being stripped as efficiently as the H I gas.

- The mean log molecular gas depletion time (M_{H_2}/SFR [yr]) is longer in the Virgo sample (8.97 ± 0.06) compared to the group (8.44 ± 0.07) sample. This difference in the molecular gas depletion time may be a combination of environmental factors that both increase the H_2 gas mass, as discussed in the previous point, and decrease the star formation rate in the presence of large amounts of molecular gas, such as heating processes in the cluster environment or differences in turbulent pressure (Usero et al., 2015; Alatalo et al., 2015).

- The molecular gas depletion time (M_{H_2}/SFR) depends positively on the stellar mass and negatively on the specific star formation rate, consistent with previous studies on these relationships (Saintonge et al., 2011; Boselli et al., 2014). Higher mass galaxies have a longer molecular gas depletion time, i.e., they are converting their molecular gas to stars at a slower rate. This may be caused by more bursty star formation in low mass galaxies and/or quenching mechanisms in higher mass galaxies, as suggested by Saintonge et al. (2011). We find that galaxies with high specific star formation rates have shorter molecular gas depletion times, suggesting that galaxies with high star formation rates relative to their stellar populations would run out of fuel faster and may be undergoing a different and less sustainable star formation process. This is similar to results from other studies, including a large survey with nearby and high redshift galaxies, where Genzel et al. (2015) found that the gas depletion time depends most strongly on a galaxy's sSFR relative to the sSFR of the star-formation main sequence.

2.6 Acknowledgments

We wish to thank the referee for their thorough review and useful suggestions. The James Clerk Maxwell Telescope has historically been operated by the Joint Astronomy Centre on behalf of the Science and Technology Facilities Council of the United Kingdom, the National Research Council of Canada and the Netherlands Organisation for Scientific Research. The research of C.D.W. is supported by grants from NSERC (Canada). We acknowledge financial support to the DAGAL network from the People Programme (Marie Curie Actions) of the European Union's Seventh Framework Programme FP7/2007-2013/ under REA grant agreement number PITN-GA-2011-289313, and from the Spanish Ministry of Economy and Competitiveness (MINECO) under grant number AYA2013-41243-P.

We acknowledge the usage of the HyperLeda database (http://leda.univ-lyon1.fr). This research has made use of the NASA/IPAC Extragalactic Database (NED) which is operated by the Jet Propulsion Laboratory, California Institute of Technology, under contract with the National Aeronautics and Space Administration. This publication makes use of data products from the Wide-field Infrared Survey Explorer, which is a joint project of the University of California, Los Angeles, and the Jet Propulsion Laboratory/California Institute of Technology, funded by the National Aeronautics and Space Administration. This work is based [in part] on archival data obtained with the Spitzer Space Telescope, which is operated by the Jet Propulsion Laboratory, California Institute of Technology under a contract with NASA. Support for this work was provided by an award issued by JPL/Caltech.

The Digitized Sky Surveys were produced at the Space Telescope Science Institute under U.S. Government grant NAG W-2166. The images of these surveys are based on photographic data obtained using the Oschin Schmidt Telescope on Palomar Mountain and the UK Schmidt Telescope. The plates were processed into the present compressed digital form with the permission of these institutions. The National Geographic Society - Palomar Observatory Sky Atlas (POSS-I) was made by the California Institute of Technology with grants from the National Geographic Society. The Second Palomar Observatory Sky Survey (POSS-II) was made by the California Institute of Technology with funds from the National Science Foundation, the National Geographic Society, the Sloan Foundation, the Samuel Oschin Foundation, and the Eastman Kodak Corporation. The Oschin Schmidt Telescope is operated by the California Institute of Technology and Palomar Observatory.The UK Schmidt Telescope was operated by the Royal Observatory Edinburgh, with funding from the UK Science and Engineering Research Council (later the UK Particle Physics and Astronomy Research Council), until 1988 June, and thereafter by the Anglo-Australian Observatory. The blue plates of the southern Sky Atlas and its Equatorial Extension (together known as the SERC-J), as well as the Equatorial Red (ER), and the Second Epoch [red] Survey (SES) were all taken with the UK Schmidt.

2.7 Appendix A - Comparison of the Three CO Datasets

We present plots of selected properties from the three observing programs that make up our sample in Figure 2.8. There is a large difference in the distribution of distances between the three datasets, as the NGLS and Virgo follow-up have an obvious peak at our assumed Virgo distance of 16.7 Mpc. For the atomic hydrogen mass, there is only a significant difference between the distributions of the Virgo follow-up and the HRS ($p = 0.003$) datasets using the Kolmogorov-Smirnov test, likely due to the Virgo follow-up program only containing Virgo galaxies. For the sSFR, we only find a small difference between the distributions for the NGLS and the HRS datasets ($p = 0.036$). For the stellar mass distributions, we find no significant differences using the Kolmogorov-Smirnov test. Finally, for the molecular gas mass, we use the log-rank test to find the only significant difference is between the NGLS and the HRS datasets ($p = 0.003$), where the resulting mean molecular gas mass is lower in the HRS dataset.

Any differences between the samples can be attributed to the small numbers of galaxies in each dataset and to the percentage of galaxies in each environment, since our sample criteria is very similar between the three datasets. For example, the original NGLS dataset contain roughly equal numbers of group and Virgo galaxies, with a smaller number of field galaxies. The Virgo follow-up only contains Virgo galaxies. The HRS, which contains galaxies not already in the sample from the NGLS and Virgo follow-up, is skewed towards group galaxies. Given that the three datasets trace the environment differently, that is likely one of the main causes of the observed variations.

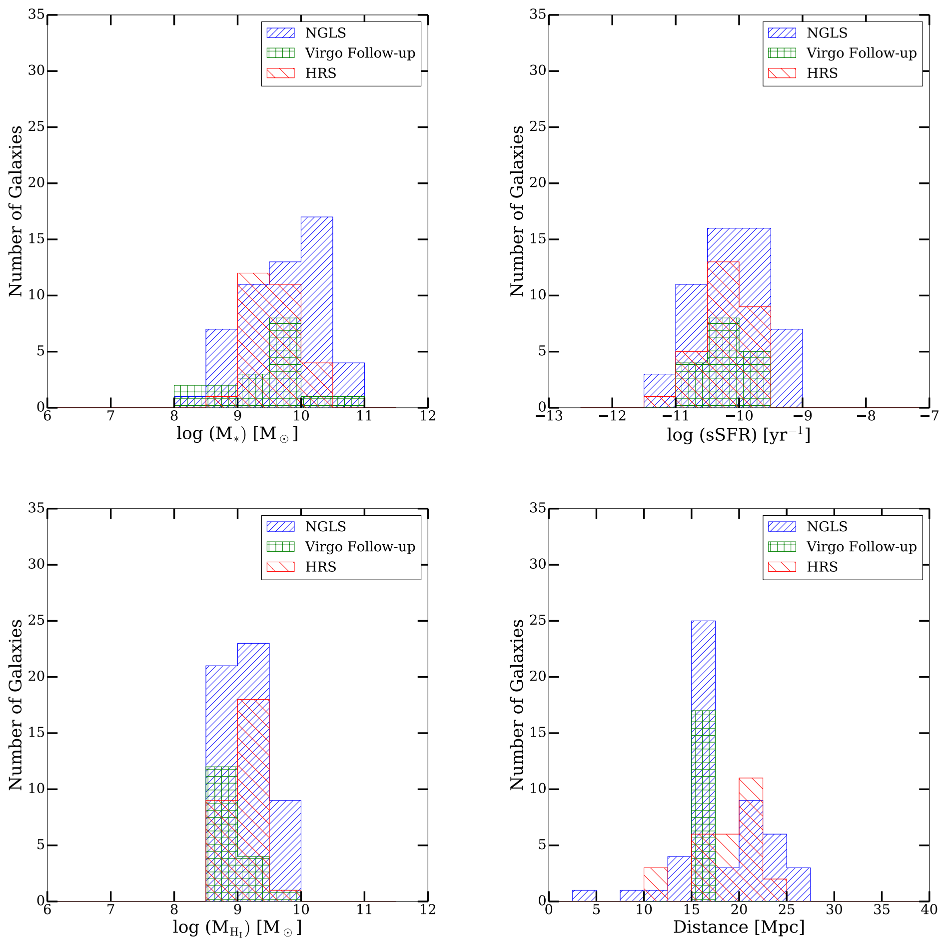

Figure 2.8 We present histograms of selected properties of the three sample sources, the NGLS, Virgo follow-up sample, and the additional HRS galaxies. The properties presented are stellar mass (top left), sSFR (top right), H I mass (bottom left), and distance (bottom right).

Table 2.7 Selected Properties of Field Galaxies

Name	Type[1]	D_{25}[1] (kpc)	Distance[2] (Mpc)	ΔT[3] (mK)	$L_{CO(3-2)}$[4] (10^7 K km s^{-1} pc^2)	$\log(M_{HI})$[5] ($M_\odot$)	$\log(M_{H_2})$[6] ($M_\odot$)	$\log(M_*)$[7] ($M_\odot$)	SFR[8] ($M_\odot$ yr^{-1})
ESO477-016	Sbc	16.5	24.2	16	< 1.48	9.06	< 8.72	9.10	0.18
ESO570-019	Sc	7.4	18.4	21	< 1.12	9.13	< 8.60	8.85	0.14
IC1254	SABb	5.8	21.9	21	< 1.57	8.90	< 8.75	$9.05^\dagger$	0.12
NGC0210	SABb	32.7	22.4	25	1.46 ± 0.47	9.79	8.42	$10.38^\dagger$	2.53
NGC6118	Sc	31.4	24.2	26	< 2.38	9.54	< 8.93	10.41	2.44
NGC6140	Sc	10.8	17.8	20	< 0.99	9.67	< 8.55	9.66	2.11
NGC7742	Sb	12.3	24.8	20	4.58 ± 0.84	9.09	8.91	10.28	0.46
PGC045195	Sd	21.9	20.7	16	< 1.09	9.48	< 8.59	9.32	1.60
PGC057723	SABb	7.9	14.9	20	< 0.69	9.31	< 8.39	$9.42^\dagger$	1.04
UGC06378	Sc	13.0	23.0	19	< 1.55	9.12	< 8.74	8.82	0.18
UGC06792	Sc	10.1	15.5	23	< 0.84	8.79	< 8.48	8.63	0.16
NGC4013	Sb	22.1	15.5	19	8.08 ± 1.04	9.15	9.16	10.32	0.46
NGC3437**	SABc	13.7	20.1	23	1.23 ± 0.23	9.11	8.34	10.04	0.70
NGC3485**	Sb	13.9	21.9	22	< 0.20	9.46	< 7.84	9.82	0.36
NGC3501**	Sc	22.1	17.8	25	0.53 ± 0.15	8.99	7.97	9.76	0.05
NGC3526**	Sc	14.9	21.3	16	< 0.14	8.95	< 7.70	9.31	0.12
NGC3666**	SBc	16.8	16.7	17	0.70 ± 0.16	9.36	8.09	9.75	0.29

Note: ** next to name indicates that the galaxy is from the HRS program

[1] Morphologies and D_{25} extracted from HyperLeda database

[2] Distances extracted from HyperLeda, corrected for Virgo infall and assuming $H_o = 70$ km s^{-1} Mpc^{-1}, $\Omega_M = 0.27$, $\Omega_\Lambda = 0.73$

[3] RMS noise in individual spectra in the data cube at 20 km s^{-1} resolution on T_{MB} scale

[4] Upper limits are 2σ limits calculated over an area of $1'$ and a line width of 100 km s^{-1}

[5] M_{HI} calculated using values for H I flux from HyperLeda database

[6] M_{H_2} calculated assuming a CO $J = 3-2/J = 1-0$ line ratio of 0.18

[7] $\log(M_*)$ from the S^{4}G survey (Sheth et al., 2010), except for galaxies with † symbol, where $\log(M_*)$ is from K-band luminosity assuming stellar mass-to-light ratio of 0.533 (Portinari et al., 2004)

[8] Star formation rates from Sánchez-Gallego et al. (2012) for NGLS galaxies, Boselli et al. (2015) for HRS galaxies

2.8 Appendix B - Selected Properties of the Galaxies in our Sample

Table 2.8 Selected Properties of Group Galaxies

Name	Type[1]	D_{25}[1] (kpc)	Distance[2] (Mpc)	ΔT[3] (mK)	$L_{CO(3-2)}$[4] (10^7 K km s^{-1} pc^2)	$\log(M_{HI})$[5] ($M_\odot$)	$\log(M_{H_2})$[6] ($M_\odot$)	$\log(M_*)$[7] ($M_\odot$)	SFR[8] ($M_\odot$ yr^{-1})	Group ID [9]
IC0750	Sab	8.3	13.7	25	13.41 ± 0.97	8.92	9.38	9.99	0.26	269
IC1066	Sb	8.5	24.2	19	< 1.71	9.02	< 8.79	9.53	0.40	387
NGC0450	SABc	21.8	25.4	20	0.85 ± 0.22	9.46	8.18	9.75	1.13	P
NGC0615	Sb	23.8	25.9	15	< 1.60	9.42	< 8.75	10.34	0.90	27
NGC1140	SBm	11.9	20.1	15	< 0.95	9.39	< 8.53	9.45	1.19	71
NGC1325	SBbc	26.3	20.7	21	< 1.40	9.29	< 8.70	10.05	0.63	97
NGC2146A	SABc	20.3	25.9	24	< 2.49	9.56	< 8.95	$9.69^\dagger$	0.21	P
NGC2742	Sc	18.8	22.4	24	2.53 ± 0.83	9.27	8.65	10.21	1.06	167
NGC3077	S?	6.0	3.9	26	0.28 ± 0.05	9.12	7.69	9.28	0.03	176
NGC3162	SABc	12.6	20.7	22	2.80 ± 0.66	9.41	8.70	9.91	2.36	194
NGC3227	SABa	21.3	18.4	25	11.74 ± 1.29	8.99	9.32	10.41	0.21	194
NGC3254	Sbc	14.9	21.9	19	< 1.42	9.56	< 8.70	10.09	1.25	197
NGC3353	Sb	6.7	17.2	26	< 1.21	8.88	< 8.64	9.18	0.62	201
NGC3507	SBb	13.3	15.5	21	1.30 ± 0.42	8.95	8.36	9.96	0.92	228
NGC3782	Scd	5.1	14.3	21	< 0.52	9.01	< 8.27	9.00	0.18	258
NGC4041	Sbc	16.4	21.9	22	30.09 ± 2.52	9.56	9.73	10.32	3.99	266
NGC4288	SBcd	5.7	11.5	21	< 0.34	8.92	< 8.09	8.92	0.05	269
NGC4504	SABc	13.7	14.9	18	< 0.61	9.51	< 8.34	9.67	0.45	293
NGC4772	Sa	19.1	16.1	17	< 0.54	8.82	< 8.28	10.04	0.08	292
NGC5477	Sm	2.7	8.6	22	< 0.25	8.80	< 7.95	8.14	0.03	371
NGC5486	Sm	9.5	24.2	16	< 1.49	9.18	< 8.72	9.15	0.31	373
IC3908**	SBcd	13.6	19.0	13	2.56 ± 0.25	8.96	8.66	9.92	0.21	314
NGC3346**	SBc	14.9	19.5	19	0.41 ± 0.13	9.09	7.87	9.88	0.28	214
NGC3370**	Sc	14.4	20.1	26	< 0.27	9.26	< 7.98	9.86	0.52	219
UGC06023**	SBcd	10.3	21.3	24	< 0.25	8.98	< 7.94	9.46	0.28	227
NGC3455**	SABb	11.5	17.2	22	< 0.13	8.96	< 7.67	9.28	0.22	219
NGC3681**	Sbc	9.9	19.5	20	< 0.16	9.37	< 7.75	9.93	0.17	237
NGC3684**	Sbc	12.3	18.4	22	0.68 ± 0.20	9.37	8.08	9.80	0.38	237
NGC3756**	SABb	12.4	22.4	26	< 0.29	9.36	< 8.02	10.17	0.34	250
NGC3795**	Sbc	12.9	21.3	26	< 0.26	8.89	< 7.97	9.38	0.09	244
NGC3982**	SABb	12.5	20.1	26	4.76 ± 0.81	9.22	8.93	10.03	0.94	250
NGC4123**	Sc	18.5	20.1	28	0.49 ± 0.16	9.56	7.94	10.06	0.63	275
NGC4668**	SBcd	11.2	24.2	24	< 0.28	9.11	< 8.00	9.42	0.33	299
NGC4688**	Sc	16.8	15.5	29	< 0.11	9.15	< 7.61	9.43	0.28	292
NGC4701**	Sc	5.8	11.5	26	< 0.07	9.02	< 7.41	9.19	0.19	292
NGC4713**	Scd	5.3	10.9	12	0.22 ± 0.06	9.03	7.60	9.33	0.35	315
NGC4771**	Sc	15.5	17.2	13	0.23 ± 0.07	8.94	7.61	9.82	0.17	315
NGC4775**	Scd	15.0	23.0	12	1.33 ± 0.42	9.46	8.37	9.92	1.26	314
NGC4808**	Sc	8.2	12.0	25	0.76 ± 0.17	9.28	8.13	9.53	0.37	315
UGC06575**	Sc	11.0	21.3	27	< 0.26	9.15	< 7.96	8.98	0.13	244
UGC07982**	Sc	14.9	17.8	13	< 0.10	8.69	< 7.57	9.41	0.07	315
UGC08041**	SBcd	18.5	20.1	12	< 0.12	9.19	< 7.62	9.46	0.16	315

Note: ** next to name indicates that the galaxy is from the HRS program

[1] Morphologies and D_{25} extracted from HyperLeda database

[2] Distances extracted from HyperLeda, corrected for Virgo infall and assuming $H_o = 70$ km s^{-1} Mpc^{-1}, $\Omega_M = 0.27$, $\Omega_\Lambda = 0.73$

[3] RMS noise in individual spectra in the data cube at 20 km s^{-1} resolution on T_{MB} scale

[4] Upper limits are 2σ limits calculated over an area of $1'$ and a line width of 100 km s^{-1}

[5] M_{HI} calculated using values for H I flux from HyperLeda database

[6] M_{H_2} calculated assuming a CO $J = 3-2/J = 1-0$ line ratio of 0.18

[7] $\log(M_*)$ from the S^{4}G survey (Sheth et al., 2010), except for galaxies with † symbol, where $\log(M_*)$ is from K-band luminosity assuming stellar mass-to-light ratio of 0.533 (Portinari et al., 2004)

[8] Star formation rates from Sánchez-Gallego et al. (2012) for NGLS galaxies, Boselli et al. (2015) for HRS galaxies

[9] Group IDs from Garcia (1993), while P indicates pairs from Karachentsev (1972)

Table 2.9 Selected Properties of Virgo Galaxies

Name	Type[1]	D_{25}[1] (kpc)	Distance[2] (Mpc)	ΔT[3] (mK)	$L_{CO(3-2)}$[4] (10^7 K km s^{-1} pc^2)	$\log(M_{HI})$[5] ($M_\odot$)	$\log(M_{H_2})$[6] ($M_\odot$)	$\log(M_*)$[7] ($M_\odot$)	SFR[8] ($M_\odot$ yr^{-1})
IC3061*	SBc	22.9	16.7	22	< 0.83	8.70	< 8.47	9.12	0.05
IC3074*	SBd	2.9	16.7	19	< 0.84	8.89	< 8.48	$8.61^\dagger$	0.03
IC3322A*	SBc	8.8	16.7	21	0.26 ± 0.07	9.09	7.67	9.55	0.13
IC3371*	Sc	5.1	16.7	21	< 0.81	8.68	< 8.46	8.29	0.02
IC3576*	SBm	11.1	16.7	21	< 0.89	8.95	< 8.50	8.77	0.06
NGC4206	Sbc	16.3	16.7	14	0.48 ± 0.14	9.38	7.93	9.63	0.20
NGC4254	Sc	52.9	16.7	27	73.80 ± 2.51	9.66	10.12	10.66	11.31
NGC4273*	Sc	22.4	16.7	23	5.88 ± 0.69	8.95	9.02	9.85	0.76
NGC4298	Sc	13.4	16.7	21	6.56 ± 1.16	8.84	9.07	10.08	0.27
NGC4303A	Sbc	47.5	16.7	26	52.64 ± 5.72	9.65	9.97	10.71	3.29
NGC4302*	Sc	32.3	16.7	14	6.37 ± 0.91	9.28	9.05	10.29	0.32
NGC4303*	Sbc	47.5	16.7	26	52.64 ± 5.72	9.65	9.97	10.71	3.29
NGC4316*	Sc	13.9	16.7	22	0.56 ± 0.16	8.70	8.00	9.71	0.08
NGC4330*	Sc	16.9	16.7	24	0.41 ± 0.14	8.68	7.87	9.59	0.05
NGC4383	Sa	12.8	16.7	20	1.13 ± 0.22	9.16	8.30	9.65	0.39
NGC4390	SABc	7.6	16.7	19	< 0.88	8.63	< 8.50	9.26	0.09
NGC4411A*	Sc	9.5	16.7	23	< 0.80	8.65	< 8.46	9.08	0.05
NGC4411B*	SABc	10.8	16.7	22	< 0.99	8.91	< 8.55	9.30	0.09
NGC4423	Sd	10.2	16.7	18	0.16 ± 0.05	8.91	7.44	8.97	0.06
NGC4430	Sb	13.3	16.7	17	1.22 ± 0.40	8.62	8.34	9.63	0.12
NGC4470	Sa	13.2	16.7	19	< 0.84	8.68	< 8.47	9.43	0.03
NGC4480*	SABc	20.1	16.7	20	0.77 ± 0.24	8.87	8.14	9.51	0.20
NGC4498*	Sc	19.8	16.7	24	< 0.78	8.77	< 8.14	9.52	0.24
NGC4519*	Scd	13.0	16.7	22	< 1.12	9.49	< 8.30	9.57	0.39
NGC4522	SBc	35.5	16.7	13	1.39 ± 0.21	8.72	8.39	9.64	0.06
NGC4548	Sb	14.7	16.7	35	< 0.33	8.86	< 8.07	10.57	0.32
NGC4561	SBcd	8.6	16.7	26	< 1.17	9.11	< 8.62	9.18	0.49
NGC4567	Sbc	27.2	16.7	20	7.58 ± 0.99	9.02	9.13	10.03	0.14
NGC4568	Sbc	42.2	16.7	19	26.30 ± 1.98	8.88	9.67	10.38	0.29
NGC4579	SABb	34.4	16.7	20	7.89 ± 2.51	8.79	9.15	10.80	3.62
NGC4639	Sbc	13.5	16.7	20	< 0.28	8.97	< 7.70	9.91	0.19
NGC4647	SABc	17.5	16.7	23	12.11 ± 1.86	8.70	9.33	$10.20^\dagger$	2.84
NGC4651	Sc	15.5	16.7	19	4.10 ± 0.79	9.47	8.86	10.28	1.15
NGC4654	Sc	22.7	16.7	12	16.22 ± 1.61	9.49	9.46	10.35	1.08
PGC040604*	SBm	5.3	16.7	24	< 1.05	8.64	< 8.57	$8.06^\dagger$	0.02
UGC07557*	SABm	11.9	16.7	24	< 1.02	9.03	< 8.56	9.76	0.07
UGC07590	Sbc	6.1	16.7	19	< 0.89	8.87	< 8.50	8.73	0.02
NGC4294**	SBc	11.7	16.7	24	< 0.15	9.20	< 7.71	9.49	0.38
NGC4396**	Scd	13.6	16.7	25	< 0.14	8.87	< 7.68	$9.35^\dagger$	0.15

Note: * indicates galaxy is in the Virgo follow-up program, ** indicates that the galaxy is from the HRS program

[1] Morphologies and D_{25} extracted from HyperLeda database

[2] Distances set to be at 16.7 Mpc (Mei et al., 2007)

[3] RMS noise in individual spectra in the data cube at 20 km s^{-1} resolution on T_{MB} scale

[4] Upper limits are 2σ limits calculated over an area of $1'$ and a line width of 100 km s^{-1}

[5] M_{HI} calculated using values for H I flux from HyperLeda database

[6] M_{H_2} calculated assuming a CO $J = 3-2/J = 1-0$ line ratio of 0.18

[7] $\log(M_*)$ from the S^{4}G survey (Sheth et al., 2010), except for galaxies with † symbol, where $\log(M_*)$ is from K-band luminosity assuming stellar mass-to-light ratio of 0.533 (Portinari et al., 2004)

[8] Star formation rates from Sánchez-Gallego et al. (2012) for NGLS galaxies, GOLDMine database for the Virgo follow-up (Gavazzi et al., 2003), and Boselli et al. (2015) for HRS galaxies

2.9 Appendix C - CO $J = 3 - 2$ Maps of NGLS Galaxies

We present the CO $J = 3 - 2$ maps of our sample of galaxies from the Nearby Galaxies Legacy Survey.

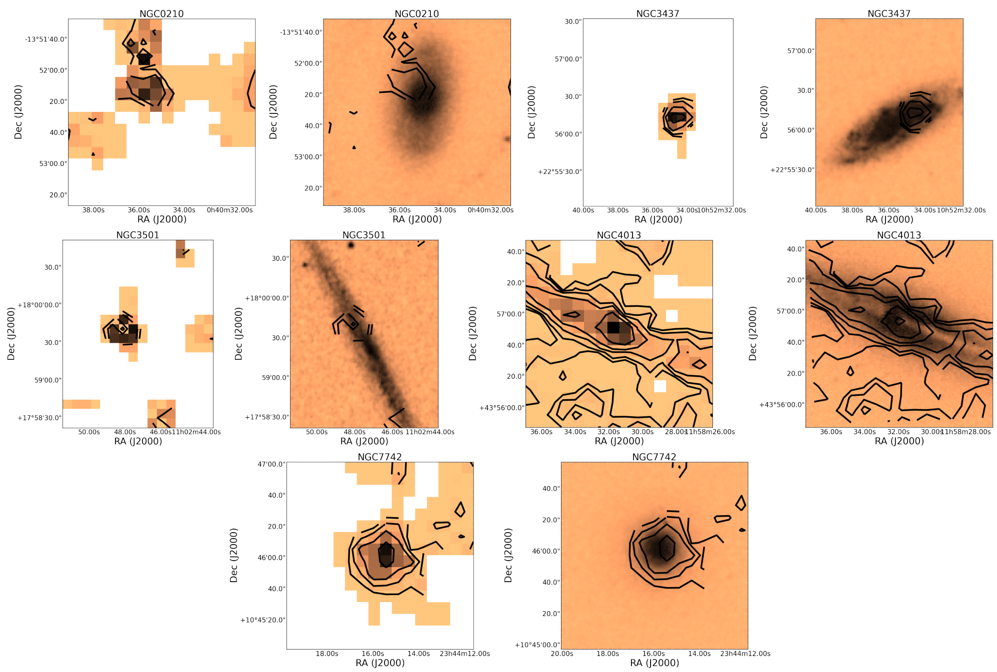

Figure 2.9 Images of the CO detected galaxies in the field sample. There are two plots for each galaxy. The first panel in each pair is the CO $J = 3-2$ integrated galaxy map with black contour levels overlaid at 0.5, 1, and 2 K km s^{-1}. The second panel is the same contour levels overlaid on the optical image from the Digitized Sky Survey.

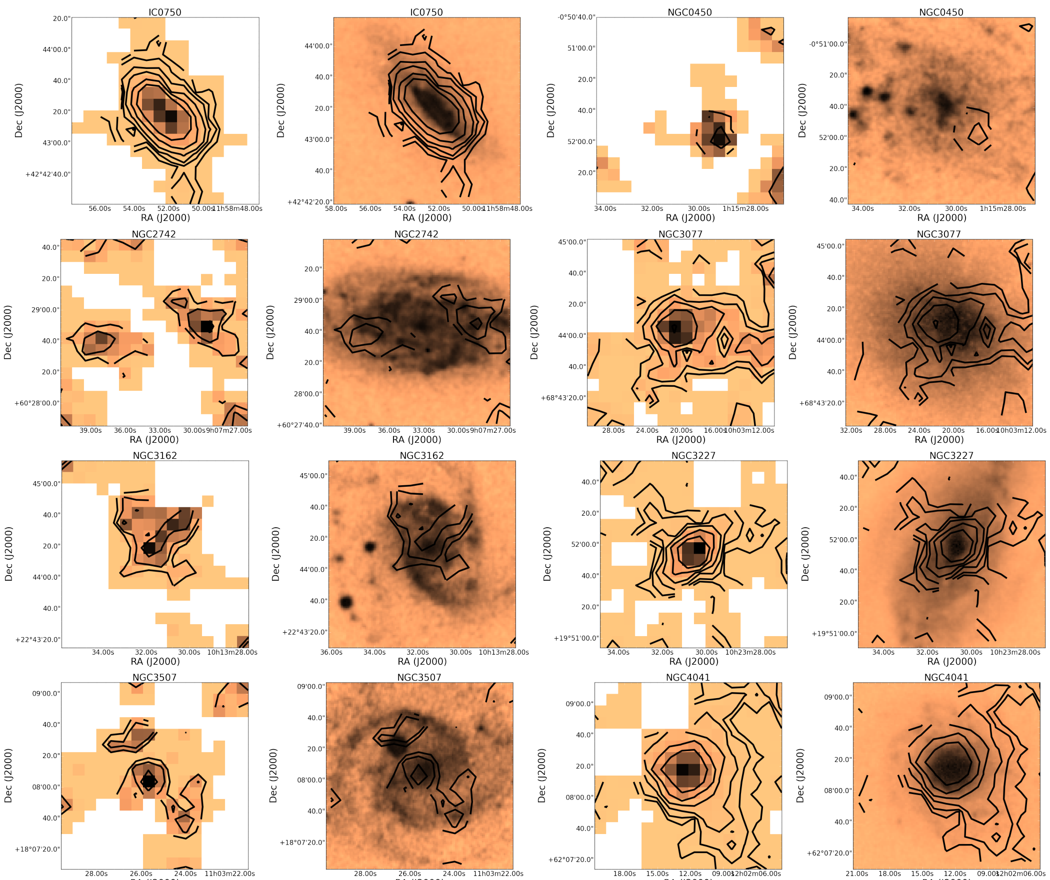

Figure 2.10 Images of the CO detected galaxies in the group sample. The first panel in each pair is the CO $J = 3-2$ integrated galaxy map with black contour levels overlaid at 0.5, 1, 2, 4, 8, and 16 K km s^{-1}. The second panel is the same contour levels overlaid on the optical image from the Digitized Sky Survey.

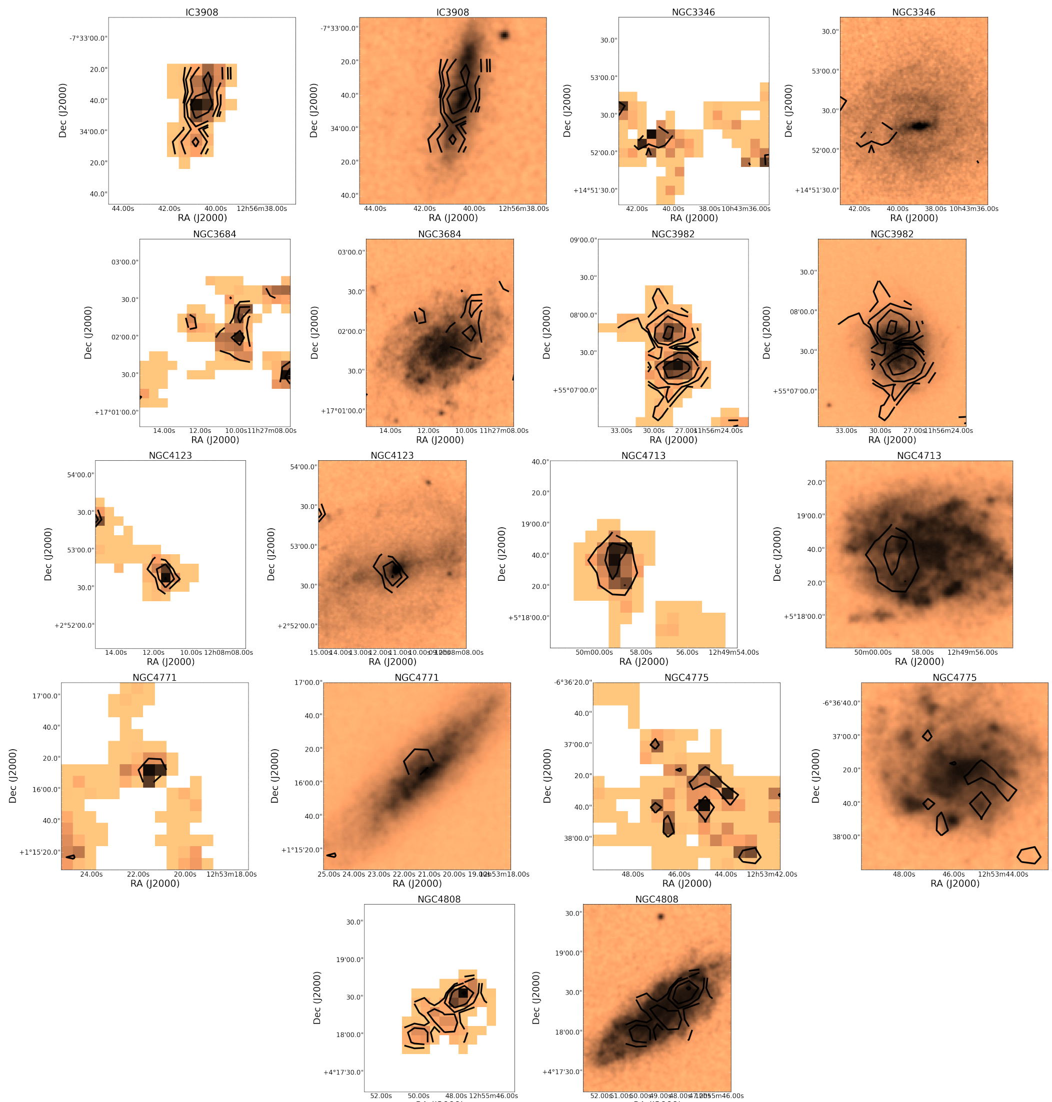

Figure 2.11 Additional images of the CO detected galaxies in the group sample. The first panel in each pair is the CO $J = 3-2$ integrated galaxy map with black contour levels overlaid at 0.5, 1, 2, 4, 8, and 16 K km s^{-1}. The second panel is the same contour levels overlaid on the optical image from the Digitized Sky Survey.

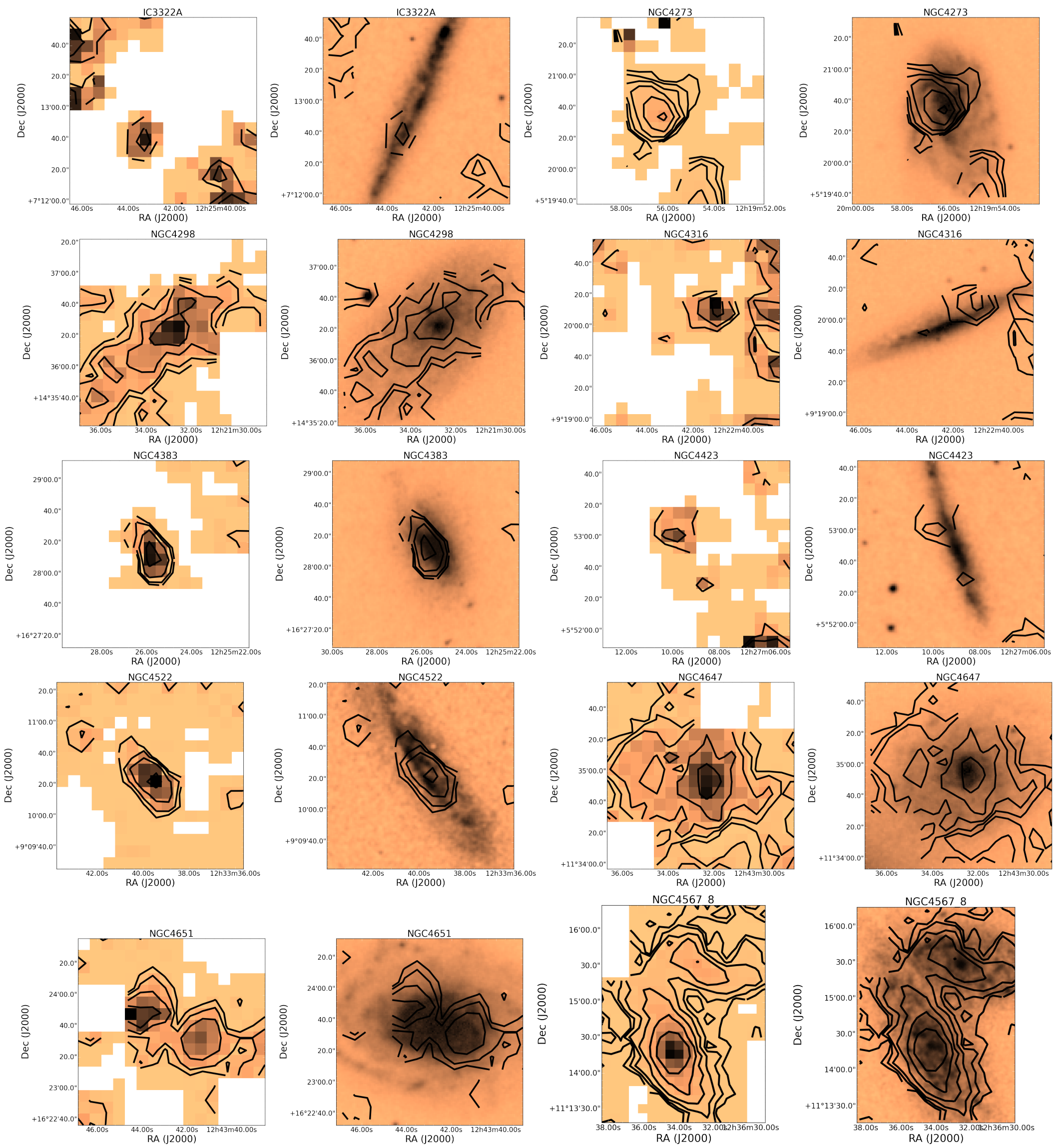

Figure 2.12 Images of the CO detected galaxies in the Virgo sample. The first panel in each pair is the CO $J = 3 - 2$ integrated galaxy map with black contour levels overlaid at 0.5, 1, 2, 4, 8, and 16 K km s^{-1}. The second panel is the same contour levels overlaid on the optical image from the Digitized Sky Survey. Note that NGC 4567 and 4568 were combined into one image due to their close proximity.

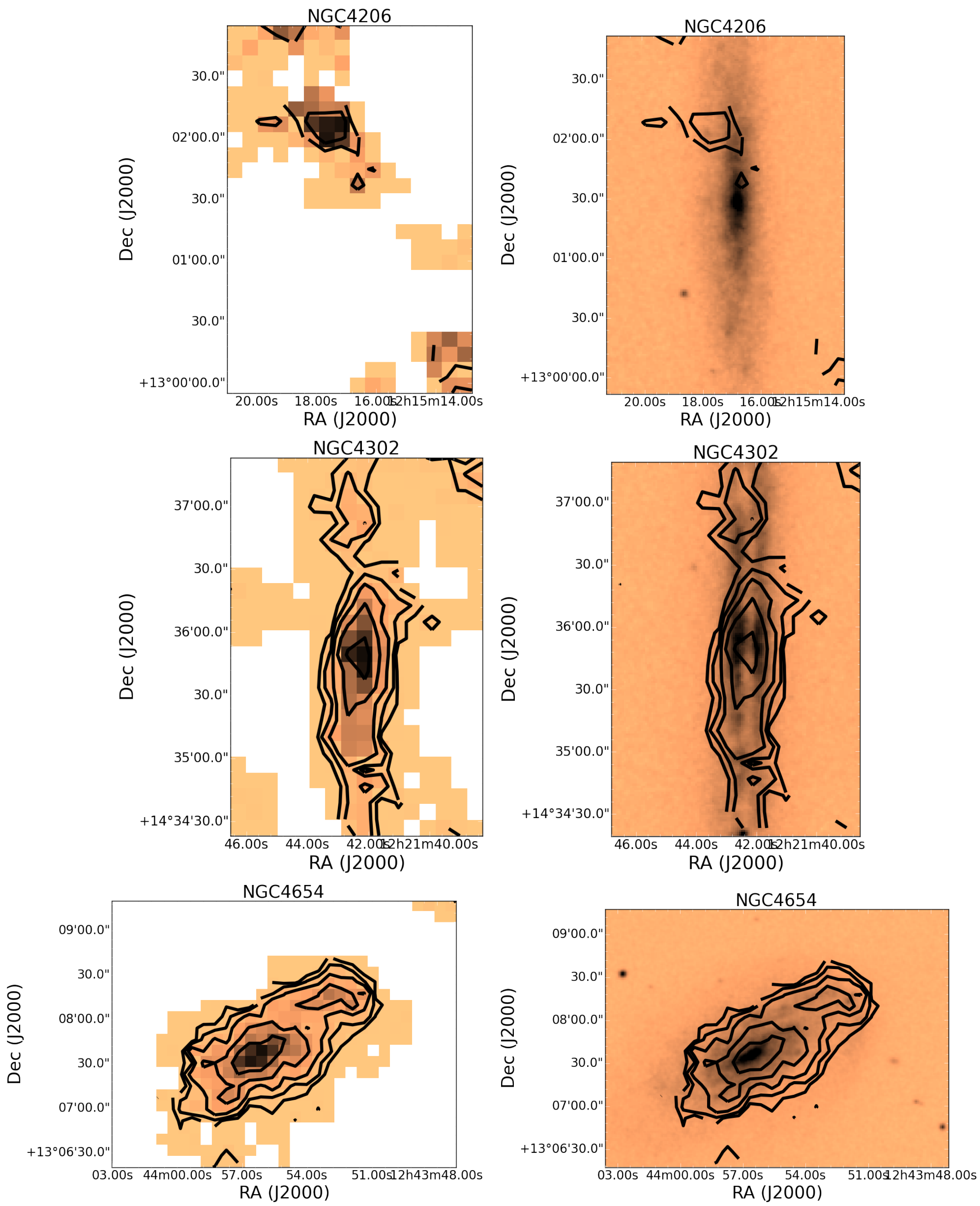

Figure 2.13 Images of the CO detected galaxies in the Virgo sample, observed with two overlapping fields. The first panel in each pair is the CO $J = 3-2$ integrated galaxy map with black contour levels overlaid at 0.5, 1, 2, 4, and 16 K km s^{-1}. The second panel is the same contour levels overlaid on the optical image from the Digitized Sky Survey.

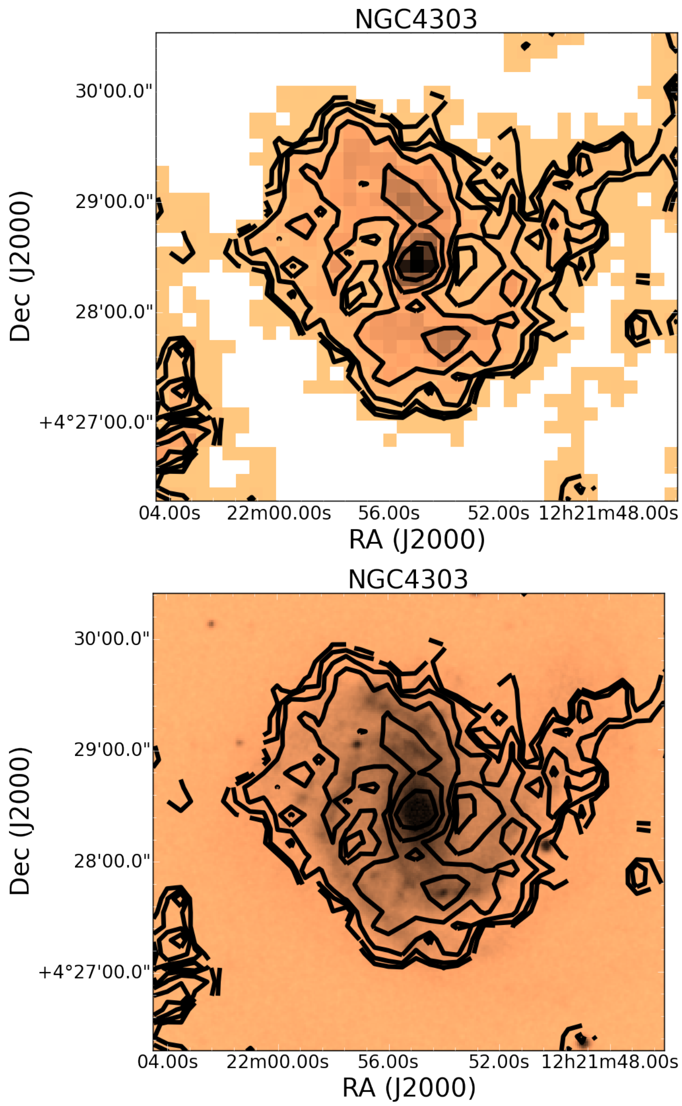

Figure 2.14 Images of NGC 4303 in the Virgo sample, observed using the raster method. The first panel in each pair is the CO $J = 3 - 2$ integrated galaxy map with black contour levels overlaid at 0.5, 1, 2, 4, 8, and 16 K km s^{-1}. The second panel is the same contour levels overlaid on the optical image from the Digitized Sky Survey.

Bibliography

Alatalo K., et al., 2015, MNRAS, 450, 3874

Arimoto N., Sofue Y., Tsujimoto T., 1996, PASJ, 48, 275

Baldry I. K., Balogh M. L., Bower R. G., Glazebrook K., Nichol R. C., Bamford S. P., Budavari T., 2006, MNRAS, 373, 469

Bell E. F., McIntosh D. H., Katz N., Weinberg M. D., 2003, ApJS, 149, 289

Bendo G. J., et al., 2007, MNRAS, 380, 1313

Bigiel F., Leroy A., Walter F., Brinks E., de Blok W. J. G., Madore B., Thornley M. D., 2008, AJ, 136, 2846

Bigiel F., et al., 2011, ApJ, 730, L13

Binggeli B., Sandage A., Tammann G. A., 1985, AJ, 90, 1681

Blanton M. R., Moustakas J., 2009, ARA&A, 47, 159

Bolatto A. D., Leroy A. K., Rosolowsky E., Walter F., Blitz L., 2008, ApJ, 686, 948

Bolatto A. D., Wolfire M., Leroy A. K., 2013, ARA&A, 51, 207

Boselli A., et al., 2010, PASP, 122, 261

Boselli A., Cortese L., Boquien M., Boissier S., Catinella B., Lagos C., Saintonge A., 2014, A&A, 564, A66

Boselli A., Fossati M., Gavazzi G., Ciesla L., Buat V., Boissier S., Hughes T. M., 2015, A&A, 579, A102

Buckle J. V., et al., 2009, MNRAS, 399, 1026

Buckley J., James I., 1979, Biometrika, 66, 429

Chamaraux P., Balkowski C., Gerard E., 1980, A&A, 83, 38

Corbelli E., et al., 2012, A&A, 542, A32

Elbaz D., et al., 2007, A&A, 468, 33

Ellison S. L., Patton D. R., Simard L., McConnachie A. W., 2008, AJ, 135, 1877

Ellison S. L., Patton D. R., Simard L., McConnachie A. W., Baldry I. K., Mendel J. T., 2010, MNRAS, 407, 1514

Ellison S. L., Mendel J. T., Patton D. R., Scudder J. M., 2013, MNRAS, 435, 3627

Eskew M., Zaritsky D., Meidt S., 2012, AJ, 143, 139

Fumagalli M., Gavazzi G., 2008, A&A, 490, 571

Garcia A. M., 1993, A&AS, 100, 47

Gavazzi G., Boselli A., Donati A., Franzetti P., Scodeggio M., 2003, A&A, 400, 451

Gavazzi G., Boselli A., van Driel W., O'Neil K., 2005, A&A, 429, 439

Geha M., Blanton M. R., Yan R., Tinker J. L., 2012, ApJ, 757, 85

Genzel R., et al., 2015, ApJ, 800, 20

Gunn J. E., Gott III J. R., 1972, ApJ, 176, 1

Hafok H., Stutzki J., 2003, A&A, 398, 959

Haynes M. P., Giovanelli R., 1986, ApJ, 306, 466

Huang M.-L., Kauffmann G., 2014, MNRAS, 443, 1329

Huang S., et al., 2014, ApJ, 793, 40

Iono D., et al., 2009, ApJ, 695, 1537

Israel F. P., 1997, A&A, 328, 471

Israel F., 2000, in Combes F., Pineau Des Forets G., eds, Molecular Hydrogen in Space. p. 293 (`arXiv:astro-ph/0001250`)

Kannappan S. J., et al., 2013, ApJ, 777, 42

Kaplan E. L., Meier P., 1958, J. Amer. Statist. Assn., 53, 457

Karachentsev I. D., 1972, Soobshcheniya Spetsial'noj Astrofizicheskoj Observatorii, 7, 1

Karachentseva V. E., 1973, Soobshcheniya Spetsial'noj Astrofizicheskoj Observatorii, 8, 3

Keel W. C., Kennicutt Jr. R. C., Hummel E., van der Hulst J. M., 1985, AJ, 90, 708

Kenney J. D. P., Young J. S., 1989, ApJ, 344, 171

Kennicutt Jr. R. C., 1989, ApJ, 344, 685

Kennicutt Jr. R. C., 1998a, ARA&A, 36, 189

Kennicutt Jr. R. C., 1998b, ApJ, 498, 541

Kennicutt R. C., Evans N. J., 2012, ARA&A, 50, 531

Kennicutt Jr. R. C., et al., 2007, ApJ, 671, 333

Kennicutt Jr. R. C., et al., 2009, ApJ, 703, 1672

Knapen J. H., James P. A., 2009, ApJ, 698, 1437

Knapen J. H., Cisternas M., Querejeta M., 2015, MNRAS, 454, 1742

Knapp G. R., Helou G., Stark A. A., 1987, AJ, 94, 54

Koopmann R. A., Haynes M. P., Catinella B., 2006, AJ, 131, 716

Kroupa P., Weidner C., 2003, ApJ, 598, 1076

Krumholz M. R., McKee C. F., Tumlinson J., 2009, ApJ, 699, 850

Kuno N., et al., 2007, PASJ, 59, 117

Larson R. B., Tinsley B. M., Caldwell C. N., 1980, ApJ, 237, 692

Leroy A. K., Walter F., Brinks E., Bigiel F., de Blok W. J. G., Madore B., Thornley M. D., 2008, AJ, 136, 2782

Leroy A. K., et al., 2012, AJ, 144, 3

Leroy A. K., et al., 2013, AJ, 146, 19

Lisenfeld U., et al., 2011, A&A, 534, A102

Makarov D., Prugniel P., Terekhova N., Courtois H., Vauglin I., 2014, A&A, 570, A13

Mantel N., 1966, Cancer Chemother Rep., 50, 163

Mei S., et al., 2007, ApJ, 655, 144

Mihos J. C., Hernquist L., 1996, ApJ, 464, 641

Moore B., Katz N., Lake G., Dressler A., Oemler A., 1996, Nature, 379, 613

Pappalardo C., et al., 2012, A&A, 545, A75

Paturel G., Petit C., Prugniel P., Theureau G., Rousseau J., Brouty M., Dubois P., Cambrésy L., 2003, A&A, 412, 45

Portinari L., Sommer-Larsen J., Tantalo R., 2004, MNRAS, 347, 691

Saintonge A., et al., 2011, MNRAS, 415, 61

Sánchez-Gallego J. R., Knapen J. H., Wilson C. D., Barmby P., Azimlu M., Courteau S., 2012, MNRAS, 422, 3208

Sheth K., et al., 2010, PASP, 122, 1397

Skrutskie M. F., et al., 2006, AJ, 131, 1163

Solanes J. M., Manrique A., García-Gómez C., González-Casado G., Giovanelli R., Haynes M. P., 2001, ApJ, 548, 97

Stark A. A., Knapp G. R., Bally J., Wilson R. W., Penzias A. A., Rowe H. E., 1986, ApJ, 310, 660

Strateva I., et al., 2001, AJ, 122, 1861

Strong A. W., et al., 1988, A&A, 207, 1

Teyssier R., Chapon D., Bournaud F., 2010, ApJ, 720, L149

Toomre A., 1964, ApJ, 139, 1217

Tremonti C. A., et al., 2004, ApJ, 613, 898

Usero A., et al., 2015, AJ, 150, 115

Vollmer B., Wong O. I., Braine J., Chung A., Kenney J. D. P., 2012, A&A, 543, A33

Wang J., et al., 2013, MNRAS, 433, 270

Wilson C. D., 1995, ApJ, 448, L97

Wilson C. D., et al., 2009, ApJ, 693, 1736

Wilson C. D., et al., 2012, MNRAS, 424, 3050

Young L. M., et al., 2011, MNRAS, 414, 940

Chapter 3

The JCMT Nearby Galaxies Legacy Survey – XI. – Environmental Variations in the Atomic and Molecular Gas Radial Profiles of Nearby Spiral Galaxies

Angus Mok [1], C. D. Wilson[1], J. H. Knapen[2,3], J. R. Sánchez-Gallego[4], E. Brinks[5], and E. Rosolowsky[6]

[1] Department of Physics & Astronomy, McMaster University, Hamilton, Ontario L8S 4M1, Canada

[2] Instituto de Astrofísica de Canarias, E-38205 La Laguna, Tenerife, Spain

[3] Departamento de Astrofísica, Universidad de La Laguna, E-38200 La Laguna, Tenerife, Spain

[4] Department of Physics and Astronomy, University of Kentucky, 40506-0055, Lexington, Kentucky, United States

[5] Centre for Astrophysics Research, University of Hertfordshire, AL10 9AB, Hatfield, Hertfordshire, United Kingdom

[6] Department of Physics, University of Alberta, Edmonton, Ontario T6G 2R3, Canada

Abstract

We present an analysis of the radial profiles of a sample of 43 H I-flux selected spiral galaxies from the Nearby Galaxies Legacy Survey (NGLS) with resolved James Clerk Maxwell Telescope (JCMT) CO $J = 3-2$ and/or Very Large Array (VLA) H I maps. Comparing the Virgo and non-Virgo populations, we confirm that the H I disks are truncated in the Virgo sample, even for these relatively H I-rich galaxies. On the other hand, the H_2 distribution is enhanced for Virgo galaxies near their centres, resulting in higher H_2 to H I ratios and steeper H_2 and total gas radial profiles. This is likely due to the effects of moderate ram pressure stripping in the cluster environment, which would preferentially remove low density gas in the outskirts while enhancing higher density gas near the centre. Combined with Hα star formation rate data, we find that the star formation efficiency (SFR/H_2) is relatively constant with radius for both samples, but Virgo galaxies have a $\sim 40\%$ lower star formation efficiency than non-Virgo galaxies.

3.1 Introduction

In the Universe, galaxies can be found in many different environments, from isolated galaxies, to groups of tens of galaxies, to clusters of thousands of galaxies. The star formation histories of these galaxies have been observed to vary greatly due to their environment. For example, overdense regions are increasingly dominated by quiescent galaxies (Dressler, 1980; Blanton & Moustakas, 2009). One of the major questions in the study of galaxy evolution is whether these effects are due to processes intrinsic to the galaxy, such as through the process of 'mass quenching', or if they can be attributed to the local environment (Peng et al., 2010, 2012). The lower density group environment is also important in this analysis, as galaxies can begin to be quenched in these groups before falling into clusters (McGee et al., 2009).

Optical studies of galaxies at a range of redshifts have provided valuable insight into these environmental effects, but a full analysis requires the study of the fuel for ongoing and future star formation. Spiral galaxies are important to this analysis because they are sites of active star formation, with gaseous disks that are sensitive to the effects of their surroundings. Past studies of the H I content of spiral galaxies in clusters have found that they are deficient in atomic gas (Haynes & Giovanelli, 1986) and their gas distributions are significantly truncated (Cayatte et al., 1990).

More recent studies have shown that star formation is most closely linked to the molecular gas content in these galaxies (Leroy et al., 2008; Saintonge et al., 2011; Bigiel et al., 2011). Given the observed reduction in overall star formation inside cluster spirals (Koopmann et al., 2006), the cluster environment should therefore have a strong effect on their molecular gas content. Processes such as ram pressure stripping (Gunn & Gott, 1972), tidal harassment (Moore et al., 1996), and strangulation (Larson et al., 1980) have been proposed to explain the environment's influence on the more diffuse H I component. However, any potential environmental effects on the denser, more centrally located H_2 gas is less clear.

Initial observations by Kenney & Young (1989) for 40 Virgo spirals using the Five College Radio Astronomy Observatory (FCRAO) found that they are not as H_2 deficient as they are H I deficient and suggested the survival of a large amount of molecular gas inside these galaxies. More recently, the Herschel Virgo Cluster Survey (HeViCS) created a sample of 12 galaxies with CO measurements and found that for disturbed galaxies, the H I gas is more efficiently stripped than the H_2 gas (Pappalardo et al., 2012). This results in steeper H_2 and total gas radial profiles for the more H I-deficient galaxies in their sample. The Herschel Reference Survey (HRS), which is a K-band selected sample of nearby galaxies, used the H I-deficiency parameter as a proxy for galaxy interactions and found a correlation between H I-deficiency and the level of H_2 gas deficiency and H_2 gas disk size (Boselli et al., 2014). They suggested that Virgo spiral galaxies may be more H_2 deficient than unperturbed field galaxies.

Here, we take a slightly different approach by using a gas-rich sample of spiral galaxies in three different environments (field, group, and the Virgo Cluster), which should be better proxies for any immediate environmental effects. To study the molecular gas properties of these galaxies, we use resolved maps from the Nearby Galaxies Legacy Survey (NGLS), an H I-flux limited sample of 155 nearby (D < 25 Mpc) galaxies (Wilson et al., 2012). In a previous paper, we select spiral galaxies from the NGLS sample to compare the field, group, and Virgo subsamples, focusing on their integrated properties (Mok et al., 2016). Compared to non-Virgo galaxies, galaxies in the Virgo cluster have higher H_2 gas masses and H_2 to H I ratios, perhaps due to environmental interactions that aid in the conversion of atomic to molecular gas. They also have lower specific star formation rates (sSFR = SFR/M_*) and lower star formation efficiencies (SFR/M_{H_2}), implying molecular gas depletion times ($t_{gas} = M_{H_2}$/SFR) that are longer than non-Virgo galaxies.

In this paper, we will further investigate the environmental effects by studying the radial profiles of the NGLS galaxies and measure any differences between the Virgo and non-Virgo sample. We select 43 galaxies from the larger sample of NGLS spiral galaxies for which we have detected maps of their H_2 and/or H I distributions, while excluding galaxies with inclinations of greater than 75 degrees. In § 2, we present our observations and some of the general properties of our sample. In § 3, we discuss the procedure used to create the radial profiles. We also present radial profiles for the H_2, H I, and star formation rate surface densities, as well as combinations of these properties, such as the molecular gas depletion time. Then, we discuss some implications of our data and provide comparisons to other observational and theoretical results.

3.2 Observations and Analysis

3.2.1 Data and Sample Selection

We seek to create a large sample of spiral galaxies with resolved molecular and/or atomic gas data available. To the original Nearby Galaxies Legacy Survey (NGLS) sample (Wilson et al., 2012), we add galaxies that match the NGLS survey criterion from two follow-up JCMT programs. The first is a program to complete the H I-flux selected sample of galaxies in the Virgo Cluster (M09AC05) and the second is to map the galaxies from the Herschel Reference Survey (M14AC05). From this larger sample, we select only spiral galaxies using the HyperLeda database, excluding any elliptical or lenticular galaxies. This results in the 98 spiral galaxies used in the analysis from Mok et al. (2016). For all of the galaxies in the survey, the CO $J = 3-2$ line was mapped out to at least $D_{25}/2$ using HARP on the James Clerk Maxwell Telescope (JCMT) (Wilson et al., 2012). The D_{25} value for each galaxy, which we take from the HyperLEDA survey, is defined as the length of the major axis of a galaxy at the B-band isophotal level of 25 mag/arcsec^2 (Paturel et al., 2003). In our analysis, we also use R_{25}, which is half of the D_{25} value for each galaxy.

To study the resolved properties of these galaxies, we select only galaxies for which we have detections in the CO $J = 3-2$ maps from the JCMT and/or the H I 21 cm line from the VLA. We exclude all galaxies with inclinations of greater than 75 degrees, as measured by the HyperLeda database (Paturel et al., 2003; Makarov et al., 2014), to remove any galaxies that are close to an edge-on configuration and not appropriate for our radial profile analysis. Our final resolved sample contains 43 galaxies.

In total, there are 33 galaxies with CO $J = 3{-}2$ detections from the JCMT. One of the main advantages to our molecular gas dataset is that the observations were all made using the same instrument, in the same CO transition, and with the same survey specifications. This homogeneous dataset provides a good basis for comparison between the different galaxies and different environments. The CO $J = 3 - 2$ data reduction process is described in Wilson et al. (2012) and will not be repeated here. A full analysis of the integrated properties of the spiral galaxies in this sample can be found in Mok et al. (2016).

For the H I data, we have collected maps from the VLA for 25 galaxies. First, we use data from the VLA Imaging of Virgo in Atomic Gas (VIVA) survey (Chung et al., 2009), where we have downloaded the moment zero maps from their website[1] for the 14 galaxies that overlap with the NGLS sample. Most of these observations were taken with the VLA in the B- or C-array configuration, with some beam sizes approaching the 15" resolution of the JCMT. There is also one galaxy, NGC3077, with H I data from the THINGS survey[2] (Walter et al., 2008). We observed an additional 10 NGLS galaxies with the VLA in the D-array configuration (VLA Project Identifier: AW701, 15B-111). The 6 AW701 galaxies were reduced manually using CASA while the newer 4 15B-111 galaxies were reduced using the automated VLA pipeline. To create the integrated H I intensity maps, we also perform a -1σ to 1σ noise

[1] http://www.astro.yale.edu/viva/

[2] http://www.mpia.de/THINGS/Overview.html

cut on the datacube. We present images of the integrated intensity (moment zero) maps for these 10 galaxies in Figure 3.1.

For the star formation rate data, we use the Hα observations from Sánchez-Gallego et al. (2012), which presented the star formation properties of the galaxies in the NGLS using a combination of archival data and new observations. We use the reduced FITS files, corrected using the R-band continuum filter and the provided conversion factor between Hα counts to Hα flux to convert the original image into units of the star formation rate. The full procedure to correct the Hα maps for contamination from the [N II] lines and the process to estimate the A(Hα) factor, the internal absorption of Hα, can be found in Sánchez-Gallego et al. (2012).

We supplement this with Hα data from the Herschel Reference Survey (Boselli et al., 2015), where we download the Hα images from their website[3]. We also include observations for one galaxy (NGC4273) from the Hα3 survey, taken from the GOLDMINE database (Gavazzi et al., 2012). For these galaxies, we first measure the Hα counts for the galaxies using an aperture created by eye to capture most of the flux from these galaxies. We combine this information with the published Hα flux values to determine the appropriate conversion factor. In order to maintain continuity with the previous papers in this series, we follow the procedure outlined in Sánchez-Gallego et al. (2012) to correct the Hα flux for [N II] contamination and A(Hα) factor. For many of these galaxies, we also had to manually align the Hα maps, as co-ordinate information was not included in the FITS files. For those cases, we compared to Digital Sky

[3] http://hedam.lam.fr/HRS/

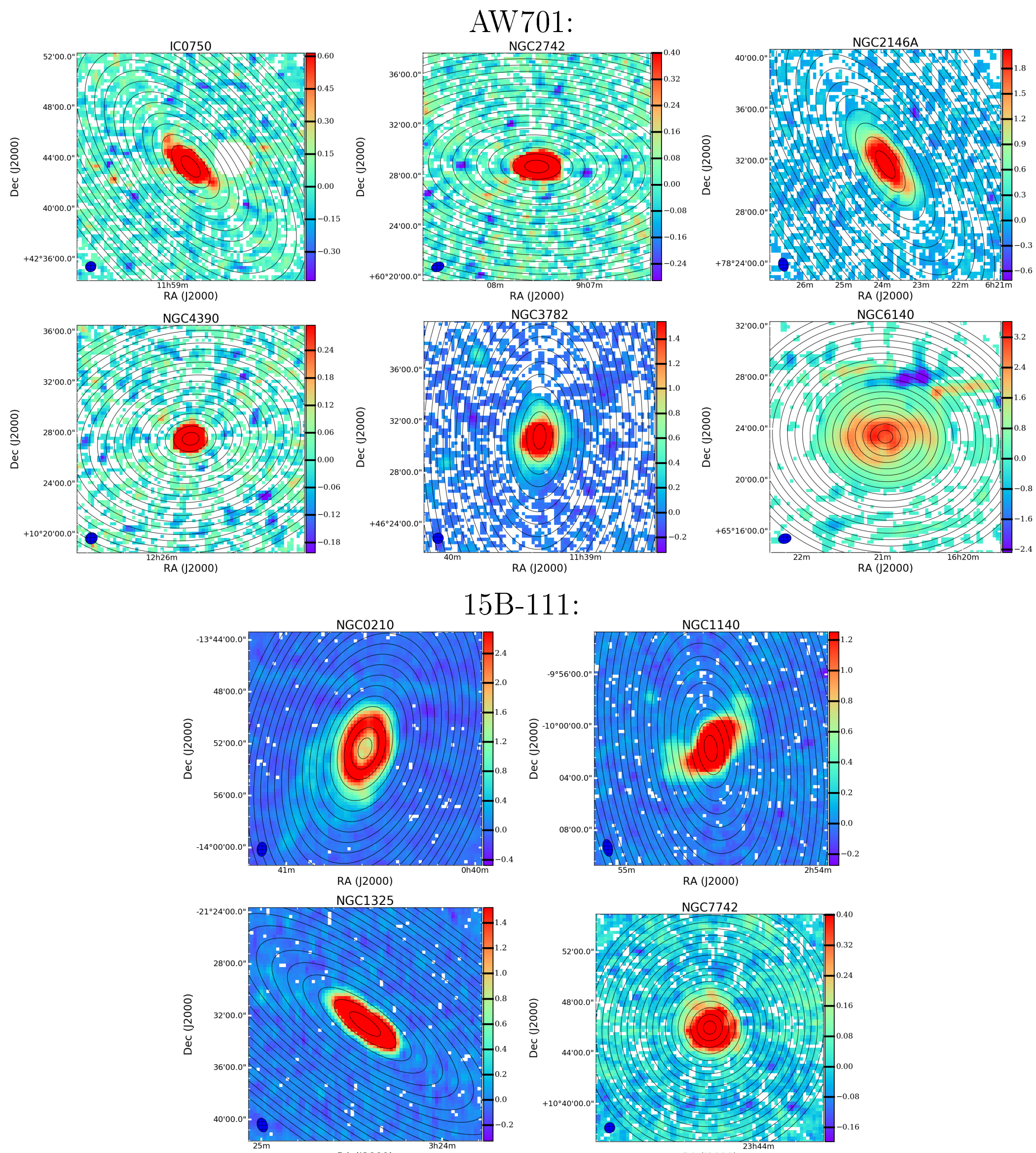

Figure 3.1 The H I 21 cm moment zero maps of the galaxies from the AW701 and 15B-111 VLA programs, in units of Jy beam^{-1} km s^{-1}. The annuli used for the creation of the radial profiles are overlaid in black and the beam is shown in the lower left corner of each image. The 6 AW701 galaxies are presented first, followed by the 15B-111 galaxies.

Survey images of the galaxies and fit to star positions using at least 5 stars for each image.

In summary, there are 25 galaxies with H I maps, 33 with H_2 maps, and 43 with Hα maps. More information about the sample can be found in Table 3.1, where the individual galaxies are listed, along with their available datasets, their inclinations and physical distances. Full tables of the key physical properties of the spiral galaxies in our sample can be found in Mok et al. (2016).

3.2.2 Integrated Properties of the Resolved Sample

3.2.2.1 Comparison with the Remaining NGLS Spiral Galaxies

First, we compare our resolved subset of 43 galaxies to the remaining sample of 55 NGLS spiral galaxies from Mok et al. (2016) that were not included in this paper, as they did not possess detected CO $J = 3 - 2$ emission or VLA H I observations or they have high inclinations. We find that the two samples have similar H I gas masses (log $\mathrm{M_{H_I}} = 9.16 \pm 0.05$ for the resolved sample vs. log $\mathrm{M_{H_I}} = 9.05 \pm 0.04$ for the non-included sample). The similar total H I gas mass is likely due to the H I flux selection imposed by the NGLS. We also find no significant difference between the integrated H I properties of the Virgo galaxies in the resolved sample, compared to the Virgo galaxies that were not included in this paper. These results indicate that we are not selecting a potentially biased H I sample out of the original H I-flux selected sample.

Table 3.1 Available H I, H_2, and Hα Data for the Galaxies in Our Sample

Galaxy[1]	Env[2]	H I source	H I beam size[3]	H I rms[3]	H_2[4]	Hα	Incl	Dist
-	-	-	-	[mJy/beam]	-	-	[deg]	[Mpc]
NGC0210	F	15B-111	66"×46"	1.75	D	HRS	55.4	22.4
NGC3437	F	-	-	-	D	HRS	72.8	20.1
NGC6140	F	AW701	60"×45"	2.16	ND	NGLS	32.2	17.8
NGC7742	F	15B-111	51"×49"	1.57	D	HRS	16.8	24.8
IC0750	G	AW701	51"×49"	1.30	D	NGLS	65.8	8.3
IC3908	G	-	-	-	D	HRS	73.2	19.0
NGC0450	G	-	-	-	D	NGLS	49.8	25.4
NGC1140	G	15B-111	79"×44"	1.51	ND	NGLS	73.8	20.1
NGC1325	G	15B-111	66"×47"	1.74	ND	NGLS	74.3	20.7
NGC2146A	G	AW701	63"×46"	1.50	ND	NGLS	69	25.9
NGC2742	G	AW701	62"×45"	1.24	D	NGLS	60.6	22.4
NGC3077	G	THINGS	14"×13"	0.94	D	NGLS	38.1	3.9
NGC3162	G	-	-	-	D	NGLS	37.1	20.7
NGC3227	G	-	-	-	D	NGLS	68.3	18.4
NGC3346	G	-	-	-	D	HRS	34.1	19.5
NGC3507	G	-	-	-	D	NGLS	31.9	15.5
NGC3684	G	-	-	-	D	HRS	50.8	18.4
NGC3782	G	AW701	51"×49"	1.26	ND	NGLS	60.3	14.3
NGC3982	G	-	-	-	D	HRS	29.9	20.1
NGC4041	G	-	-	-	D	NGLS	22	21.9
NGC4123	G	-	-	-	D	HRS	44.3	20.1
NGC4713	G	VIVA	26"×22"	1.96	D	HRS	23.8	10.9
NGC4771	G	-	-	-	D	HRS	74.4	17.2
NGC4772	G	VIVA	18"×15"	0.36	ND	NGLS	67.3	16.1
NGC4775	G	-	-	-	D	HRS	28.4	23.0
NGC4808	G	VIVA	40"×36"	0.59	D	HRS	69.2	12.0
NGC4254	V	VIVA	38"×33"	0.41	D	NGLS	20.1	16.7
NGC4273	V	-	-	-	D	GOLDMINE	26.9	16.7
NGC4294	V	VIVA	29"×27"	0.29	ND	HRS	70.2	16.7
NGC4298	V	VIVA	17"×16"	0.35	D	NGLS	58.4	16.7
NGC4303	V	-	-	-	D	HRS	18.1	16.7
NGC4383	V	VIVA	45"×38"	0.26	D	NGLS	63.7	16.7
NGC4390	V	AW701	58"×53"	1.16	ND	NGLS	43.3	16.7
NGC4396	V	VIVA	27"×27"	0.28	ND	HRS	71.6	16.7
NGC4430	V	-	-	-	D	NGLS	43.8	16.7
NGC4480	V	-	-	-	D	HRS	61.2	16.7
NGC4548	V	VIVA	17"×16"	0.30	ND	HRS	36.9	16.7
NGC4567	V	VIVA	17"×16"	0.36	D	NGLS	39.4	16.7
NGC4568	V	VIVA	17"×16"	0.36	D	NGLS	67.5	16.7
NGC4579	V	VIVA	42"×35"	0.45	D	NGLS	41.9	16.7
NGC4647	V	-	-	-	D	NGLS	31.6	16.7
NGC4651	V	VIVA	17"×16"	0.40	D	NGLS	49.5	16.7
NGC4654	V	VIVA	16"×16"	0.45	D	HRS	59.8	16.7

[1] Galaxies with both H I and H_2 data are in bold face.
[2] For the environment, F indicates field galaxies, G indicates group galaxies, and V indicates Virgo galaxies. A full explanation of our categories can be found in Mok et al. (2016)
[3] Beam sizes and rms from the H I maps in the VIVA survey are from Table 2 of Chung et al. (2009)
[4] For H_2 data, D indicates detected galaxies, ND indicates non-detected galaxies

On the other hand, the stellar masses for the resolved sample (log $M_* = 9.94 \pm 0.06$) are significantly higher than the non-included sample (log $M_* = 9.37 \pm 0.07$). In Mok et al. (2016), we found that the stellar mass for the CO $J = 3-2$ detected galaxies is significantly higher than the CO $J = 3-2$ non-detected galaxies. Thus, it is not surprising to see a similar difference in stellar mass, since this resolved sample would comprise most of the CO $J = 3-2$ detected galaxies, except for a few heavily inclined galaxies. In addition, the star formation rates are higher in the resolved sample. This is likely due to the strong link between H_2 gas and star formation, as well as between stellar mass and star formation. These results suggest that the resolved sample would not contain many of the gas-rich low surface brightness galaxies discussed in Mok et al. (2016) and in other surveys of these H I-rich objects, such as HIghMass (Huang & Kauffmann, 2014).

3.2.2.2 Comparison of the Virgo and non-Virgo Galaxies in the Resolved Sample

For our resolved sample, we present a summary of the global properties of the non-Virgo and Virgo galaxies in Table 3.2. In this analysis, we have combined the field and group galaxy samples to increase the number of galaxies in the non-Virgo sample.

Although the non-Virgo galaxies have higher H I masses, the difference in the stellar mass normalized H I masses is less significant, as shown by performing the Kolmogorov-Smirnov test on the two distributions. While Virgo galaxies have a higher average stellar mass, it is less than a 1σ difference and the Kolmogorov-Smirnov test shows that the two distributions cannot be distinguished. The other properties, such as star formation rate and specific star formation rate (sSFR), are also comparable between the two samples. These results give us more confidence that we are comparing between similar galaxies and probing the more subtle effects of environment.

The main difference between the Virgo and non-Virgo resolved samples is in the molecular gas properties. Since not all of these galaxies are detected in the CO $J = 3-2$ maps, as shown in Table 3.1, we have used the statistical technique of survival analysis on these two samples, as discussed in Mok et al. (2016). The resolved sample shows the same general trends as analysis from the full NGLS sample, with the Virgo galaxies possessing higher mean molecular gas masses, higher H_2-to-H I ratios, and lower star formation efficiencies (or longer molecular gas depletion times). For the total gas mass, the two samples are quite similar, suggesting that the cluster environment may be aiding in the conversion process between atomic and molecular gas. We will further explore these global results by measuring the radial profiles of these galaxies.

3.2.3 Creating Surface Density Maps

We convert the HARP CO $J = 3-2$ moment maps to a H_2 surface density map by assuming a CO-to-H_2 conversion factor of $X_{\rm CO} = 2{\times}10^{20}{\rm cm}^{-2}({\rm K\ km\ s}^{-1})^{-1}$ (Strong et al., 1988) or $\alpha_{\rm CO} = 3.2\ {\rm M}_\odot\ {\rm pc}^{-2}({\rm K\ km\ s}^{-1})^{-1}$. We use a constant line ratio (R_{31}) between CO $J = 3-2$ and CO $J = 1-0$ of 0.18, the average value found for galaxies in the NGLS (Wilson et al., 2012). This leads to the

Table 3.2 Global Properties of the non-Virgo and Virgo Resolved Samples

Mean Quantity	Non-Virgo (26)	Virgo (17)	KS - Test
log M_{H_I} [$M_\odot$]	9.24 ± 0.05	9.04 ± 0.08	$\underline{0.009}$
log M_* [$M_\odot$]	9.87 ± 0.07	10.05 ± 0.12	0.154
M_{H_I}/M_*	0.35 ± 0.06	0.15 ± 0.03	0.108
Distance [kpc]	18.6 ± 0.94	16.0	-
log SFR [$M_\odot$ yr^{-1}]	-0.29 ± 0.09	-0.25 ± 0.14	0.774
log sSFR [yr^{-1}]	-10.17 ± 0.09	-10.30 ± 0.10	0.610
log M_{H_I}/SFR [yr]	9.54 ± 0.07	9.29 ± 0.11	0.486
log M_{H_2}[1] [$M_\odot$]	8.35 ± 0.11	8.83 ± 0.13	$\underline{0.028}$[2]
log SFR/M_{H_2}[1] [yr]	-8.62 ± 0.11	-9.06 ± 0.10	$\underline{0.049}$[2]
M_{H_2}/M_*[1]	0.047 ± 0.012	0.095 ± 0.016	0.051[2]
M_{H_2}/M_{H_I}[1]	0.38 ± 0.14	1.43 ± 0.37	$\underline{0.007}$[2]
$M_{H_2} + M_{H_I}$ [$M_\odot$][1]	9.35 ± 0.05	9.35 ± 0.10	0.656[2]

Note: Underline indicates $p < 0.05$.
[1] CO non-detections taken into account using survival analysis; please refer to Mok et al. (2016) for more information.
[2] Log-rank test used, which takes into account censored data.

following relation between $\Sigma_{\mathrm{H_2}}$, the surface density of molecular hydrogen, and $I_{\mathrm{CO(3-2)}}$, the integrated CO $J = 3-2$ intensity:

$$\Sigma_{\mathrm{H_2}}[\mathrm{M_\odot\ pc^{-2}}] = 17.8 \times (\mathrm{R_{31}}/0.18)^{-1} I_{\mathrm{CO(3-2)}}[\mathrm{K\ km\ s^{-1}}] \quad (3.1)$$

To convert the VLA 21 cm moment zero maps into physical units, we combine equations 1 and 5 from Walter et al. (2008) and then convert to units of $\mathrm{M_\odot\ pc^{-2}}$. This leads to the following relationship, where Σ_{HI} is the surface density of H I, $\sum S\Delta\nu$ is the integrated flux density from the moment zero maps, and $\mathrm{FWHM_{maj}} \times \mathrm{FWHM_{min}}$ is a measure of the beam area:

$$\Sigma_{\mathrm{HI}}[\mathrm{M_\odot\ pc^{-2}}] = 8765.27 \times \frac{\sum S\Delta\nu[\mathrm{Jy\ beam^{-1} km\ s^{-1}}]}{\mathrm{FWHM_{maj}} \times \mathrm{FWHM_{min}}} \quad (3.2)$$

For the Hα maps, we convert the Hα counts into star formation rates using the procedure outlined in § 3.2.1. This process uses the conversion factor from Kennicutt et al. (2009), which assumes a Kroupa IMF (Kroupa & Weidner, 2003):

$$\mathrm{SFR}[\mathrm{M_\odot\ yr^{-1}}] = 5.5 \times 10^{-42}\, \mathrm{L(H\alpha)}[\mathrm{erg\ s^{-1}}] \quad (3.3)$$

where SFR is the star formation rate and L(Hα) is the Hα luminosity. When we generate radial profiles, we divide the star formation rates in each measured annulus by its physical size, as determined by the distance to each galaxy listed in Table 3.1. This results in a final measurement of the surface density of star formation (Σ_{SFR}) in units of $\mathrm{M_\odot\ yr^{-1}\ pc^{-2}}$.

We perform an additional data reduction step on the CO $J = 3-2$ and Hα data. Our VLA dataset has a wide variety of angular resolutions while our CO $J = 3-2$ dataset has a constant angular resolution of 15". To allow for analysis using a combination of two values (such as the H_2/H I ratio) and to better compare between the H_2 and H I datasets, we adopted a standard 60” resolution. For the galaxies observed using the D-array configuration, we convolved the CO $J = 3-2$ and Hα maps to the same resolution as the H I maps using the software package Starlink. For the VIVA dataset, observed using the VLA in the B/C configurations, we convolved all three maps (H_2, H I, and Hα) to our standard 60” resolution.

Finally, we correct for any inclination effects by multiplying our resulting maps with a $\cos i$ factor, with the inclinations provided from the HyperLeda database (Paturel et al., 2003).

3.2.4 Generating Radial Profiles

To generate the radial profiles for our galaxies, we use the co-ordinates, position angle, and inclination data from the HyperLeda database to define 20 concentric annuli. The widths of each ring along the minor axis is set to 30”, which is half of the standard angular resolution for our dataset. We then measured the mean values within each aperture using the apperadd command. For galaxy pairs that were collected in a single map, such as NGC4567 and NGC4568, the other galaxy was masked out manually from the individual maps. We note that the radial profiles will only extend as far out as the observed area in each map and may not include all 20 annuli, especially for the H_2 data.

Furthermore, an annulus is only included if it contains more than 5% valid (non-blank) pixels. We have tested more conservative thresholds, such as 25%, and it did not result in any significant difference in our profiles and results. However, it did reduce the amount of galaxies in our H_2 sample due to the localized nature of some of our CO $J = 3 - 2$ detections. To maximize the number of galaxies in our sample, we have maintained this low threshold.

To determine any systematic difference between the galaxies in the sample, we divide the physical radii by each galaxy's R_{25}, which is half of their D_{25} value from the HyperLeda database. This normalization is important because the Virgo galaxies in our sample are on average slightly closer and physically larger than the non-Virgo sample (Mok et al., 2016). A comparison using physical radii (kpc) may be affected by the differences in the size of the galaxies in the Virgo and non-Virgo samples and their distances.

Next, we tested three ways of combining the profiles to create the 'average' radial profile for our subsamples: the median, the mean, and the geometric mean. The geometric mean is the square root of the product of the input values. This is also equivalent to the log-average, where we perform the arithmetic mean on the logarthmic values.

We calculate the average profile at equally spaced points in the R_{25}-normalized radius, interpolating between the physical annuli points where necessary. The results of these three methods for the H I data are presented in the left plot of Figure 3.2 for the Virgo sample. These averages are only calculated in regions where there are more than three galaxies. The differences in the horizontal range that each radial profile spans depends on the number of galaxies in each sample and the interaction between the fixed size annuli used for the analysis and the distance to each individual galaxy.

The error bars on the mean are the statistical errors and the error bars on the median are based on the median absolute deviation. The error on the geometric mean uses the formula from Norris (1940):

$$S_G = G\frac{s_{\log x_i}}{\sqrt{n-1}} \tag{3.4}$$

where G is the geometric mean, $s_{\log x_i}$ is the standard deviation of the log values, and n is the number of galaxies. Since the stellar masses of the Virgo and non-Virgo samples are not significantly different and we are normalizing their radii using R_{25}, we can compare the standard error on the mean values of these similar objects. Note that the datapoints where we calculate the average profile will correspond to different points at the R/R_{25} for each individual galaxy, given their varying distances and sizes. Thus, we perform interpolation between the measured annuli points for the individual galaxy profiles when necessary. It is also possible for the error bars to be underestimated, because each data point in average profile is not fully independent of the others. On the other hand, this is compensated by the large number of individual galaxy profiles which goes into the averaging process.

We chose the geometric mean method to generate the average radial profile for our analysis. Compared to the median method, it provides a more stable profile. The median can produce ragged profiles, particularly at radii with few individual measurements. Compared to the mean method, the geometric mean is more representative. The simple mean can be biased by high outliers, especially when presented in a log-log plot. The choice of the particular averaging method does not change the overall results presented in this paper, especially between the median and the geometric mean methods.

Finally, we calculate the average R/R_{25} value for the galaxies in each average radial profile. To create a balance between the increased dataset available from combining our individual profiles and the angular resolution of our data, we decided to generate average radial profiles points at intervals which are the equivalent of 15” at the average R/R_{25} value for the galaxies making up the average profile.

3.2.5 Correcting Blank Pixels in H_2 Maps

The CO $J = 3-2$ maps for many of our galaxies contain large areas of blank pixels. This is due to the sensitivity limits of the observations and the data reduction procedure from Wilson et al. (2012), which removes regions of the map below a certain signal to noise limit. One approach is to assume that the non-detected pixels have no molecular gas present. This correction is performed by multiplying the raw value by the ratio of valid pixels to the total number pixels in the aperture. This can be considered a lower limit to the H_2 profile. Another approach is to add in the average 1σ noise of the map for those missing pixels. This second correction method assumes that the undetected pixels would take on the mean value from the noise map generated in the data reduction process, where a line width of 100 km/s is assumed. The final approach is to make no corrections to the average value of the detected pixels measured in the aperture, which we will call the uncorrected profile.

We compare these three methods to correct for these blank pixels in the right plot of Figure 3.2, looking at the H_2 radial profiles for our Virgo sample. These corrections are not very important within $R/R_{25} = 0.5$, the main target

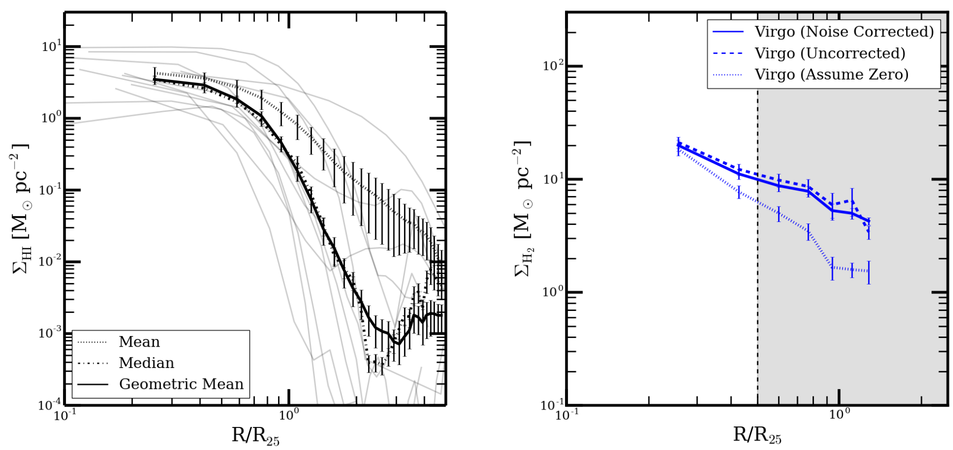

Figure 3.2 **Left:** A comparison of the results from using different methods for defining the radial profile for the population of Virgo galaxies, including mean (dotted), geometric mean (solid), and median (dot-dashed). Error bars for the mean are statistical. Error bars for the median method are based on median absolute deviation. Error bars for the geometric mean method are based on the formula from Norris (1940). We see that the mean profile is biased by high outliers, while the median method produces jagged profiles in regions due to a small number of galaxies. **Right:** The average H_2 surface density radial profiles, measured using the geometric mean method, for the Virgo galaxies in our sample. The radii are normalized by R_{25}. The dashed vertical line is at $R_{25} = 0.5$, the main target area of the NGLS survey, and results from the CO $J = 3-2$ maps are less reliable in the shaded region. The original, uncorrected profile (dashed line), noise corrected profile (solid line) and the profile assuming blank pixels have no gas (dotted line) is plotted. The three methods produce similar results in the reliable region near the centre, where most of the CO $J = 3-2$ pixels are detected.

area of the NGLS survey. Inside this region, most of the pixels are detected and the three curves are similar to each other. We decided to apply the noise correction method to all of the subsequent H_2 maps in our sample, as this is the most physical scenario. In general, the noise corrected profile provides similar results to the uncorrected case. The radial profile for the case where we assume no molecular gas is present in the blank pixels naturally produces steeper profiles, as it reduces the surface density in the outskirts of these galaxies.

3.3 Results and Discussion

3.3.1 H I Radial Profiles - Stripping in Group and Virgo Galaxies

We present the radial profiles for our sample of galaxies with available H I data in Figure 3.3. We separate the sample of galaxies by field, group, and Virgo samples and also between the Virgo and non-Virgo samples. All of the radial profiles have a relatively flat inner portion, which transitions into a steeper profile in the outskirts. We note that the galaxies in the Virgo cluster have truncated H I disks compared to non-Virgo galaxies, which was seen in previous studies of Virgo Cluster spirals (Cayatte et al., 1994). The new result here is that this truncation is seen even in this sample of H I-flux selected galaxies from the NGLS.

Comparing the smaller field and group samples, the field galaxies have a shallower decrease in the outskirts compared to the group galaxies. This would suggest a natural trend in H I disk sizes from the field to the group and then to the cluster environment. Given we only have 3 field galaxies with H I maps in our sample, we may need more observations to confirm this difference with the group sample. On the other hand, this scenario fits well with the picture of ram-pressure stripping, where higher density environments can strip away the ISM of spiral galaxies. Our result provides some more evidence for H I stripping in environments of relatively modest density. Observationally, H I-deficient galaxies have been found in the group environment, such as in Hickson Compact Groups (Martinez-Badenes et al., 2012). The Blind Ultra Deep H I Environmental Survey (BUDHIES) have also found a correlation between the fraction of H I detected galaxies and the mass of their host groups (Jaffé et al., 2016).

In addition, since this is a H I-flux selected sample from the NGLS, these galaxies still possess a relatively large amount of available cold gas. It is likely that the NGLS is preferentially selecting galaxies that are recently infalling into the Virgo Cluster or have not been strongly affected by the cluster environment. In addition, due to the H I-flux criteria and with most of the galaxies in the resolved sample detected in the CO $J = 3-2$ maps, we are selecting relatively high stellar mass galaxies that are less likely to be fully stripped according to semi-analytical models (Luo et al., 2016). Despite these caveats, the trends observed in the H I radial profile suggest that the environment can still play a big factor in changing the spatial distribution of the ISM inside these galaxies.

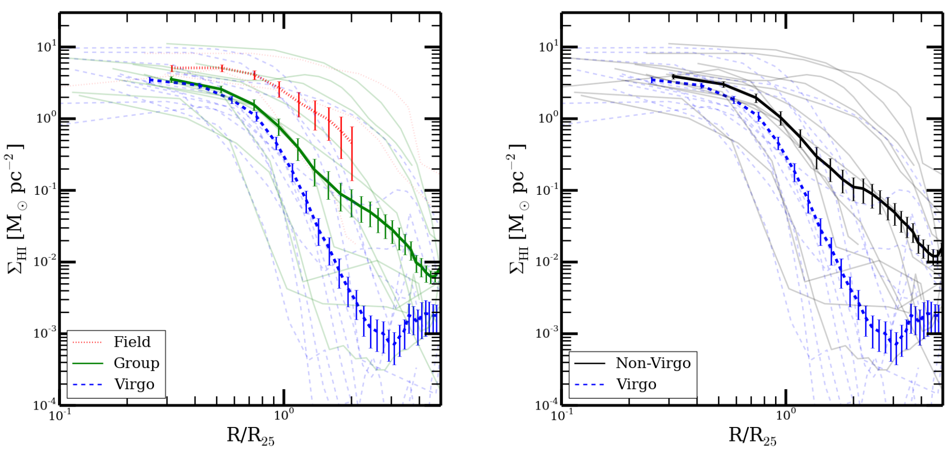

Figure 3.3 The radial profiles of H I surface density for the galaxies in our sample, calculated using the geometric mean method and normalized by R_{25}. The statistical error bars for each profile are plotted. The individual galaxy profiles are in the background. **Left:** The sample is separated into field (red-dotted), group (green), and Virgo (blue-dashed) populations. We see a reduction in the sizes of the H I disk, from field to group to the Virgo Cluster, suggesting H I properties are affected even in moderate density environments. **Right:** The sample is separated into the non-Virgo (black) and Virgo (blue-dashed) populations. Even for this H I-flux selected sample, the Virgo Cluster galaxies have truncated H I distributions in the outskirts compared to non-Virgo galaxies.

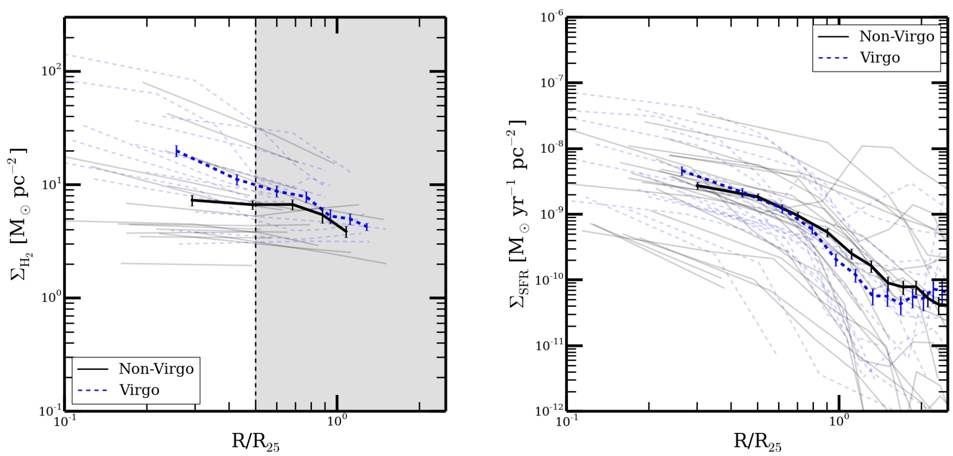

Figure 3.4 **Left:** The radial profiles of H_2 surface density for the galaxies in our sample, calculated using the geometric mean method and normalized by R_{25}. The statistical error bars for each profile are plotted. The individual galaxy profiles are in the background. The sample is separated into the non-Virgo (black) and Virgo (blue-dashed) populations. The dashed vertical line is at $R_{25} = 0.5$, the main target area of the NGLS survey, and results from the CO $J = 3-2$ maps are less reliable in the shaded region. On average, the Virgo galaxies are more H_2-rich at all radii, along with a steeper radial gradient. **Right:** The radial profiles of star formation rate surface density for the galaxies in our sample, calculated using the geometric mean method and normalized by R_{25}. The statistical error bars for each profile are plotted. The individual galaxy profiles are in the background. We see an enhancement in the star formation rates near the centre of Virgo galaxies, similar to the behaviour of the H_2 distribution. However, there are also hints of a truncation in their disks at large radii.

3.3.2 H_2 Radial Profiles - Enhancement in Virgo Galaxies

The H_2 radial profiles are presented in the left plot of Figure 3.4. With the small number of CO detected field galaxies and the short range over which we have enough galaxies to generate an average radial profile, the remaining figures will only show a comparison between the Virgo sample and the combined field and group samples. Comparing between the Virgo and non-Virgo samples, we see that the H_2 disk is not significantly truncated for Virgo galaxies. In fact, the H_2 surface density is enhanced near the centre. This is consistent with results from the integrated measurements (Mok et al., 2016), where we noted an increase in the H_2 gas mass for the Virgo galaxies in this H I flux selected sample.

As discussed in Section 3.3.1, the NGLS is a H I-flux selected survey and likely contains galaxies not yet strongly affected by the cluster environment. As a result, our sample may not be directly comparable to those from the Herschel Virgo Cluster Survey (HeViCS) or the Herschel Reference Survey (HRS), which contain a large population of H I-deficient objects that are also often H_2-deficient. Our results suggest that for recently infalling galaxies or galaxies in less extreme environments, molecular gas can be enhanced rather than reduced by the cluster environment.

A comparison of the H_2 and H I profiles for Virgo galaxies suggests that while the environment can play a role in truncating the H I disks in these galaxies, some of the gas may lose angular momentum and move towards the centre, into a region where it is more easily converted into molecular form. Simulations of light to moderate ram pressure stripping with cooling processes have shown that low density gas could be preferentially removed from the outskirts while enhancing the amount of high density gas near the centre (Tonnesen & Bryan, 2009; Bekki, 2014). Observations of Hickson Compact Groups have shown hints of an enhancement in the molecular gas content compared to isolated galaxies (Martinez-Badenes et al., 2012). Changes in the molecular gas distribution have been observed for the galaxies in the Abell 1367 cluster ($z = 0.022$), with some galaxies showing signs of H_2 enhancements (Scott et al., 2013, 2015).

Galaxy interactions, which are more common in the cluster environment, may also aid in this process. For example, results from the AMIGA sample of isolated galaxies suggests a possible molecular gas enhancement for interacting galaxies of approximately 0.2−0.3 dex (Lisenfeld et al., 2011).

3.3.3 SFR Radial Profiles

We present the radial profiles of the Hα derived star formation rates in the right plot of Figure 3.4. Near the central regions, there is an enhancement in the star formation rate density for the Virgo sample, similar to the trends from the H_2 profiles. The consistency between these two datasets is likely caused by the strong link between molecular gas and star formation. Previous observations have also shown that interactions can drive increases to the star formation rate (Kennicutt et al., 1987; Ellison et al., 2013), which may also contribute to the increase in the star formation rate for the Virgo sample, as several of our galaxies are in close pairs (NGC4567/NGC4568).

At large radii, there are hints of a possible truncation for Virgo galaxies, which was also seen in Koopmann et al. (2006). The behaviour of the star formation rate profiles in this region ($R/R_{25} > 1$) is less reliable, as the measurement comes from places outside where the Hα flux is normally observed for these galaxies. The large scatter in the distribution of individual galaxy profiles is likely due to imperfect removal of other sources (such as stars) and potential differences in the neighbourhoods of these galaxies.

3.3.4 Environmental Trends in the Spatial Distribution of the ISM

In Figure 3.5, we present the results of the H_2/H I and H_2 + H I profiles for the smaller sample of 15 galaxies with both sets of measurements. We find that the Virgo galaxies generally have a higher H_2/H I ratio than non-Virgo galaxies, which is also seen in a comparison of the integrated measurements from Mok et al. (2016). The non-Virgo galaxies have a relatively flat profile, at a value of around unity in the region where both H_2 and H I are detected. Due to the small number of CO $J = 3 - 2$ detected galaxies for the non-Virgo sample and the procedure used in the creation of the radial profiles, we do not probe this ratio in the central region. For the Virgo galaxies, the H_2/H I ratio rises towards the centre as expected, marking the transition to a molecular gas dominated regime. On the other hand, the slight increase in the H_2/H I ratio for Virgo galaxies at large radii is likely not significant, as it falls in the region beyond the main NGLS survey area.

For the total gas surface density (H_2 + H I) profile, we find differences between the Virgo and non-Virgo samples. Near the centre, the non-Virgo sample have a flatter profile than the Virgo sample, due to the strong contribution from the molecular gas component. In the outskirts, the truncation in the H I disks observed for the profiles of Virgo galaxies is largely responsible for their steep total gas profiles. Steeper H_2 profiles have also been found for Virgo galaxies from the HeViCS (Pappalardo et al., 2012), especially for H I-deficient galaxies, and fits with the idea that ram pressure stripping may be preferentially removing gas in the outskirts and enhancing the high density gas near the centre, as discussed for the H_2 surface density profiles.

3.3.5 Depressed Star Formation Efficiency at All Radii in Virgo Spirals

With the Hα-derived star formation rate and the H_2 data, we can calculate the star formation efficiency (or its reciprocal, the molecular gas depletion time). The results are presented in Figure 3.6. From the SFR/H_2 plot, we find that Virgo galaxies generally have a lower star formation efficiency. This result has also been seen in the integrated measurements from Mok et al. (2016). The profile is relatively flat in the inner regions for both samples, with a decrease at large radii for the Virgo sample. This decline in the star formation efficiency may not be physically significant, as it sits outside of the main region of the HARP instrument in the NGLS survey and is in the regime where noise corrections to the CO $J = 3 - 2$ data become important.

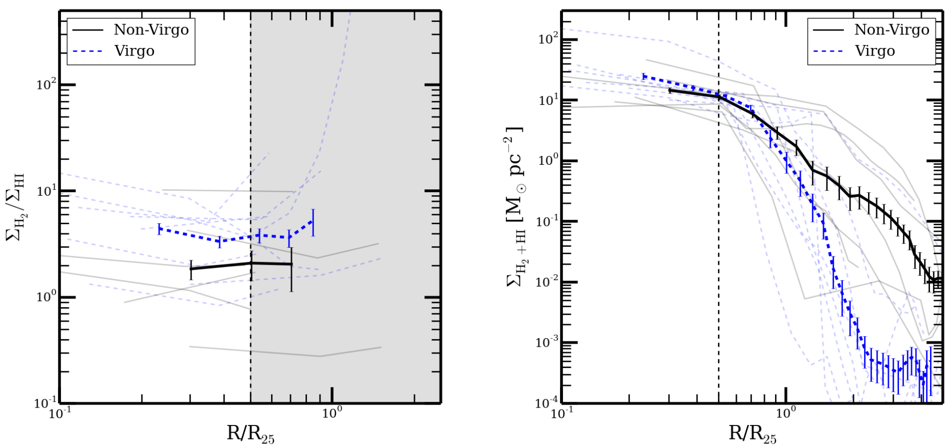

Figure 3.5 **Left:** The mean radial profiles of the H_2-to-H I ratio for the galaxies in our sample, calculated using the geometric mean method and normalized by R_{25}. The statistical error bars for each profile are plotted. The individual galaxy profiles are in the background. The sample is separated into the non-Virgo (black) and Virgo (blue-dashed) populations. The dashed vertical line is at $R_{25} = 0.5$, the main target area of the NGLS survey, and results from the CO $J = 3-2$ maps are less reliable in the shaded region. The H_2-to-H I ratio shows an enhancement for Virgo galaxies, especially near the centre. **Right:** The radial profiles of the total gas surface density for the galaxies in our sample, calculated using the geometric mean method and normalized by R_{25}. The statistical error bars for each profile are plotted. The individual galaxy profiles are in the background. There is a steeper radial distribution for Virgo galaxies compared to non-Virgo galaxies, with more gas concentrated near the centre. Ram pressure stripping is likely playing a role in removing low density gas in the outskirts and enhancing the high density gas near the centre.

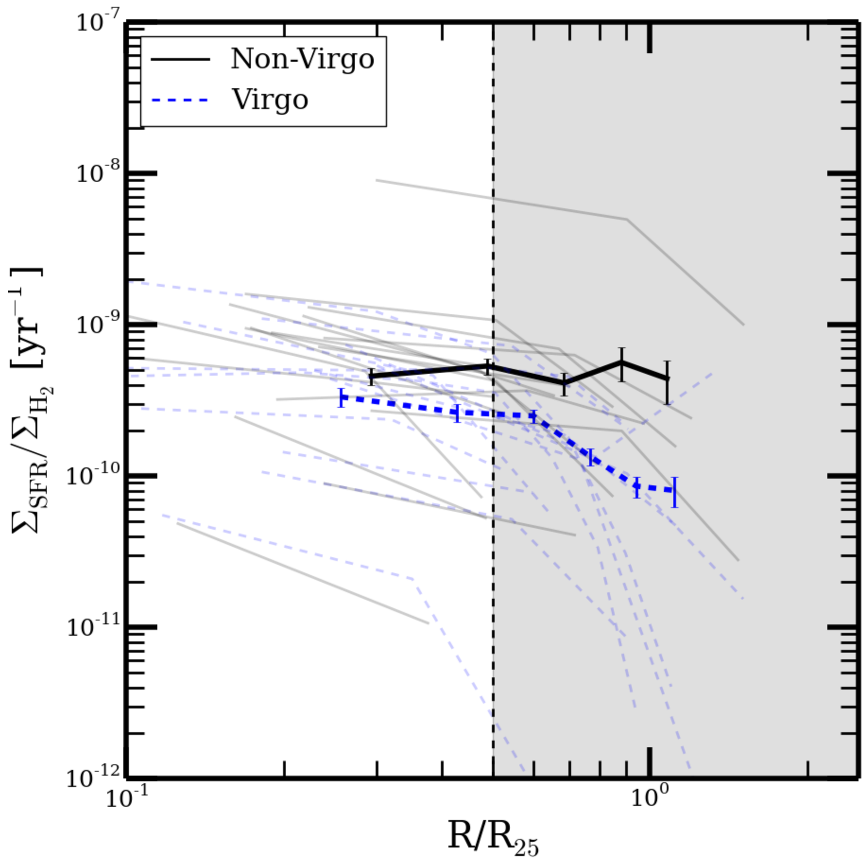

Figure 3.6 The SFR/H_2 surface density radial profiles for the galaxies in our sample, calculated using the geometric mean method and normalized by R_{25}. The statistical error bars for each profile are plotted. The individual galaxy profiles are in the background. The sample is separated into the non-Virgo (black) and Virgo (blue-dashed) populations. The dashed vertical line is at $R_{25} = 0.5$, the main target area of the NGLS survey, and results from the CO $J = 3 - 2$ maps are less reliable in the shaded region. Both profiles show a relatively flat trend with radius, with the Virgo galaxies offset at a lower star formation efficiency (or longer molecular gas depletion time), similar to global results presented in Mok et al. (2016).

The flatness in the radial profiles of the star formation efficiency has been seen in previous studies, which have found near constant molecular gas depletion times for spiral galaxies (Leroy et al., 2008; Bigiel et al., 2011; Leroy et al., 2012). The absolute values are also in line with these previous results, which have usually found gas depletion times in the ∼2 Gyr range. As stated previously, the reduction in the star formation efficiency at larger radii is likely due to the limitations in the survey sensitivity and mapping area.

We also find an average offset in the SFR/H_2 plot between the Virgo and non-Virgo profiles of $\sim 40\%$, which was also present in the integrated measurements from Mok et al. (2016). While Virgo galaxies generally have higher molecular gas masses than non-Virgo galaxies, they are relatively inefficient at turning this fuel into stars. One possibility to explain this result is that there are other factors in the cluster environment, such as difference in the molecular gas properties (pressure, temperature) or larger-scale dynamical stabilization (Martig et al., 2009) that may be inhibiting the process of star formation in our Virgo sample. A related effect is the possible trend of star formation efficiency with stellar masses (Saintonge et al., 2011; Schruba et al., 2011), where higher mass galaxies have lower star formation efficiencies. Our Virgo sample has a slightly higher mean stellar mass ($\log M_* = 10.05 \pm 0.12$) compared to the non-Virgo sample ($\log M_* = 9.87 \pm 0.07$), which may contribute to this observed difference. However, given the large scatter in these relationships and the low mean stellar mass of our sample, it is hard to quantify its effect on the star formation efficiency. A final reason may be metallicity effects (Schruba et al., 2011), which could affect the observed CO intensity and hence the SFR-to-CO ratio. In this paper, as in other papers in the series, we have used a constant

CO-to-H_2 conversion factor and a constant line ratio between CO $J = 3-2$ and CO $J = 1-0$. Since most of our galaxies are normal spiral galaxies in a small range of stellar masses, it seems unlikely they would have metallicities of more than a factor of 2 below solar, where these effects become significant (Wilson, 1995; Bolatto et al., 2008).

3.4 Conclusions

We present an analysis of the radial profiles of a sample of 43 H I-flux selected spiral galaxies from the JCMT Nearby Galaxies Legacy Survey (NGLS) with resolved JCMT H_2 and/or VLA H I maps. This sample includes field, group, and Virgo Cluster galaxies, and their gaseous disks can act as important probes for environmental effects. Using this gas-rich sample of spiral galaxies, we find significant environmental variations in the spatial distribution of the ISM, including the H I and H_2 radial profiles, as well as in their star formation properties.

- We confirm that the H I disks are truncated in the Virgo sample, compared to the non-Virgo sample. This result is well-known from previous studies of the atomic gas distribution inside clusters (Cayatte et al., 1994), but we also observe this same effect for these relatively gas-rich galaxies. Comparing between the smaller group and field samples, we find that there is a decrease in the H I disk size for group galaxies compared to field galaxies, which may be related to the trends in H I properties with group masses (Jaffé et al., 2016) and suggests that the environment affects the H I gas even in moderate density regions.

- We find that the H_2 distribution is enhanced for Virgo galaxies, especially near the centre, which results in a significantly higher H_2 to H I ratio for Virgo galaxies. This matches the results found using integrated measurements of these galaxies in Mok et al. (2016). The steeper radial profile for the total gas content (H I + H_2), even for these gas-rich objects, suggests that the environment may play a role in determining the spatial distribution of the ISM inside these galaxies. The most likely scenario is moderate ram pressure stripping that preferentially removes low-density gas in the outskirts of these spiral galaxies and aids in the creation of higher density gas near the centre (Tonnesen & Bryan, 2009). Another possibility is interactions in the Virgo sample, as enhancements in molecular gas have also been seen in interacting isolated galaxies (Lisenfeld et al., 2011) and in compact group galaxies (Martinez-Badenes et al., 2012).

- The Hα star formation rate data for our galaxies show similar trends as the H_2 distribution. There is an enhancement in the star formation rate surface density for Virgo galaxies near the centre, which is likely related to the increase in the molecular gas surface density. Interactions in the Virgo sample, as discussed for the H_2 profiles, may also enhance star formation (Kennicutt et al., 1987; Ellison et al., 2013). We also find hints of a Hα truncation at large radii for Virgo galaxies, which has been found in other surveys of cluster spirals (Koopmann et al., 2006).

- We find that the star formation efficiency (SFR/H_2) is relatively constant with radius for the Virgo and non-Virgo samples. This is consistent with the near constant molecular gas depletion times found in other surveys for normal spiral galaxies (Bigiel et al., 2011; Leroy et al., 2012). However, the star formation efficiency for the Virgo galaxies is on average $\sim 40\%$ lower than non-Virgo galaxies. This variation may be the result of differences in the star formation process for Virgo galaxies or variations in the molecular gas properties (pressure, temperature, metallicity).

3.5 Acknowledgments

The research of CDW is supported by grants from NSERC (Canada). JHK acknowledges financial support from the Spanish Ministry of Economy and Competitiveness (MINECO) under grant number AYA2013-41243-P.

The James Clerk Maxwell Telescope is operated by the East Asian Observatory on behalf of The National Astronomical Observatory of Japan, Academia Sinica Institute of Astronomy and Astrophysics, the Korea Astronomy and Space Science Institute, the National Astronomical Observatories of China and the Chinese Academy of Sciences (Grant No. XDB09000000), with additional funding support from the Science and Technology Facilities Council of the United Kingdom and participating universities in the United Kingdom and Canada. The National Radio Astronomy Observatory is a facility of the National Science Foundation operated under cooperative agreement by Associated Universities, Inc. This work is based [in part] on archival data obtained with the Spitzer Space Telescope, which is operated by the Jet Propulsion Laboratory, California Institute of Technology under a contract with NASA. Support for this work was provided by an award issued by JPL/Caltech. We acknowledge the usage of the HyperLeda database (http://leda.univ-lyon1.fr). This research has made use of the GOLDMine Database. This research has made use of data from HRS project. HRS is a Herschel Key Programme utilising Guaranteed Time from the SPIRE instrument team, ESAC scientists and a mission scientist. The HRS data was accessed through the Herschel Database in Marseille (HeDaM - http://hedam.lam.fr) operated by CeSAM and hosted by the Laboratoire d'Astrophysique de Marseille.

The Digitized Sky Surveys were produced at the Space Telescope Science Institute under U.S. Government grant NAG W-2166. The images of these surveys are based on photographic data obtained using the Oschin Schmidt Telescope on Palomar Mountain and the UK Schmidt Telescope. The plates were processed into the present compressed digital form with the permission of these institutions. The National Geographic Society - Palomar Observatory Sky Atlas (POSS-I) was made by the California Institute of Technology with grants from the National Geographic Society. The Second Palomar Observatory Sky Survey (POSS-II) was made by the California Institute of Technology with funds from the National Science Foundation, the National Geographic Society, the Sloan Foundation, the Samuel Oschin Foundation, and the Eastman Kodak Corporation. The Oschin Schmidt Telescope is operated by the California Institute of Technology and Palomar Observatory.The UK Schmidt Telescope was operated by the Royal Observatory Edinburgh, with funding from the UK Science and Engineering Research Council (later the UK Particle Physics and Astronomy Research Council), until 1988 June, and thereafter by the Anglo-Australian Observatory. The blue plates of the southern Sky Atlas and its Equatorial Extension (together known as the SERC-J), as well as

the Equatorial Red (ER), and the Second Epoch [red] Survey (SES) were all taken with the UK Schmidt.

Bibliography

Bekki K., 2014, MNRAS, 438, 444

Bigiel F., et al., 2011, ApJ, 730, L13

Blanton M. R., Moustakas J., 2009, ARA&A, 47, 159

Bolatto A. D., Leroy A. K., Rosolowsky E., Walter F., Blitz L., 2008, ApJ, 686, 948

Boselli A., Cortese L., Boquien M., Boissier S., Catinella B., Gavazzi G., Lagos C., Saintonge A., 2014, A&A, 564, A67

Boselli A., Fossati M., Gavazzi G., Ciesla L., Buat V., Boissier S., Hughes T. M., 2015, A&A, 579, A102

Cayatte V., van Gorkom J. H., Balkowski C., Kotanyi C., 1990, AJ, 100, 604

Cayatte V., Kotanyi C., Balkowski C., van Gorkom J. H., 1994, AJ, 107, 1003

Chung A., van Gorkom J. H., Kenney J. D. P., Crowl H., Vollmer B., 2009, AJ, 138, 1741

Dressler A., 1980, ApJ, 236, 351

Ellison S. L., Mendel J. T., Patton D. R., Scudder J. M., 2013, MNRAS, 435, 3627

Gavazzi G., Fumagalli M., Galardo V., Grossetti F., Boselli A., Giovanelli R., Haynes M. P., Fabello S., 2012, A&A, 545, A16

Gunn J. E., Gott III J. R., 1972, ApJ, 176, 1

Haynes M. P., Giovanelli R., 1986, ApJ, 306, 466

Huang M.-L., Kauffmann G., 2014, MNRAS, 443, 1329

Jaffé Y. L., et al., 2016, MNRAS, 461, 1202

Kenney J. D. P., Young J. S., 1989, ApJ, 344, 171

Kennicutt Jr. R. C., Roettiger K. A., Keel W. C., van der Hulst J. M., Hummel E., 1987, AJ, 93, 1011

Kennicutt Jr. R. C., et al., 2009, ApJ, 703, 1672

Koopmann R. A., Haynes M. P., Catinella B., 2006, AJ, 131, 716

Kroupa P., Weidner C., 2003, ApJ, 598, 1076

Larson R. B., Tinsley B. M., Caldwell C. N., 1980, ApJ, 237, 692

Leroy A. K., Walter F., Brinks E., Bigiel F., de Blok W. J. G., Madore B., Thornley M. D., 2008, AJ, 136, 2782

Leroy A. K., et al., 2012, AJ, 144, 3

Lisenfeld U., et al., 2011, A&A, 534, A102

Luo Y., Kang X., Kauffmann G., Fu J., 2016, MNRAS, 458, 366

Makarov D., Prugniel P., Terekhova N., Courtois H., Vauglin I., 2014, A&A, 570, A13

Martig M., Bournaud F., Teyssier R., Dekel A., 2009, ApJ, 707, 250

Martinez-Badenes V., Lisenfeld U., Espada D., Verdes-Montenegro L., García-Burillo S., Leon S., Sulentic J., Yun M. S., 2012, A&A, 540, A96

McGee S. L., Balogh M. L., Bower R. G., Font A. S., McCarthy I. G., 2009, MNRAS, 400, 937

Mok A., et al., 2016, MNRAS, 456, 4384

Moore B., Katz N., Lake G., Dressler A., Oemler A., 1996, Nature, 379, 613

Norris N., 1940, The Annals of Mathematical Statistics, 11, 445

Pappalardo C., et al., 2012, A&A, 545, A75

Paturel G., Petit C., Prugniel P., Theureau G., Rousseau J., Brouty M., Dubois P., Cambrésy L., 2003, A&A, 412, 45

Peng Y.-j., et al., 2010, ApJ, 721, 193

Peng Y.-j., Lilly S. J., Renzini A., Carollo M., 2012, ApJ, 757, 4

Saintonge A., et al., 2011, MNRAS, 415, 61

Sánchez-Gallego J. R., Knapen J. H., Wilson C. D., Barmby P., Azimlu M., Courteau S., 2012, MNRAS, 422, 3208

Schruba A., et al., 2011, AJ, 142, 37

Scott T. C., Usero A., Brinks E., Boselli A., Cortese L., Bravo-Alfaro H., 2013, MNRAS, 429, 221

Scott T. C., Usero A., Brinks E., Bravo-Alfaro H., Cortese L., Boselli A., Argudo-Fernández M., 2015, MNRAS, 453, 328

Strong A. W., et al., 1988, A&A, 207, 1

Tonnesen S., Bryan G. L., 2009, ApJ, 694, 789

Walter F., Brinks E., de Blok W. J. G., Bigiel F., Kennicutt Jr. R. C., Thornley M. D., Leroy A., 2008, AJ, 136, 2563

Wilson C. D., 1995, ApJ, 448, L97

Wilson C. D., et al., 2012, MNRAS, 424, 3050

Chapter 4

The JINGLE Survey – Variations in the Dust and CO Properties in a Sample of Gas-Rich Galaxies at $0.01 < z < 0.05$

Angus Mok [1], C. D. Wilson[1], and the JINGLE Collaboration

[1] Department of Physics & Astronomy, McMaster University, Hamilton, Ontario L8S 4M1, Canada

Abstract

JINGLE is a sample of 193 Herschel 250μm and 350 μm detected, gas-rich, star-forming galaxies with planned JCMT SCUBA-2 dust continuum measurements and a smaller subset of 97 with RxA3m CO $J = 2-1$ observations. We use the initial Data Release 1 (DR1) from observations of the first half of the sample of galaxies to determine their ISM and star formation properties. There is a

strong correlation between the molecular gas mass estimated using the 850 μm and CO $J = 2-1$ observations. We find that the H_2-to-H I ratio and the molecular gas depletion times do not change significantly with stellar mass. Finally, we do not find any significant variations in the JINGLE DR1 sample with environment parameters, such as the host halo mass, local environment density, and location in a phase-space diagram.

4.1 Introduction

In the Universe, galaxies can be found isolated from other similarly sized neighbours, inside groups of tens of galaxies, and in clusters with thousands of close neighbours. The star formation properties of galaxies located inside high density environments are different from those found outside. For example, there is an increase in the number of red, passive galaxies in comparison to blue, star-forming galaxies (Blanton & Moustakas, 2009). There is also a noticeable decline in the fraction of blue, star-forming galaxies inside clusters since $z \sim 0.5$ (Butcher & Oemler, 1984). Recent analysis shows that this effect is due to the large reduction in the specific star formation rate for cluster galaxies, in excess of the expected decline in cosmic star formation rate (Haines et al., 2013).

Stars are formed from the collapse of the dense molecular gas, which is a major component of the Interstellar Medium (ISM) inside star-forming galaxies (Leroy et al., 2008; Saintonge et al., 2011a). Initial studies of the effect of the environment on the ISM have focused on the atomic component. For example, inside clusters, there is a deficiency in atomic gas (Chamaraux et al., 1980) and a truncation in their atomic gas disks (Cayatte et al., 1990, 1994).

The extended atomic disks are prone to the effects of ram pressure stripping (Gunn & Gott, 1972; Bekki, 2014) and tidal harassment (Moore et al., 1996, 1998). Since the atomic gas is likely a reservoir for the creation of molecular gas and ultimately star formation, direct measurements of the molecular gas component are important in an analysis of environmental effects.

Past studies of the effects of environment on the star-forming molecular gas inside galaxies have focused on the Virgo Cluster, the nearest cluster to the Milky Way. Initial observation by Kenney & Young (1989) revealed the survival of molecular gas in many H I-deficient Virgo spirals. More recent studies by the Herschel Virgo Survey (Corbelli et al., 2012) and the Herschel Reference Survey (Boselli et al., 2014) show a correlation between H I and H_2 stripping for Virgo galaxies and suggests that the cluster environment can remove molecular gas, though to a lesser extent than the atomic gas. In lower density environments, galaxies inside Hickson Compact Groups (Martinez-Badenes et al., 2012) and interacting galaxies (Lisenfeld et al., 2011) have shown enhancement in their molecular gas content.

Given these interesting variations, we require an analysis of gas-rich star-forming galaxies across multiple groups and clusters. One example is the Nearby Galaxies Legacy Survey (NGLS), a H I-flux (> 6.3 Jy km s^{-1}) selected sample of galaxies within a distance of 25 Mpc. The original sample contains galaxies of all morphological types (Wilson et al., 2012), but the environmental analysis presented in Mok et al. (2016, 2017) and reproduced in Chapter 2 and 3 of the thesis only considered spiral galaxies. Divided up between the field, group, and Virgo subsamples, Mok et al. (2016) found a possible enhancement in the molecular gas fraction and a larger H_2-to-H I ratio in the Virgo subsample. In addition, the mean molecular gas depletion time is longer for spiral galaxies inside the Virgo Cluster. Using resolved HARP and VLA maps, Mok et al. (2017) found that the molecular gas and total gas radial profiles are enhanced near the centre of the galaxy for Virgo Cluster galaxies, but truncated in the outskirts. These observations are consistent with simulations which suggest that moderate ram pressure stripping can aid in the formation of molecular gas and possibly enhance star formation (Tonnesen & Bryan, 2009; Bekki, 2014).

In this paper, we extend our analysis to a wider range of redshifts and environments with the JCMT dust and gas In Nearby Galaxies Legacy Exploration (JINGLE) sample. The JINGLE survey is a JCMT survey which will observe a sample of 193 Herschel-selected galaxies within $0.01 < z < 0.05$ in the 850 μm and 450 μm dust continuum bands using SCUBA-2 (Saintonge et al., in prep). In addition, JINGLE will observe the CO $J = 2 - 1$ line for a subsample of 95 galaxies using RxA3m (Xiao et al., in prep).

The JINGLE galaxies are selected from galaxies in the H-ATLAS survey (Rigby et al., 2011), in fields which overlap with optical IFU surveys, such as the Mapping Nearby Galaxies at APO (MaNGA) and the Sydney-Australian-Astronomical-Observatory Multi-object Integral-Field Spectrograph (SAMI) surveys, as well as the Arecibo Legacy Fast ALFA (ALFALFA) H I survey. The galaxies also are required to be detected in the 250 μm and 350 μm Herschel bands, which suggests they are dust-rich galaxies with high star formation rates. Furthermore, JINGLE galaxies are also within the redshift range of

$0.01 < z < 0.05$ and have stellar masses within the range of $10^{9.5} < \mathrm{M}_* < 10^{11.5}$. Some of the main goals of the JINGLE survey are to characterize the dust properties for a large sample of nearby galaxies, determine their gas-to-dust ratio, and measure important scaling relations with other galaxy properties. A full description of the JINGLE survey is presented in the overview paper by Saintonge et al. (in prep).

One past study that is very similar to the JINGLE survey is the CO Legacy Database for the GALEX Arecibo SDSS Survey (COLD GASS) (Saintonge et al., 2011a,b), which we will also use as a comparison sample in our analysis. They used the IRAM 30 meter telescope to measure the CO $J = 1 - 0$ line for a sample of 350 galaxies from the SDSS survey with H I detections. Both the COLD GASS and JINGLE surveys use the same Chabrier IMF and assumed cosmology, as well as SED-fitting based galaxy properties, such as star formation rates. Furthermore, COLD GASS galaxies are in the redshift range of $0.025 < z < 0.05$, comparable to the redshift limits of $0.01 < z < 0.05$ for JINGLE. However, the stellar mass selection of COLD GASS is $10^{10} < \mathrm{M}_* < 10^{11.5}$, higher than the stellar mass limits of $10^{9.5} < \mathrm{M}_* < 10^{11.5}$ for JINGLE. Therefore, the COLD GASS survey is sampling on average more distant and higher mass galaxies compared to JINGLE. Finally, the Herschel selection means that all the JINGLE galaxies are star-forming and gas-rich, which is not the case for the COLD GASS sample.

In Section 2, we describe the general sample properties and a summary of the data sources used in this paper. In Section 3, we present the group catalogue used to match with the JINGLE sample and the important environment parameters used in the analysis. In Section 4, we outline the main results, including variations of galaxy properties with host halo mass, the local environment density, and the location of the galaxy in the velocity-radius phase space of its host group.

4.2 Data Sources and Reduction

The primary set of observations in this analysis is the molecular gas mass of the JINGLE galaxies, which we can estimate using JCMT observations in two different ways. The Data Release 1 (DR1) includes 450 μm and 850 μm measurements for 105 galaxies and CO $J = 2 - 1$ line measurements for 35 galaxies. We also make use of the complementary multi-wavelength data compiled for the JINGLE sample (Saintonge et al., in prep).

4.3 Molecular Gas Masses Using 850μm SCUBA-2 Data

SCUBA-2 is a 10,000 pixel bolometer on the JCMT (Holland et al., 2013), which observes in the 450 μm and 850 μm wavelength bands. The JINGLE team is performing detailed dust Spectral Energy Distribution (SED) modelling, combining Herschel and JCMT SCUBA-2 measurements to determine properties such as the dust temperature, the dust emissivity spectral index (β), and the total dust mass (De Looze et al., in prep). These finalized numbers will be incorporated into the environment analysis when available, but in the meantime, there is a straightforward way to obtain a first-order estimate of the molecular gas component inside JINGLE galaxies using the 850 μm flux alone.

Observations of a sample of local and high redshift galaxies have shown a linear correlation between the 850 μm luminosity and the molecular gas mass (Scoville et al., 2014, 2016). This indicates that there is a strong link between the molecular gas and dust distributions inside star-forming galaxies. From a sample of 38 nearby galaxies, Thomas et al. (2004) found that the scale-length of the 850 μm emission is less than half that of the more extended atomic gas disk. Therefore, the dust continuum data can be used as a good estimator of the molecular gas content for JINGLE galaxies.

Scoville et al. (2016) measured the relationship between these two quantities for his sample of galaxies, where he assumed a CO-to-H_2 conversion factor ($X_{\rm CO}$) value of 3×10^{20} cm^{-2} (K km s^{-1})$^{-1}$. In this equation, $\rm M_{mol}$ is the molecular gas mass in units of the solar mass, taking into account a factor of 1.36 for Helium and heavier elements, and $\rm L_{850\mu m}$ is the 850 μm luminosity in units of erg s^{-1} Hz^{-1}.

$$\mathrm{M_{mol}}\ [\mathrm{M_\odot}] = \frac{1}{(6.7 \pm 0.17) \times 10^{19}} \times \left(\frac{X_{\rm CO}}{3 \times 10^{20}}\right) \times \mathrm{L_{850\mu m}}\ [\mathrm{erg\ s^{-1}\ Hz^{-1}}] \quad (4.1)$$

For the JINGLE galaxies, we will assume a value of 2×10^{20} cm^{-2} (K km s^{-1})$^{-1}$ for the CO-to-H_2 conversion factor, in order to be consistent with the COLD GASS survey. We also use $\rm M_{H_2}$ for this analysis instead of $\rm M_{mol}$ in order to match the dataset from COLD GASS. Finally, calculation of the 850 μm luminosity is based on the following formula from Scoville et al. (2016), simplified for observations at the rest frequency of 850 μm and assuming a dust spectral index (β) of 1.8. In this equation, $\rm S_{850\mu m}$ is the 850 μm flux in units of Janskys, z is the redshift of the galaxy, and D_L is the luminosity distance of the galaxy in units of Megaparsecs.

$$\mathrm{L}_{850\mu\mathrm{m}}\ [\mathrm{erg\ s^{-1}\ Hz^{-1}}] = 1.19 \times 10^{27}\ \mathrm{S}_{850\mu\mathrm{m}}\ [\mathrm{Jy}] \times \left(\frac{\nu_{850\mu\mathrm{m}}}{\nu_{\mathrm{obs}}(1+z)}\right)^{3.8} \left(\frac{{D_L}^2\ [\mathrm{Mpc}]}{(1+z)}\right) \quad (4.2)$$

The SCUBA-2 data reduction process and the creation of the apertures used to measure the 850 μm fluxes are described in Smith et al. (in prep). The apertures are based on the initial Herschel SPIRE apertures, with modifications based on the growth curves from the 850 μm SCUBA-2 maps. For galaxies that are well-fit by a point-source, that flux is used instead of the aperture flux. A full list of the JINGLE galaxies and their properties are provided in the tables found in Appendix A (§ 4.8).

In this analysis, we remove galaxies with aperture fluxes that turn out to be negative. We also set a threshold for detected galaxies in the JINGLE maps at a signal to noise (S/N) level of 2 in the resulting flux value, which results in a total of 55 detected galaxies. Out of this detected sample, 15 galaxies have aperture flux measurements with a S/N ratio of between 2 and 3, and 9 out of those 15 galaxies have a peak S/N flux of greater than 3. Note that this is less than the S/N aperture threshold of 3 previously used in similar surveys such as the NGLS. However, improvements in the data-processing of JINGLE galaxies are ongoing and it is likely many of these galaxies will end up above the S/N aperture threshold. In addition, we will incorporate non-detections into our results as upper limits in the framework of survival analysis. This statistical tool is more fully described in Chapter 2 of this thesis.

4.4 Molecular Gas Masses Using CO $J = 2 - 1$ Data

The main method of measuring the molecular gas content of nearby galaxies has traditionally been through the use of the carbon monoxide (CO) molecule, which is a good tracer of the bulk molecular gas mass (Bolatto et al., 2013). The main transition used is the ground state CO $J = 1 - 0$ transition, but RxA3m is able to observe the CO $J = 2 - 1$ line at a frequency of 230 GHz.

We can convert the CO $J = 2 - 1$ luminosity to an equivalent CO $J = 1 - 0$ luminosity using an expected line ratio (R_{21}). The value of R_{21} adopted by the JINGLE collaboration is 0.8, between the value of ~ 0.5 for nearby star-forming disks (Rosolowsky et al., 2015) and a value of ~ 1 for starburst galaxies (Downes & Solomon, 1998). To determine the molecular gas masses for JINGLE galaxies, we use the following equation:

$$\mathrm{M}_{\mathrm{H}_2}\ [\mathrm{M}_\odot] = 1.073 \times 10^4\ d_L^2\ [\mathrm{Mpc}]\ \mathrm{S}_{\mathrm{CO}}\ [\mathrm{Jy\ km\ s^{-1}}] \times \left(\frac{X_{\mathrm{CO}}}{2 \times 10^{20}}\right)\left(\frac{\nu_0}{115.271\mathrm{GHz}}\right)^{-2}\left(\frac{\mathrm{f_{ap}}}{\mathrm{R}_{21}}\right) \quad (4.3)$$

The $\mathrm{M}_{\mathrm{H}_2}$ is the molecular hydrogen mass in units of solar mass, S_{CO} is the integrated line flux in units of Jansky kilometres per second, and ν_0 is the frequency in units of Gigahertz. $\mathrm{f_{ap}}$ is the aperture correction term, which we assume to be 1 for the JINGLE sample. In the redshift range of the JINGLE sample ($0.01 < z < 0.05$), most of the molecular gas can be observed within the JCMT RxA3m half power beam width of $\sim 22''$ at 230 GHz.

Figure 4.1 shows the correlation between these two methods of estimating molecular gas masses. For the galaxies in the JINGLE survey, the two methods provide similar estimates but with a large scatter in the relationship. A least

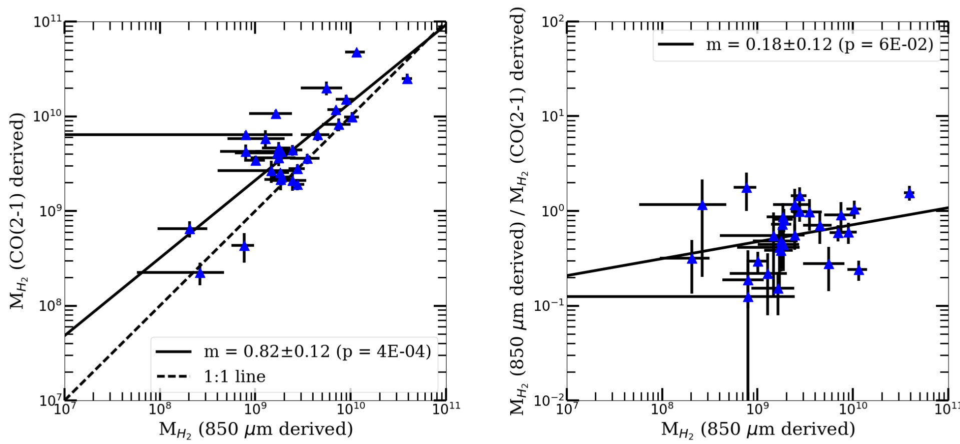

Figure 4.1 **Left:** Plot of the molecular gas mass derived from the CO $J = 2-1$ line vs. the molecular gas mass derived from the 850 μm flux. The 1:1 line (dashed line) and the least squares fit (solid line) to the points are included. The slope of the least squares fit and the p-value from the Pearson's correlation test are provided in the legend. The slope of the fitted line is 0.82 ± 0.12. It is possible that the 850 μm method may be underestimating the H_2 mass for galaxies with less molecular gas, but more CO $J = 2 - 1$ observations are needed to confirm this result. **Right:** Plot of the ratio of the molecular gas mass derived from the 850 μm to the CO $J = 2 - 1$ line vs. the molecular gas mass derived from the 850 μm flux. The measurements of the DR1 sample show a potential offset, but not a significant trend with molecular gas mass.

squares fit to the points gives a slope of 0.82 ± 0.12. The 850 μm method may be underestimating the H_2 mass for galaxies with less molecular gas, but we will need more galaxies with both 850 μm and CO $J = 2 - 1$ data to confirm this result. This possible trend may be attributed to variations in the dust-to-gas ratio and the increasing contributions to the 850 μm flux from the atomic gas. Once the final data reduction is completed and accurate dust masses found from the SED-fitting process, we will try to correlate these results to galaxy properties such as metallicity and the atomic gas to molecular gas fraction.

Since the total number of detected galaxies is higher for the 850μm data and their gas masses appear to be generally consistent with those derived from the CO $J = 2 - 1$ data, we will use the SCUBA-2 dataset for environmental analysis in the following sections. Although we have not performed additional calibration steps, since we are mainly considering trends and scaling relations in this analysis, our conclusions should not be affected by any potential offsets. Finally, this process assume a constant gas-to-dust ratio, so any observed trends should in theory also apply to the dust. We will not focus on the dust component as accurate dust mass estimates will be obtained after performing the full dust SED-fitting routine by members of the JINGLE team.

4.4.1 Supplementary Data

We also use other data collected by the JINGLE team, which will be made available in a public catalogue. We use the right ascension and declination co-ordinates from the database to match with the group catalogue discussed in Section 4.5. The cosmological parameters assumed for the JINGLE survey are as follows: matter density – $\Omega_m = 0.3$, dark energy density – $\Omega_\Lambda = 0.7$, and the Hubble constant – $H_0 = 70$ km s^{-1} Mpc^{-1}. The JINGLE survey also assumes a Chabrier Initial Mass Function (IMF) for the calculations of the star-formation rates and stellar masses (Chabrier, 2003). For this analysis, we use three main sets of supplementary data from the JINGLE catalogue, which are further described in the survey overview paper (Saintonge et al., in prep).

First, we use the stellar masses obtained from multi-wavelength spectral energy distribution (SED) fitting. The JINGLE galaxies use the Comprehensive Adjustable Aperture Photometry Routine (CAAPR) pipeline[1]. Full details about the use of this pipeline can be found in De Vis et al. (2017) and in the JINGLE overview paper (Saintonge et al., in prep). The fluxes are then incorporated into Multi-wavelength Analysis of Galaxy Physical Properties (MAGPHYS) models (da Cunha et al., 2008) to determine galaxy wide properties, such as the stellar mass and metallicity.

Second, we use the star formation rates derived from the CAAPR photometry and MAGPHYS SED fitting as described in the previous paragraph.

Finally, we use the available H I masses, which includes a total of 39 galaxies in the JINGLE DR1 galaxy sample. There are two main sources in the JINGLE master catalogue: the ALFALFA survey (Giovanelli et al., 2005) and the H I galaxy catalogue compiled by Springob et al. (2005). There are new observations from Arecibo for the remainder of the JINGLE galaxies (Smith et al., in prep), but the data were obtained in Spring 2017 and have not been reduced in time for this analysis. Individual errors have not been compiled in the catalogue, but we assume a 25% uncertainty on the H I flux density (Haynes et al., 2011).

[1] https://github.com/Stargrazer82301/CAAPR

4.5 Environmental Analysis

4.5.1 Tempel et al. (2014) Group Catalogue

We use the catalog from Tempel et al. (2014), which looks for groups and clusters in the dataset from the Sloan Digital Sky Survey (SDSS). We will use the term 'group' for these systems to simplify the terminology, but some of the more massive haloes may be more commonly referred to as clusters, such as the Coma Cluster. The group catalogue uses the DR10 release of the SDSS (Ahn et al., 2014), which covers $\sim 17.5\%$ of the sky. To identify groups, Tempel et al. (2014) used the Friends-of-Friends (FoF) algorithm to identify groups, a well-developed technique that is used by similar studies as the initial step for this type of analysis (e.g. Yang et al., 2007). We use the assumed JINGLE cosmology in this analysis, with $h = 0.7$ used for the parameters from the environment catalogue where applicable.

Since the SDSS is a flux-limited dataset, it will be missing faint objects at larger distances. As a result, Tempel et al. (2014) created a series of 8 different catalogues: a flux-limited catalogue and 7 volume-limited samples at varying absolute magnitude cuts (M_r) of -18.0, -18.5, -19.0, -19.5, -20.0, -20.5, and -21.0. The volume-limited sample with a magnitude cut of -18.0 corresponds to a limiting redshift of 0.045, while -21.0 correpsonds to a limiting redshift of 0.168 (Tempel et al., 2014). Since the JINGLE galaxies are at a moderate redshift range of $0.01 < z < 0.05$ and we are only looking at the environment of these galaxies, this analysis will use the full catalogue, in order to maximize the chances of matching the two datasets.

In total, we match 104 out of the 105 galaxies with SCUBA-2 measurements with the Tempel et al. (2014) catalogue. We require that the two catalogues matches are within 5" and a redshift difference of less than 1%. There is also an additional galaxy with RxA3m CO $J = 2 - 1$ observations, but no SCUBA-2 observation included in the Appendices. From the Tempel et al. (2014) group catalogue, two parameters are measured for the individual JINGLE galaxies:

- DEN1 - The normalized environmental density of the galaxy at various scales, where the 1 refers to 1 h^{-1} Mpc from the catalogue. The process of calculating this value is described fully in Tempel et al. (2012), where the luminosity density field is measured and then smoothed at various length scales. The local density field value at the galaxy's location is then calculated and normalized by the mean density. There are also DEN2, DEN4, and DEN8 for smoothing scales at 2, 4, and 8 h^{-1} Mpc respectively, but we do not use those parameters in our analysis.

- ZCMB - This is the redshift for the individual galaxies, corrected to the cosmic microwave background (CMB) rest frame. This is used to calculate the velocity of the individual galaxy with respect to the host group when combined with the CMB-corrected group redshift.

For the individual groups, we use 6 parameters from the Tempel et al. (2014) group catalogue:

- RAJ2000 + DEJ2000 - The right ascension and declination of the group centre. This is used to calculate the phase space location of an individual galaxy by measuring its projected distance to the group centre.

- NGAL [n] - The number of galaxies in the group, also known as richness or multiplicity.

- SIG.V [km s^{-1}] - The rms radial velocity dispersion for the group, estimated from the line of sight velocities of the member galaxies. This is used to normalize the velocity of an individual galaxy with respect to the velocity dispersion of the host group in the phase space analysis.

- MASS_NFW [h^{-1} $M_{\odot}$] - The mass of the halo using an estimate from the dynamical mass. The process of calculating this value is described fully in Tempel et al. (2014). The velocity dispersion of the group is measured and combined with a chosen density profile for the haloes, which in this case is the NFW profile (Navarro et al., 1997), to obtain a radius for the group. The velocity dispersion and the radius are combined together using the virial theorem to determine a dynamical mass. The catalogue contains masses for all groups, though this method is uncertain for groups with less than 10 members (Lee, 2017).

- RVIR [Mpc] - The virial radius of the group, obtained in the same procedure as the velocity dispersion and dynamical mass. This is used to normalize the projected distance of an individual galaxy from the group center in the phase space analysis.

- ZCMB - This is the redshift for the group, corrected to the CMB rest frame. This is used to calculate the velocity of an individual galaxy with respect to the velocity of the host group when combined with the CMB-corrected galaxy redshift.

We present some selected environment properties for the JINGLE galaxies in Appendix B (§ 4.9). For this analysis, we also match the COLD GASS sample to the Tempel et al. (2014) catalogue, finding matches for 271 out of 366 galaxies. The remaining COLD GASS galaxies are outside of the region of the sky studied in the group catalogue.

4.5.2 Dividing the Sample into Different Environments

We use the environment data to sub-divide the JINGLE sample. For the halo masses, we divide the galaxies into bins of host halo mass ranges of $< 10^{13}$, $10^{13} - 10^{14}$, and $> 10^{14}$ $M_{\odot}$, which we consider as the low density environment (isolated and poor-groups), medium density environment (rich groups), and high density environment (clusters). We also include galaxies not in a group to be in the low density environment bin. This classification is well-correlated with the Ngal categories of < 10, $10-99$, and > 100, which is the traditional method of defining isolated/poor groups, rich groups, and clusters. Figure 4.2 shows the rough equivalence between the two methods for classifying the galaxies in the JINGLE sample.

One caveat to the MASS_NFW parameter is their method of defining the halo mass. Tempel et al. (2014) first calculate the velocity dispersion of the group, then assume a chosen density profile to determine the radius, and finally use the virial theorem to calculate a dynamical mass. The method of determining the velocity dispersion for a group is uncertain for groups with less than 10 members (Lee, 2017) and so accurate masses should not be expected below that limit. Although masses are calculated for all the groups in the

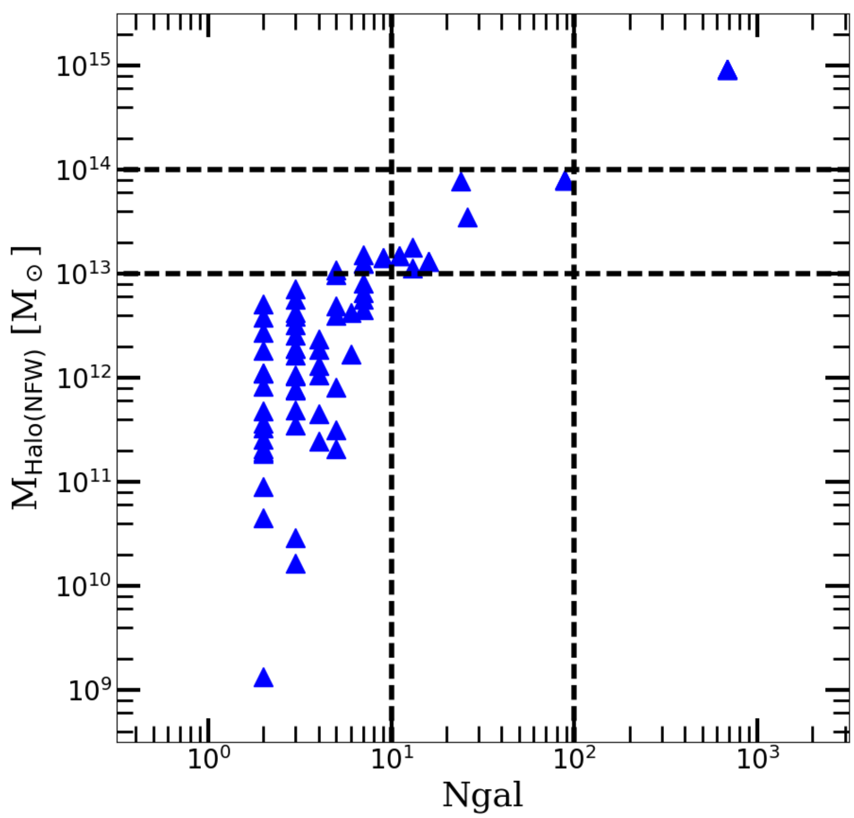

Figure 4.2 Plot of the number of galaxies in the group vs. group halo mass for the galaxies in the JINGLE sample. We select galaxies in bins of host halo masses of $< 10^{13}$, $10^{13} - 10^{14}$, and $> 10^{14}$ $M_\odot$. The bins for the number of group galaxies is set at < 10, $10 - 100$, and > 100. The two sets of boundaries are plotted with dashed lines. The plot shows that the two methods lead to similar classifications for most of the galaxies in JINGLE.

Tempel et al. (2014) catalogue, we will not use the masses for groups with less than 10 members in our linear fits. In our analysis with binned sub-samples, 10 members is also the dividing line between the low density environment (isolated/poor groups) and the medium density environment (rich group) bin, so incorrect mass estimates below the limit of 10 member galaxies should not be a significant factor.

Another method of classifying the halo is to use the normalized environment density as the parameter, which is a measurement of how many galaxies are within a certain distance. There are 4 different choices, which measure the galaxy density with smoothing scales of 1, 2, 4, and 8 h^{-1} Mpc. This is perhaps a more nuanced view of the environment, as there may be differences between galaxies closer to the group center and galaxies at the edge of the group. We use the density within 1 h^{-1} Mpc, as this is where we expect the strongest environmental signature to be found.

Finally, we can determine the position of an individual galaxy on a phase-space diagram, where we have velocity of the galaxy relative to the group centre (Δ) on the y-axis and the group-centric radius on the x-axis. We normalized both axes by dividing the velocity by the group velocity dispersion (σ) and the distance to the group centre by the group virial radius ($R_{\rm vir}$). We divide our sample into two regions in a similar fashion to the analysis performed by Muzzin et al. (2014) and Noble et al. (2016), where they create bins of equal number of galaxies in the $r \times v$ parameter. A plot of the JINGLE galaxies performed using this analysis is present in Figure 4.3. For the JINGLE galaxies, we divide the sample into two bins at $r \times v = 1$, which separates the sample

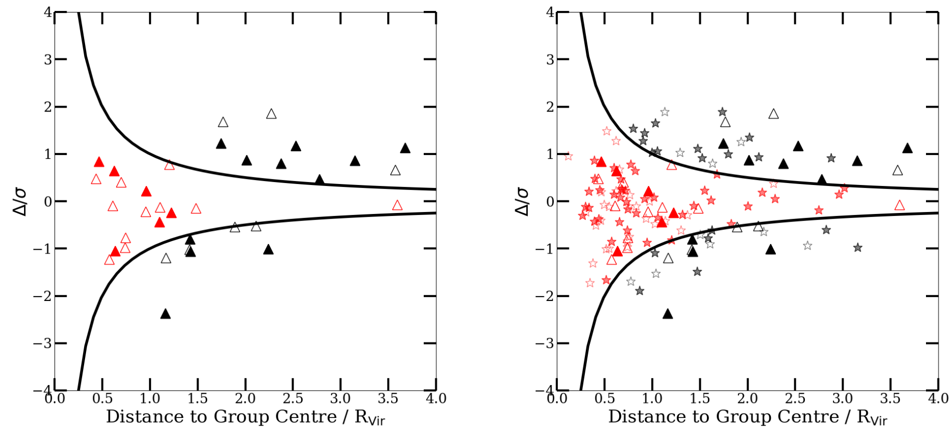

Figure 4.3 **Left:** Plot of the JINGLE sample in a phase-space diagram, where we plot the galaxy velocity relative to the group velocity (Δ) divided by the group's velocity dispersion (σ) vs. the group-centric radius divided by the the group's virial radius (R_{vir}). Solid triangles indicate galaxies in groups of more than 10, while open triangles indicate groups with 5 to 9 members. We can divide the JINGLE sample into two bins at $r \times v = 1$, as shown with the solid line, dividing recently infalling galaxies from an older population. **Right:** The COLD GASS galaxies are plotted, in solid and open star symbols using the same criteria as the JINGLE galaxies.

between those galaxies likely to be newly infalling objects and the older, more virialized population. This separation is also seen in the Millenium Simulation in Haines et al. (2012), which shows the inner region to be dominated by galaxies accreted earlier and therefore have felt the effects of environment to a larger extent. With the full sample and improvements in measuring the 850 μm flux, we should eventually be able to define many more regions used in these previous analyses, such as central, intermediate, recently accreted, infalling, and field.

4.6 Results and Discussion

4.6.1 Scaling Relations in the JINGLE Sample

The ISM properties of JINGLE galaxies are strongly affected by their stellar masses. In addition, due to selecting galaxies that lie on or slightly above the star-forming main sequence, their properties are also well-correlated with their star formation rate. Figure 4.4 presents plots of several galaxy properties with respect to their stellar mass. We also perform least squares fit to the detected points, as well as present the results from the Pearson's correlation test. Note that for the rest of this analysis, we will discuss significant correlations if the p-value is less than 0.05 and the absolute value of the slope is larger than the uncertainty. There is a negative correlation between the stellar mass and the specific star formation rate (SFR/M_*), the molecular gas fraction ($M(H_2)/M_*$) and the atomic gas fraction ($M(\text{H I})/M_*$). On the other hand, the H_2-to-H I ratio appears to be nearly independent of stellar mass, which suggest that environmental differences may be easiest to measure with that quantity.

In Figure 4.5, we overlay COLD GASS galaxies with detections in the appropriate parameter. The stellar mass range of the COLD GASS sample is smaller compared to the JINGLE sample, with no galaxies below 10^{10} $M_\odot$ in stellar mass. However, in the region where the two samples overlap, the galaxies appear to follow similar trends in their atomic gas and molecular gas fractions. One fortunate side-effect of the relatively shallow COLD GASS survey is that the galaxies with H_2 and H I detections are likely comparable to star-forming JINGLE sample.

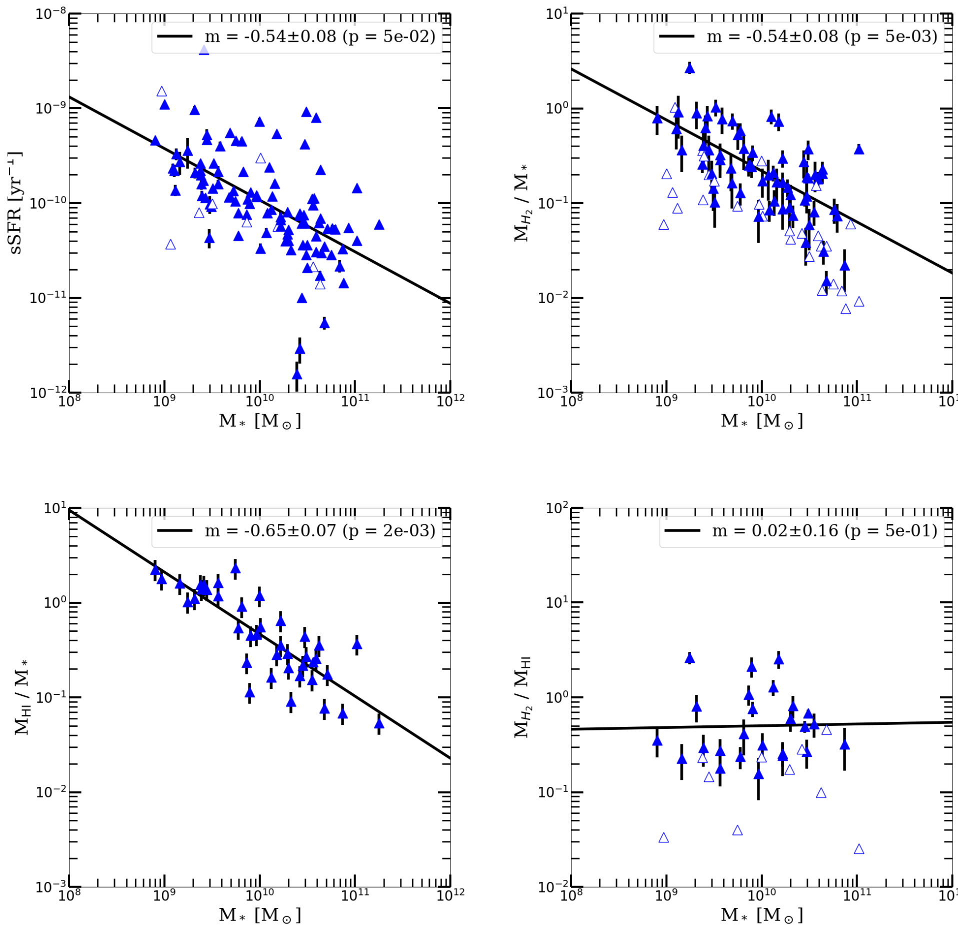

Figure 4.4 Plot of the correlation with stellar mass for selected JINGLE galaxy properties: sSFR (top left), molecular gas fraction (top right), atomic gas fraction (bottom left), and the H_2-to-H I ratio (bottom right). Filled triangles indicate JINGLE galaxy measurements, with associated error bars. Open triangles indicate values below the S/N threshold of 2. The slope of the least squares fits to the detected points and the p-values from the Pearson's correlation test are provided in the legend. There is a negative correlation in the specific star formation rate, atomic gas fraction, and molecular gas fraction with stellar mass, but the H_2-to-H I ratio appears to be nearly independent of stellar mass.

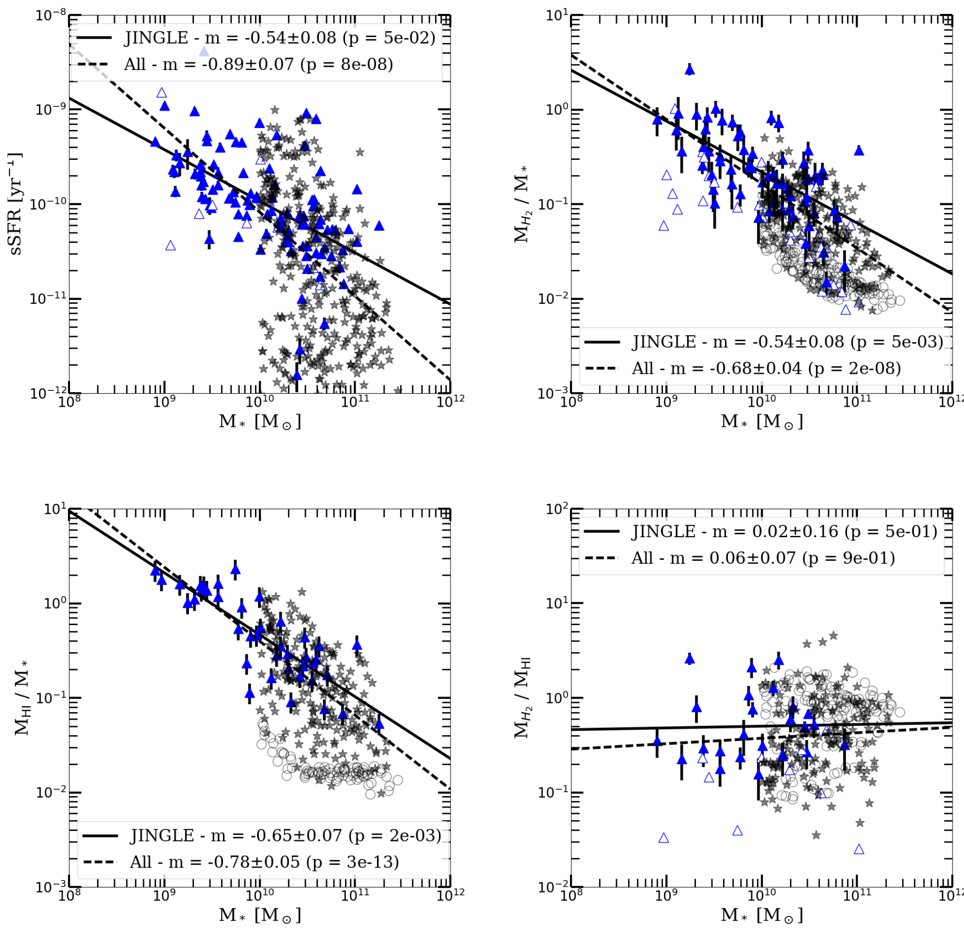

Figure 4.5 Plot of the correlation with stellar mass for selected JINGLE galaxy properties: sSFR (top left), molecular gas fraction (top right), atomic gas fraction (bottom left), and the H_2-to-H I ratio (bottom right). Filled triangles indicate JINGLE galaxy measurements, with associated error bars. Open triangles indicate values below the S/N threshold of 2. The COLD GASS (grey stars) galaxies are overlaid, as well as non-detections (grey circles). The slope of the least squares fit to the detected points and the p-values from the Pearson's correlation test are provided in the legend, including fits to the JINGLE points (solid line) and fits to the combined sample (dashed lines). In comparison to the previous figure, the main differences are in the wider range of galaxy sSFRs in the COLD GASS sample and a higher H_2-to-H I ratio for the COLD GASS sample.

The main difference between the two samples is in the wider range of galaxy sSFRs in the COLD GASS sample. This is due to the lack of gas-poor, low sSFR objects in the JINGLE sample, as a result of the Herschel selection criteria. The molecular gas fraction, atomic gas fraction, and the H_2-to-H I ratio appear to be consistent between the JINGLE and COLD GASS samples.

Next, we plot the star formation rate vs. the molecular gas mass for the JINGLE galaxies in Figure 4.6. The COLD GASS (grey stars) and JINGLE (triangles) samples follow a similar linear trend. The slope of the least squares fit to the detected galaxies in the JINGLE sample is close to unity, with a value of 0.84 ± 0.11. The slope of the fit to the combined sample is consistent with the JINGLE-only fit.

Finally, when we measure the molecular gas depletion times in Figure 4.7, there does not appear to be a significant trend with stellar mass for the JINGLE sample. There has been debate in the literature over whether the molecular gas gas depletion times are universal inside star-forming galaxies (Leroy et al., 2008; Bigiel et al., 2008) or if they can vary with galaxy properties, such as stellar mass (Saintonge et al., 2011b). At this moment, we do not find a significant trend with stellar mass for molecular gas depletion time in the JINGLE DR1 sample. When we add the COLD GASS sample, which includes many more galaxies at the high stellar mass end, there appears to be a positive correlation with the molecular gas depletion times. We will explore these important scaling relationships further once observation and data reduction for the full JINGLE sample is complete.

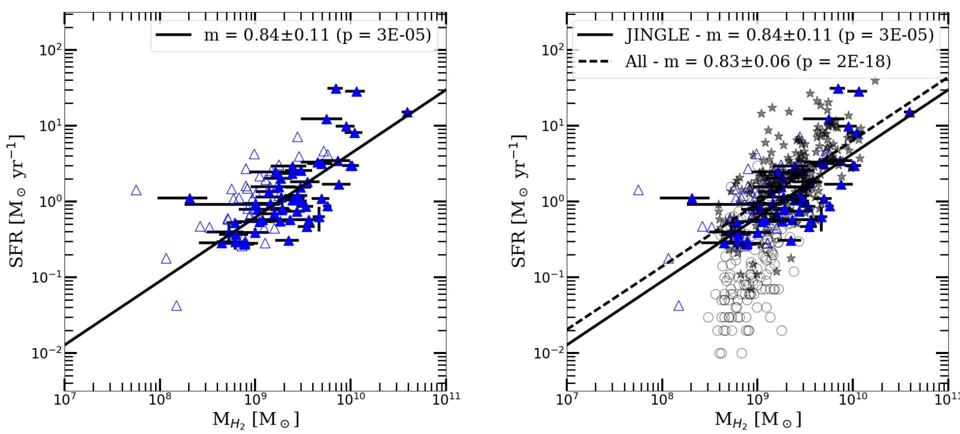

Figure 4.6 **Left:** Plot of the star formation rate vs. molecular gas for the JINGLE galaxies. Filled triangles indicate JINGLE measurements, along with the associated error bars, while open triangles indicate non-detections from our 850 μm S/N criteria. The slope of the least squares fit to the detected points and the p-value from the Pearson's correlation test are provided in the legend. The slope to the least squares fit (solid line) is 0.84 ± 0.11 and the Pearson test p-value of 3×10^{-5}. **Right:** The COLD GASS (grey stars) galaxies are overlaid, as well as non-detections (grey circles). The slope to the all detected galaxies (dashed line) is consistent with the JINGLE-only fit.

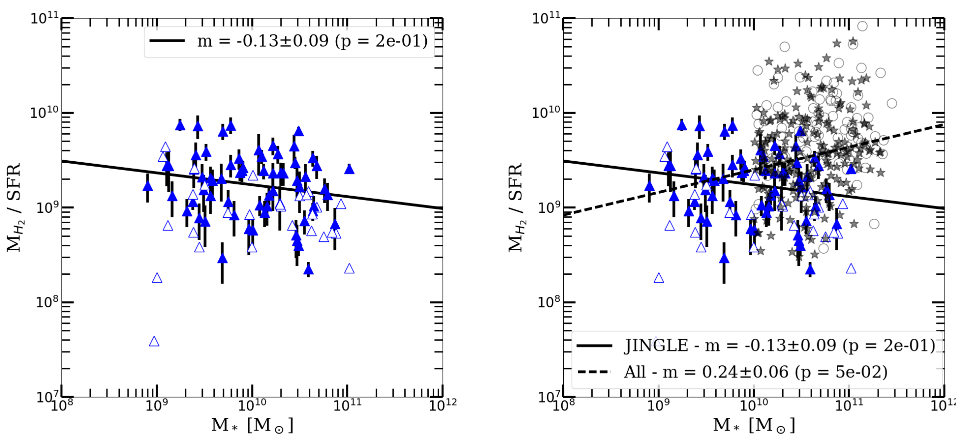

Figure 4.7 **Left:** Plot of the molecular gas depletion time (molecular gas mass divided by the star formation rate) vs. stellar mass for JINGLE galaxies. Filled triangles indicate JINGLE galaxy measurements, with associated error bars. Open triangles indicate values below the S/N threshold of 2. The slope of the least squares fit to the JINGLE galaxies (solid line) and the p-value from the Pearson's correlation test are provided in the legend. We do not see a significant trend with stellar mass. **Right:** The COLD GASS (grey stars) galaxies are overlaid, as well as non-detections (grey circles). The fit to all detected galaxies (dashed line) show an increase in the molecular gas depletion times for more massive galaxies.

4.6.2 Group Halo Masses

Next, we divide the JINGLE sample using the masses of their host haloes. As stated in the previous section, there is a strong correlation between the number of galaxies in a group and the group halo mass. As a result, we decide to use group halo mass as our main measurement of environment. We first measure if there are any trends with respect to stellar mass and the results are presented in Figure 4.8. We do not find any significant correlation between galaxy mass and host halo mass for the JINGLE sample or in the combined JINGLE and COLD GASS sample. Note that we only perform the least squares fit in the region where we are certain about the dynamical mass method ($> 10^{13}$ $M_{\odot}$).

Next, we plot the other galaxy parameters with respect to the group halo mass in Figure 4.9. Unfortunately, since most of our galaxies live in groups halos of less than 10^{13} $M_{\odot}$, we have a small number of galaxies and a limited dynamic range. The JINGLE sample does not show a significant trend in the molecular gas depletion time and molecular gas fraction with halo mass. For the combined sample, there is a positive correlation with the molecular gas fraction with the group halo mass, but given the large scatter in the points and the small number of galaxies, we will remain cautious until the final JINGLE dataset is included.

We also binned the JINGLE galaxies into three categories by their associated halo mass. We used the method of survival analysis, as presented in Mok et al. (2016), to incorporate upper limits for galaxies below our chosen S/N detection threshold. The results of performing this analysis on the binned

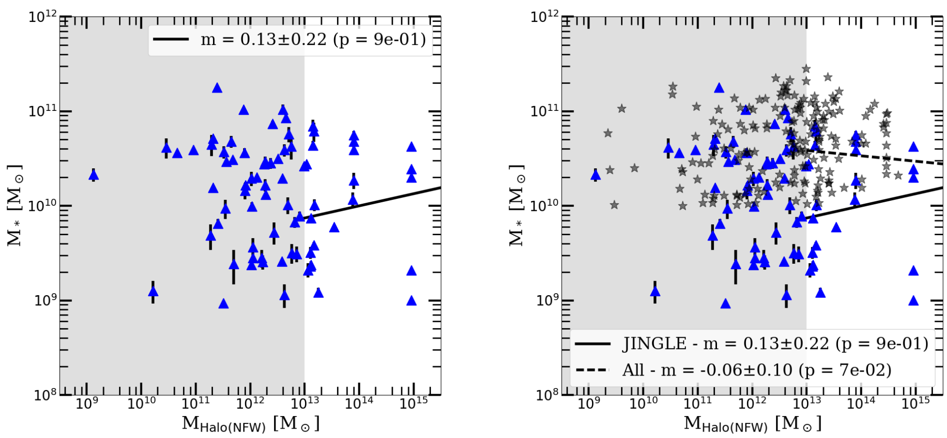

Figure 4.8 **Left:** Plot of the galaxy's stellar mass vs. group halo mass for the JINGLE galaxies. Filled triangles indicate JINGLE galaxies measurements, with associated error bars. The slope of the least squares fit to the JINGLE galaxies (solid line) and the p-value from the Pearson's correlation test are provided in the legend. We do not see a significant correlation between the two quantities. The shaded region indicate where halo masses are less certain. **Right:** The COLD GASS (grey stars) galaxies are overlaid, showing their higher stellar mass selection cutoff. The least squares fit to the combined sample (dashed line) does not show a significant trend.

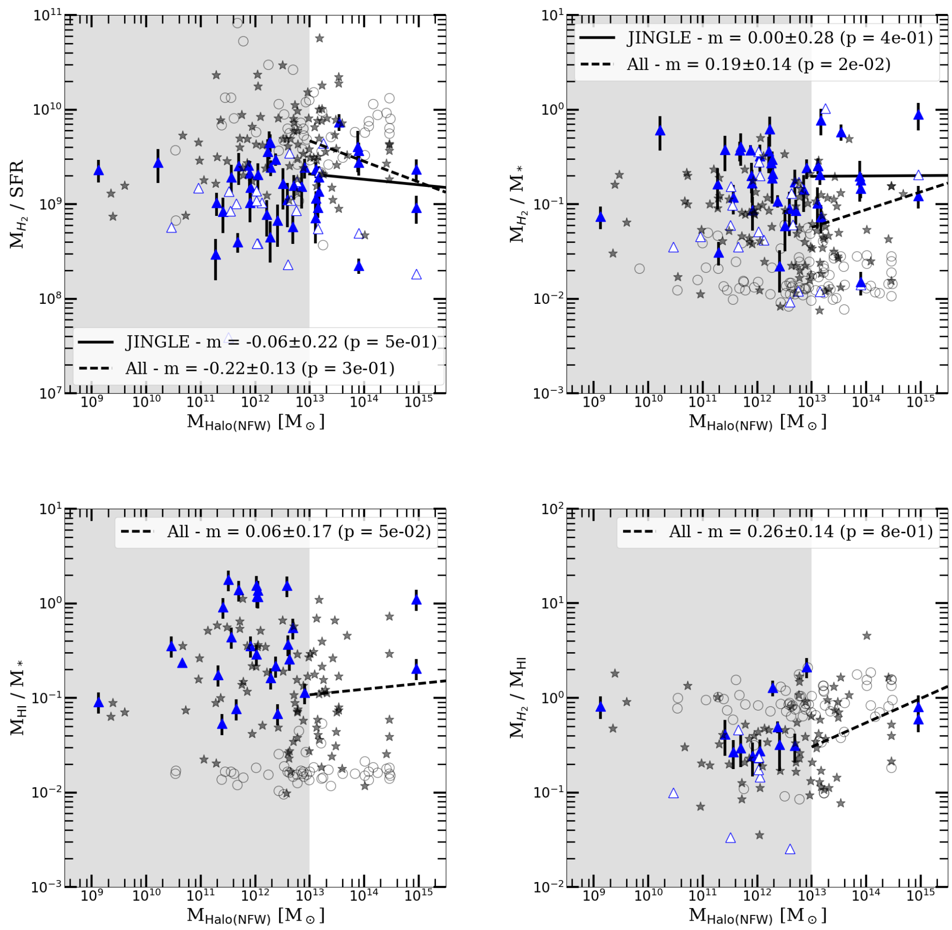

Figure 4.9 Plot of the correlation with halo mass for selected JINGLE galaxy properties, such as molecular gas depletion time (top left), molecular gas fraction (top right), atomic gas fraction (bottom left), and the H_2-to-H I fraction (bottom right). Filled triangles indicate JINGLE galaxies measurements, with associated error bars. Open triangles indicate values below the S/N threshold of 2. The shaded region indicate where halo masses are less certain. The COLD GASS (grey stars) galaxies are overlaid, as well as non-detections (grey circles). The slopes of the least squares fit to the detected points and the p-values from the Pearson's correlation test are provided in the legend, including fits to the JINGLE galaxies (solid line) and fits to the combined sample (dashed line). For H I measurements, we perform the fit on all galaxies only, due to a lack of JINGLE galaxies in the valid halo mass range.

Table 4.1 Properties of JINGLE Galaxies Subsamples, Divided by Host Halo Mass

	LD	MD	HD	LD/MD	LD/HD	MD/HD
Number	82	17	5	-	-	-
log H_2	9.14 ± 0.04	9.12 ± 0.12	8.97 ± 0.02	0.95	0.34	0.20
log H_2/M_*	-0.91 ± 0.06	-1.07 ± 0.14	-1.09 ± 0.13	0.46	0.90	0.71
log H_2/SFR	9.03 ± 0.04	9.11 ± 0.10	8.82 ± 0.07	0.61	0.44	0.45
log H_2/H I	-0.48 ± 0.05	-0.16 ± 0.04	-0.16 ± 0.04	0.38	0.38	1

Note: LD indicate galaxies with host halo mass of $< 10^{13}$ $M_\odot$, MD indicate host halo masses of $10^{13} - 10^{14}$ $M_\odot$, and HD indicate host halo masses of $> 10^{14}$ $M_\odot$.
Note: The last three columns are the p-values from performing the log-rank tests of the two populations.

galaxy sample is presented in Table 4.1. Due to the small number of galaxies, the statistical tests also show no significant differences between the three populations.

4.6.3 Environment Density at 1 h^{-1} Mpc

Next, we look for trends in the JINGLE galaxy properties with the normalized large scale environment density at 1 h^{-1} Mpc. This measurement provides more information than the host halo mass, as we would expect galaxies near the group center to have different properties than those living further out. In addition, since there are no constraints in defining this quantity, such as the threshold of 10 galaxies or more for reliable dynamical masses, we will have better statistics than the other two measures of environmental effect.

We first measure the correlation of stellar mass with the environment density in Figure 4.10. There is a positive correlation between the two parameters for the combined sample, as more massive galaxies have more neighbours on av-

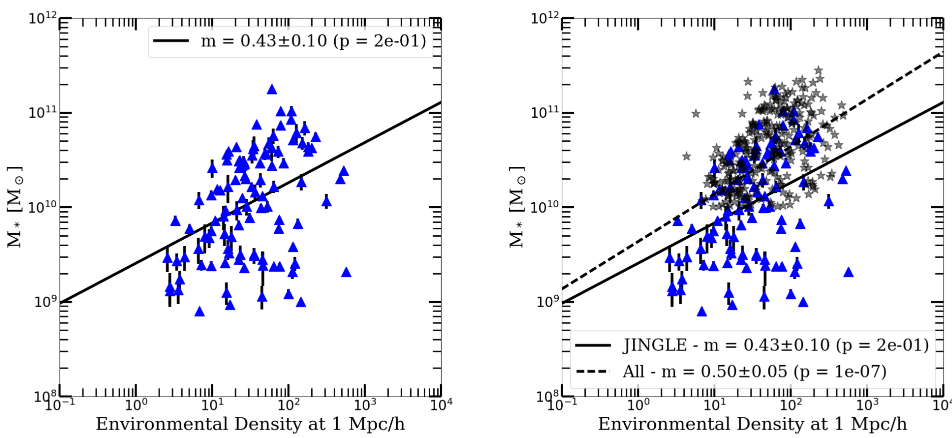

Figure 4.10 **Left:** Plot of the galaxy's stellar mass vs. environment density at 1 Mpc h^{-1}. Filled triangles indicate JINGLE galaxies, with the associated error bars. The slope of the least squares fit to the JINGLE galaxies (solid line) and the p-value from the Pearson's correlation test are provided in the legend. **Right:** The COLD GASS (grey stars) galaxies are overlaid, including a least squares fit to the combined sample (dashed line). For the combined sample, there is a positive correlation between stellar mass and environment density.

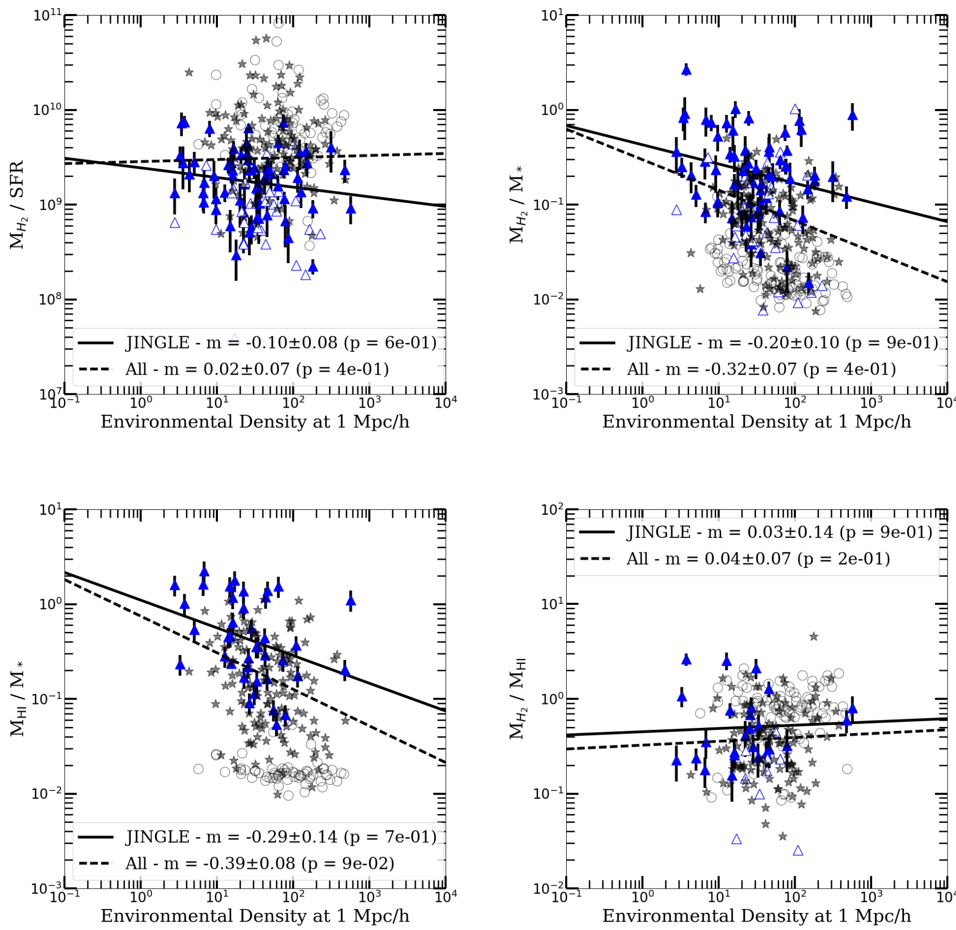

Figure 4.11 Plot of the correlation with halo mass for selected JINGLE galaxy properties: molecular gas depletion time (top left), molecular gas fraction (top right), atomic gas fraction (bottom left), and the H_2-to-H I ratio (bottom right). Filled triangles indicate JINGLE galaxies measurements, with associated error bars. Open triangles indicate values below the S/N threshold of 2. The COLD GASS (grey stars) galaxies are overlaid, as well as non-detections (grey circles). The slopes of the least squares fit to the detected points and the p-values from the Pearson's correlation test are provided in the legend, including fits to the JINGLE galaxies (solid line) and fits to the combined sample (dashed line). None of these correlations are statistically significant, according to the Pearson test.

erage. This is in agreement with previous observations of the nearby Universe, since more massive galaxies tend to live inside overdense regions (Blanton & Moustakas, 2009).

For the other galaxy properties presented in Figure 4.11, we find hints of a negative correlation between the atomic gas fraction and environmental density in the combined sample, though the Pearson correlation test indicates that it is not significant at this moment. This is also the case for the molecular gas fraction. Unfortunately, there do not appear to be any significant trends in the H_2-to-H I ratio and other parameters with the environmental density parameter.

4.6.4 Phase Space Analysis

We plot the galaxy properties against the $r \times v$ parameter, in the same fashion to past analysis from Noble et al. (2016). We include only galaxies in groups containing at least 10 members, such as in Figure 4.3. Unfortunately, as with the plots made with the host halo mass, there were only 2 H I observations for JINGLE galaxies which meet this criteria. This means that we cannot perform the same analysis on the atomic gas properties as performed for the other two environmental parameter.

Our results are presented in Figure 4.12. Due to in part to the small number of galaxies from JINGLE that live in groups of 10 or more, we do not find any significant environmental trends with this environmental parameter. Using the combined sample, there is a statistically significant correlation between molecular gas fraction and the $r \times v$ parameter. We hope to populate this plot

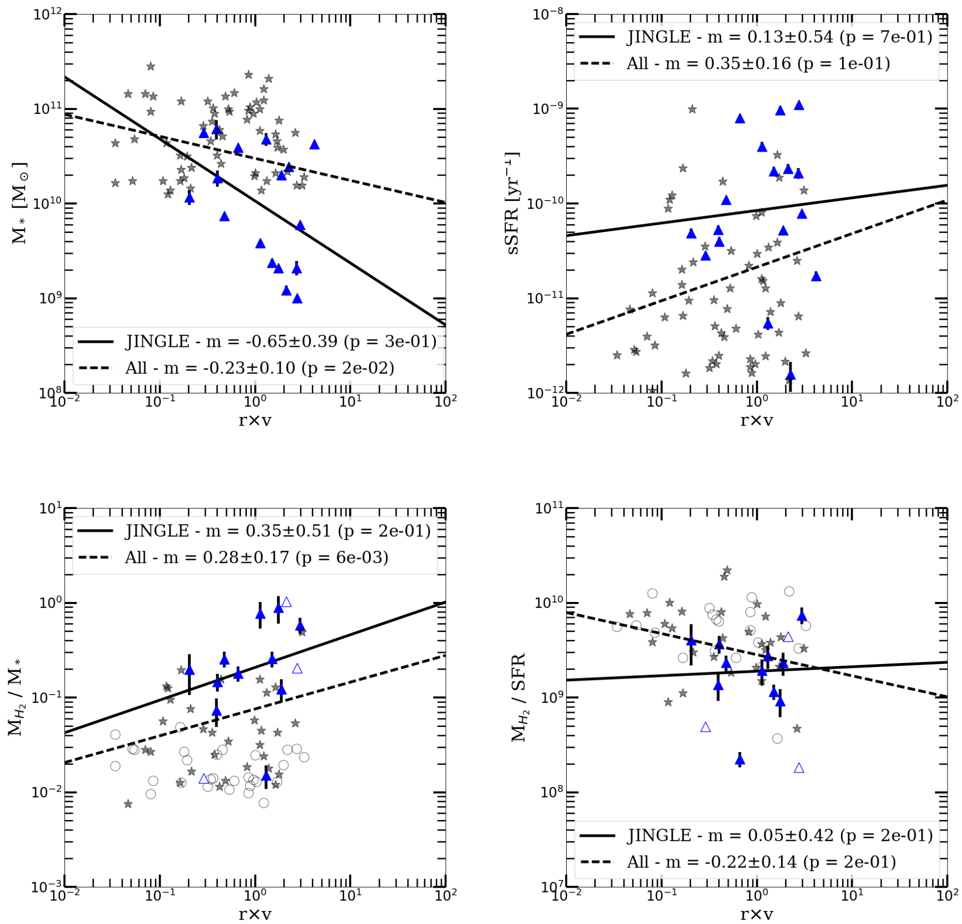

Figure 4.12 Plot of the correlation with $r \times v$ for selected JINGLE galaxy properties, such as stellar mass (top left), sSFR (top right), molecular gas fraction (bottom left), and the molecular gas depletion time (bottom right). Filled triangles indicate JINGLE galaxies measurements, with associated error bars. Open triangles indicate values below the S/N threshold of 2. The COLD GASS (grey stars) galaxies are overlaid, as well as non-detections (grey circles). The slopes of the least squares fit to the detected points and the p-values from the Pearson's correlation test are provided in the legend, including fits to the JINGLE galaxies (solid line) and fits to the combined sample (dashed line).

with more data-points once the full sample is achieved and determine these environmental variations for JINGLE galaxies.

4.7 Conclusions

We use a sample of gas-rich, star-forming galaxies from the JINGLE survey to analyze the variation of their star-forming and ISM properties with environment. In this analysis, we use the DR1 release from the initial set of 105 galaxies with SCUBA-2 and 35 with RxA3m measurements (Saintonge et al., in prep, Xiao et al., in prep). We perform an initial analysis of their star-formation and ISM properties and compare them to the results from the COLD GASS survey.

- We find a strong correlation between the molecular gas estimates obtained from the 850 μm and the CO $J = 2 - 1$ data. This result shows that the 850 μm dust continuum emission may be a good tracer of the molecular gas inside JINGLE galaxies.

- We find an almost linear relationship between star formation rate and molecular gas mass. For the JINGLE sample, we also find no significant correlation with stellar mass for the molecular gas depletion time and the H_2-to-H I ratio, whereas the sSFR, molecular gas fraction, and atomic gas fraction are strongly correlated with the stellar mass. This suggests that the molecular gas depletion time and the H_2-to-H I ratio may be ideal indicators for environmental effects in this sample of galaxies.

- We do not find any significant variations using environmental parameters such as the host halo mass, the local environment density, and location in phase-space for the JINGLE sample using the DR1 release.

In this work, we performed initial analysis on the star formation, atomic gas, and molecular gas properties of JINGLE galaxies. With this framework in place, we can quickly incorporate the data from the remainder of the survey and measure any environmental variations with improved statistics. On the other hand, the current lack of significant observed differences for our sample of JINGLE galaxies may indicate that galaxies on the star-forming main sequence have similar properties across a range of environments, such as in other observations of the star-formation and ISM properties for these galaxies (e.g Peng et al., 2010; Genzel et al., 2010).

In the future, we will have Arecibo H I observations for all of the galaxies in the JINGLE sample. The H_2-to-H I ratio appears to be a promising environmental indicator, given the strong variations found in the NGLS (Mok et al., 2016), the Herschel Virgo Survey (Corbelli et al., 2012), and the Herschel Reference Survey (Boselli et al., 2014). The use of the H I data will be instrumental, given the current lack of atomic gas data in the environmental analysis.

4.8 Appendix A - List of JINGLE Galaxies and Their Properties

Table 4.2 General Properties of JINGLE Galaxies

SDSS (ID)	d_L (Mpc)	SFR ($M_\odot$ yr^{-1})	M_* (log $M_\odot$)	$M(H_2)_{850}$ (log $M_\odot$)	P.S. (-)	$M(H_2)_{CO}$ (log $M_\odot$)	M(H I) (log $M_\odot$)
J084532.01+011736.2	194.7	2.58 ± 0.22	9.75 ± 0.05	9.48 ± 0.14	0	-	-
J084648.77+001812.6	127.8	0.58 ± 0.05	9.75 ± 0.17	8.72 ± 0.37	0	-	10.11
J084742.49+004056.0	201.2	0.13 ± 0.03	9.47 ± 0.13	-	1	-	-
J085043.08+012102.4	188.4	2.77 ± 0.18	10.71 ± 0.01	-	0	-	9.96
J085747.31-001159.8	123.4	2.33 ± 0.19	10.16 ± 0.09	9.38 ± 0.17	0	-	-
J090045.90-002937.2	180.2	0.81 ± 0.11	10.30 ± 0.02	8.92 ± 0.25	1	-	-
J091750.80-001642.5	75.9	1.02 ± 0.03	10.45 ± 0.05	9.48 ± 0.06	0	-	9.79
J092143.23+024127.1	107.3	0.63 ± 0.22	9.24 ± 0.09	9.67 ± 0.06	0	-	9.25
J113725.46-014714.3	208.5	0.60 ± 0.33	10.63 ± 0.12	8.71 ± 0.49	1	-	-
J114103.60+014331.7	179.3	3.95 ± 0.30	10.55 ± 0.08	9.46 ± 0.12	1	-	9.74
J114253.92+000942.7	80.2	1.44 ± 0.96	8.97 ± 0.01	7.75 ± 0.71	1	-	9.22
J114359.62+002540.7	125.5	10.76 ± 0.06	9.41 ± 0.01	-	0	-	9.60
J114522.07-013354.5	124.1	0.44 ± 0.06	9.32 ± 0.07	-	1	-	-
J115104.55+001454.2	208.5	0.92 ± 0.07	10.29 ± 0.08	9.00 ± 0.36	1	-	9.75
J115705.93+010731.8	174.5	10.64 ± 0.06	11.25 ± 0.00	-	0	-	9.98
J115723.03+002913.9	210.0	3.44 ± 0.30	10.56 ± 0.05	9.86 ± 0.15	0	-	-
J115736.61+010826.7	159.3	0.66 ± 0.00	10.50 ± 0.00	8.94 ± 0.41	0	-	-
J115846.24-012757.0	93.0	0.47 ± 0.00	9.78 ± 0.00	9.54 ± 0.09	0	-	-
J120018.00+001741.9	89.9	0.69 ± 0.04	10.33 ± 0.07	9.20 ± 0.12	0	-	9.29
J120446.29-000055.3	178.5	0.30 ± 0.04	9.39 ± 0.06	8.89 ± 0.28	1	-	-
J120803.96+004151.2	85.5	0.37 ± 0.00	8.90 ± 0.00	8.80 ± 0.15	0	-	9.25
J121017.87-003104.4	153.3	1.09 ± 0.03	10.88 ± 0.00	8.77 ± 1.15	0	-	-
J121520.15-002352.9	90.5	0.28 ± 0.04	9.10 ± 0.12	8.89 ± 0.17	0	-	-
J121552.50+002402.5	91.6	0.87 ± 0.07	10.49 ± 0.05	9.75 ± 0.04	0	-	9.92
J121948.26-005231.6	174.7	3.14 ± 0.27	10.76 ± 0.08	9.69 ± 0.13	0	-	-
J122337.49-002821.3	111.5	0.86 ± 0.00	9.52 ± 0.00	9.53 ± 0.09	0	-	-
J125440.02+322201.2	105.4	0.34 ± 0.04	10.01 ± 0.06	8.87 ± 0.26	0	-	-
J125453.68+282501.1	107.4	0.08 ± 0.02	10.42 ± 0.03	-	0	-	-
J125606.09+274041.1	71.5	1.11 ± 0.04	9.00 ± 0.01	8.31 ± 0.23	1	8.81 ± 0.08	-
J125610.97+280947.4	127.0	0.95 ± 0.07	10.08 ± 0.09	9.00 ± 0.10	1	9.54 ± 0.05	-
J125809.22+284230.8	110.8	1.05 ± 0.01	10.30 ± 0.01	9.39 ± 0.12	0	9.64 ± 0.06	9.61
J125818.23+290743.6	115.0	0.74 ± 0.08	10.63 ± 0.01	-	0	9.10 ± 0.12	-
J125837.28+271035.8	111.7	2.00 ± 0.17	9.32 ± 0.02	9.27 ± 0.14	0	9.33 ± 0.10	9.36
J125902.07+280656.3	137.8	2.70 ± 0.11	9.69 ± 0.13	8.90 ± 0.20	1	9.63 ± 0.08	-
J130125.07+284038.0	127.6	1.57 ± 0.10	10.29 ± 0.02	9.25 ± 0.21	0	9.56 ± 0.08	-
J130305.93+263152.0	83.1	0.27 ± 0.02	9.78 ± 0.04	8.88 ± 0.11	0	8.64 ± 0.15	9.51
J130316.24+280149.4	88.4	0.04 ± 0.01	10.39 ± 0.03	-	0	-	-

For Point Source column, 1 indicates the use of the point-source method and 0 indicates aperture method for SCUBA-2 flux measurements.

Table 4.3 General Properties of JINGLE Galaxies (continued)

SDSS (ID)	d_L (Mpc)	SFR ($M_\odot$ yr^{-1})	M_* (log $M_\odot$)	M(H_2)$_{850}$ (log $M_\odot$)	P.S. (-)	M(H_2)$_{CO}$ (log $M_\odot$)	M(H I) (log $M_\odot$)
J130329.08+263301.7	96.3	0.78 ± 1.04	10.56 ± 0.00	-	0	9.47 ± 0.06	9.94
J130428.23+264019.0	158.2	2.58 ± 0.25	10.62 ± 0.11	9.17 ± 0.31	0	9.43 ± 0.11	10.17
J130615.12+252737.9	105.4	3.07 ± 2.03	10.01 ± 0.09	9.25 ± 0.15	0	9.66 ± 0.07	9.75
J130636.39+275222.6	91.1	1.13 ± 0.06	10.12 ± 0.02	9.44 ± 0.08	0	9.45 ± 0.05	9.33
J130713.20+280249.0	106.2	0.77 ± 0.02	9.89 ± 0.05	9.27 ± 0.10	0	9.36 ± 0.06	8.95
J130801.65+264555.3	149.7	1.96 ± 0.05	10.42 ± 0.04	9.11 ± 0.26	0	9.77 ± 0.10	9.65
J130802.57+271840.0	85.2	0.40 ± 0.11	9.16 ± 0.17	8.72 ± 0.18	0	-	9.37
J130851.54+283745.4	99.0	0.46 ± 0.02	9.51 ± 0.06	8.52 ± 0.20	1	-	-
J130855.07+290226.7	137.6	1.19 ± 0.19	10.22 ± 0.14	9.44 ± 0.12	0	-	10.03
J130945.77+283716.3	98.6	0.18 ± 1.00	9.36 ± -0.00	-	0	8.95 ± 0.08	-
J131047.64+294235.6	92.3	1.05 ± 0.07	9.91 ± 0.13	9.44 ± 0.08	0	9.28 ± 0.06	9.56
J131101.71+293442.0	105.8	2.44 ± 0.03	10.87 ± 0.03	9.21 ± 0.21	0	10.03 ± 0.03	9.71
J131239.04+340354.5	149.6	1.54 ± 0.16	9.58 ± 0.03	9.47 ± 0.13	0	-	-
J131258.27+311531.0	88.6	0.79 ± 0.11	9.56 ± 0.14	9.02 ± 0.16	0	-	9.77
J131313.45+335903.9	154.5	3.29 ± 0.30	10.79 ± 0.10	9.65 ± 0.14	0	9.81 ± 0.06	-
J131508.21+302413.5	100.9	1.14 ± 0.00	10.50 ± 0.00	9.27 ± 0.20	0	9.63 ± 0.05	-
J131526.03+330926.0	70.4	0.18 ± 0.02	9.12 ± 0.12	8.06 ± 0.54	0	-	-
J131551.16+263320.4	168.6	1.59 ± 0.04	10.13 ± 0.05	9.15 ± 0.13	1	-	-
J131615.95+301552.2	218.6	12.36 ± 0.78	10.47 ± 0.05	9.75 ± 0.20	0	10.30 ± 0.07	-
J131620.53+304042.0	82.1	0.82 ± 0.00	9.87 ± 0.00	9.28 ± 0.08	0	-	-
J131721.28+310334.1	80.7	0.53 ± 0.05	9.38 ± 0.04	8.79 ± 0.08	1	-	-
J131804.10+335118.2	125.7	0.31 ± 0.03	9.43 ± 0.09	9.35 ± 0.12	0	-	-
J131958.31+281449.3	98.9	0.89 ± 1.05	10.19 ± 0.00	-	0	9.45 ± 0.05	-
J131958.56+340209.8	127.5	0.29 ± 0.06	9.48 ± 0.13	8.79 ± 0.16	1	-	-
J132014.23+312132.1	206.2	0.57 ± 0.07	10.07 ± 0.08	9.36 ± 0.20	0	-	-
J132035.40+340821.7	100.5	28.64 ± 0.33	10.49 ± 0.01	10.06 ± 0.10	0	10.68 ± 0.02	-
J132115.52+333732.0	171.4	1.31 ± 0.14	9.45 ± 0.09	9.01 ± 0.18	1	-	-
J132122.24+255703.6	146.9	1.13 ± 0.05	9.97 ± 0.05	8.83 ± 0.21	1	-	9.63
J132134.91+261816.8	71.7	0.55 ± 0.03	9.86 ± 0.05	9.26 ± 0.10	0	9.40 ± 0.04	9.23
J132151.16+322612.6	150.6	1.09 ± 0.13	9.97 ± 0.10	8.96 ± 0.35	0	-	-
J132251.07+314934.3	77.4	0.48 ± 0.02	9.38 ± 0.05	8.42 ± 0.34	0	8.35 ± 0.12	-
J132320.14+320349.0	72.5	0.29 ± 0.03	9.49 ± 0.08	8.65 ± 0.18	0	-	-
J132359.95+305556.7	97.1	0.28 ± 0.02	10.44 ± 0.01	-	0	-	-
J132443.68+323225.0	175.5	9.82 ± 0.34	10.64 ± 0.05	9.95 ± 0.10	0	10.18 ± 0.05	-
J132509.71+320051.9	177.6	2.17 ± 0.10	10.46 ± 0.01	9.05 ± 0.19	1	-	-
J132515.15+324016.1	175.8	1.50 ± 0.22	10.84 ± 0.08	8.92 ± 0.84	0	-	-

For Point Source column, 1 indicates the use of the point-source method and 0 indicates aperture method for SCUBA-2 flux measurements.

Table 4.4 General Properties of JINGLE Galaxies (continued)

SDSS (ID)	d_L (Mpc)	SFR ($M_\odot$ yr^{-1})	M_* (log $M_\odot$)	M(H_2)$_{850}$ (log $M_\odot$)	P.S. (-)	M(H_2)$_{CO}$ (log $M_\odot$)	M(H I) (log $M_\odot$)
J132609.41+264612.2	163.6	0.39 ± 0.05	9.39 ± 0.17	9.00 ± 0.16	1	-	9.53
J132638.85+270223.4	101.4	0.58 ± 0.06	9.56 ± 0.11	9.07 ± 0.14	0	-	9.63
J132643.48+303024.0	102.9	0.46 ± 1.07	9.86 ± 0.00	-	0	8.81 ± 0.13	-
J132731.45+342008.2	156.8	0.29 ± 0.03	9.09 ± 0.05	9.10 ± 0.25	0	-	-
J132838.16+333618.3	114.7	2.05 ± 0.11	10.42 ± 0.10	-	0	-	-
J132856.70+325244.0	112.0	3.00 ± 0.02	10.10 ± 0.01	10.02 ± 0.08	0	9.99 ± 0.06	-
J133213.68+265659.9	155.2	1.69 ± 0.00	10.44 ± 0.00	9.87 ± 0.14	0	9.92 ± 0.07	-
J133306.57+330903.7	108.9	1.45 ± 0.03	9.83 ± 0.06	-	0	-	-
J133316.29+343213.2	106.2	1.61 ± 0.08	10.75 ± 0.04	8.90 ± 0.91	0	9.80 ± 0.04	-
J133451.23+340319.8	109.5	0.74 ± 0.07	10.27 ± 0.09	9.44 ± 0.09	0	-	-
J133457.27+340238.7	103.1	31.05 ± 0.18	10.59 ± 0.01	9.84 ± 0.08	0	10.07 ± 0.03	-
J133538.40+255230.9	111.9	0.95 ± 0.05	10.22 ± 0.03	9.16 ± 0.17	0	-	9.77
J133619.63+332524.3	108.8	0.26 ± 0.04	10.68 ± 0.07	8.86 ± 0.12	1	-	-
J133931.82+312657.8	159.7	0.04 ± 0.03	9.06 ± 0.12	8.17 ± 0.98	1	-	-
J133933.35+295949.4	151.5	1.75 ± 0.03	10.59 ± 0.07	-	0	-	10.00
J133944.15+274635.2	123.4	2.93 ± 0.25	9.81 ± 0.05	9.39 ± 0.18	0	9.32 ± 0.09	9.77
J134017.95+262058.3	124.3	1.81 ± 0.01	10.47 ± 0.01	9.54 ± 0.15	0	9.55 ± 0.05	10.12
J134018.24+320911.2	112.6	0.71 ± 0.02	9.72 ± 0.11	-	0	-	-
J134113.58+302327.4	176.5	0.44 ± 0.08	9.41 ± 0.07	9.20 ± 0.15	1	-	-
J134145.21+270016.9	126.7	1.67 ± 0.12	10.68 ± 0.06	9.23 ± 0.28	0	9.61 ± 0.06	9.57
J134229.72+341303.4	153.0	0.57 ± 0.05	9.69 ± 0.15	9.56 ± 0.08	0	-	-
J134308.83+302015.8	152.7	15.21 ± 0.00	11.02 ± 0.00	10.59 ± 0.05	0	10.40 ± 0.05	-
J141330.00+001109.0	112.4	0.55 ± 0.02	9.68 ± 0.10	9.04 ± 0.19	0	-	-
J141605.26-011537.3	221.7	4.70 ± 0.14	10.93 ± 0.05	9.71 ± 0.38	0	-	-
J141628.95-004437.9	216.5	4.19 ± 0.05	10.57 ± 0.07	9.76 ± 0.23	0	-	-
J141658.36+013825.5	109.4	1.47 ± 0.22	9.45 ± 0.02	8.75 ± 0.37	0	-	9.58
J142227.60+000332.5	138.9	8.17 ± 0.14	10.18 ± 0.02	10.04 ± 0.09	0	-	9.63
J142433.17+011038.3	171.0	4.24 ± 0.15	11.02 ± 0.05	8.99 ± 0.99	0	-	10.58
J142653.06+005746.3	114.3	0.63 ± 0.00	9.38 ± 0.00	8.94 ± 0.25	0	-	9.57
J143042.33+015253.2	148.5	7.19 ± 0.70	10.00 ± 0.04	9.44 ± 0.25	0	-	10.07
J143643.42-003401.3	162.9	0.31 ± 0.25	9.50 ± 0.10	8.73 ± 0.29	1	-	-
J143816.50-002059.0	162.5	1.34 ± 0.11	10.65 ± 0.11	9.14 ± 0.12	1	-	-
J143842.98-000027.8	148.0	1.19 ± 0.01	10.59 ± 0.00	9.25 ± 1.03	0	-	-
J144256.63-004839.0	199.3	0.44 ± 0.06	9.13 ± 0.13	9.09 ± 0.21	1	-	-
J144307.78+010600.0	148.6	1.10 ± 0.09	10.22 ± 0.07	9.69 ± 0.09	0	-	-
J144322.25+010553.2	168.1	3.00 ± 0.00	10.64 ± 0.00	10.00 ± 0.08	0	-	-

For Point Source column, 1 indicates the use of the point-source method and 0 indicates aperture method for SCUBA-2 flux measurements.

4.9 Appendix B - List of JINGLE Galaxies and Their Environment

Table 4.5 Environmental Properties of JINGLE Galaxies

SDSS (ID)	Ngal (Num)	M_{halo} (log $M_{\odot}$)	Env. Den. at 1 h^{-1} Mpc (-)	R (Mpc)	R/R_{vir} (-)	Δ/v_{vir} (-)
J084532.01+011736.2	1	-	9.66	-	-	-
J084742.49+004056.0	1	-	2.58	-	-	-
J085043.08+012102.4	5	11.52	113.87	0.1	1.77	1.68
J085747.31-001159.8	5	12.11	36.67	0.2	0.74	-0.77
J090045.90-002937.2	4	12.33	27.52	0.2	1.48	1.15
J091750.80-001642.5	4	12.59	25.54	0.3	2.38	1.46
J092143.23+024127.1	1	-	3.73	-	-	-
J113725.46-014714.3	7	12.97	60.69	0.9	1.89	-0.54
J114103.60+014331.7	1	-	33.30	-	-	-
J114253.92+000942.7	5	11.71	17.05	0.2	0.61	-0.09
J114359.62+002540.7	2	12.59	14.71	0.1	0.73	0.73
J114522.07-013354.5	13	13.27	113.14	0.4	3.15	0.87
J115104.55+001454.2	3	12.23	42.99	0.3	1.59	-0.22
J115705.93+010731.8	4	11.59	59.98	0.1	1.26	1.03
J115723.03+002913.9	3	12.10	51.37	0.4	1.34	-0.16
J115736.61+010826.7	1	-	15.60	-	-	-
J115846.24-012757.0	26	13.76	73.90	0.8	2.53	1.18
J120018.00+001741.9	2	9.12	26.65	0.2	0.70	0.00
J120446.29-000055.3	1	-	7.20	-	-	-
J120803.96+004151.2	1	-	6.81	-	-	-
J121017.87-003104.4	1	-	38.15	-	-	-
J121520.15-002352.9	3	10.41	15.29	0.1	0.74	-1.10
J121552.50+002402.5	1	-	25.98	-	-	-
J121948.26-005231.6	2	12.71	63.01	0.2	0.75	-0.74
J122337.49-002821.3	1	-	16.56	-	-	-
J125440.02+322201.2	7	13.40	53.04	0.5	2.27	1.86
J125453.68+282501.1	5	13.20	23.35	0.2	0.57	-1.23
J125606.09+274041.1	680	15.20	144.04	0.8	1.16	-2.37
J125610.97+280947.4	1	-	6.66	-	-	-
J125809.22+284230.8	680	15.20	475.95	1.6	2.37	0.80
J125818.23+290743.6	680	15.20	201.18	2.5	3.68	1.13
J125837.28+271035.8	680	15.20	572.40	1.4	2.01	0.87
J125902.07+280656.3	2	11.28	17.79	0.1	0.74	-0.67
J130125.07+284038.0	3	12.81	20.05	0.1	0.69	0.99
J130305.93+263152.0	1	-	5.06	-	-	-
J130316.24+280149.4	680	15.20	528.62	1.5	2.24	-1.01

Note: Δ is the velocity of the galaxy relative to the group center.

Table 4.6 Environmental Properties of JINGLE Galaxies (continued)

SDSS (ID)	Ngal (Num)	M_{halo} (log $M_{\odot}$)	Env. Den. at 1 h^{-1} Mpc (-)	R (Mpc)	R/R_{vir} (-)	Δ/v_{vir} (-)
J130329.08+263301.7	2	10.66	15.31	0.2	0.72	0.70
J130428.23+264019.0	3	10.66	34.48	0.4	1.23	0.96
J130615.12+252737.9	5	12.91	28.33	0.2	0.96	-0.22
J130636.39+275222.6	3	12.49	45.57	0.3	1.16	1.12
J130713.20+280249.0	7	13.12	31.10	0.2	1.10	-0.12
J130801.65+264555.3	1	-	22.80	-	-	-
J130802.57+271840.0	1	-	2.78	-	-	-
J130851.54+283745.4	7	13.32	35.32	0.4	1.41	-1.02
J130855.07+290226.7	1	-	16.09	-	-	-
J130945.77+283716.3	7	13.32	26.09	0.3	1.17	-1.19
J131047.64+294235.6	1	-	14.15	-	-	-
J131101.71+293442.0	3	12.62	78.80	0.2	1.26	0.60
J131239.04+340354.5	11	13.39	113.70	0.3	1.42	-0.80
J131258.27+311531.0	1	-	6.63	-	-	-
J131313.45+335903.9	11	13.39	126.81	0.1	0.47	0.84
J131508.21+302413.5	3	12.72	23.08	0.4	1.15	-0.11
J131526.03+330926.0	1	-	2.79	-	-	-
J131551.16+263320.4	1	-	9.78	-	-	-
J131615.95+301552.2	3	12.49	85.86	0.1	0.54	-0.11
J131620.53+304042.0	16	13.33	74.96	0.3	1.10	-0.43
J131721.28+310334.1	16	13.33	76.70	0.4	1.42	-1.06
J131804.10+335118.2	1	-	3.45	-	-	-
J131958.31+281449.3	2	11.32	11.65	0.1	0.72	0.68
J131958.56+340209.8	1	-	4.38	-	-	-
J132014.23+312132.1	24	14.11	312.16	0.3	0.96	0.21
J132035.40+340821.7	2	11.68	22.24	0.0	0.72	-0.73
J132115.52+333732.0	3	12.42	45.76	0.2	0.87	-0.38
J132122.24+255703.6	1	-	14.96	-	-	-
J132134.91+261816.8	1	-	3.26	-	-	-
J132151.16+322612.6	3	11.75	21.03	0.1	1.81	-0.77
J132251.07+314934.3	1	-	9.71	-	-	-
J132320.14+320349.0	3	13.06	35.57	0.1	1.31	0.19
J132359.95+305556.7	5	13.25	60.11	0.1	0.74	-0.98
J132443.68+323225.0	9	13.37	180.84	0.2	1.48	-0.14
J132509.71+320051.9	1	-	26.57	-	-	-
J132515.15+324016.1	9	13.37	164.48	0.4	3.59	-0.08

Note: Δ is the velocity of the galaxy relative to the group center.

Table 4.7 Environmental Properties of JINGLE Galaxies (continued)

SDSS (ID)	Ngal (Num)	M_{halo} (log $M_\odot$)	Env. Den. at 1 h^{-1} Mpc (-)	R (Mpc)	R/R_{vir} (-)	Δ/v_{vir} (-)
J132609.41+264612.2	3	11.90	46.04	0.2	0.71	-0.69
J132638.85+270223.4	2	12.05	16.16	0.2	0.72	-0.71
J132643.48+303024.0	1	-	11.00	-	-	-
J132731.45+342008.2	13	13.47	100.20	0.2	1.75	1.23
J132838.16+333618.3	1	-	9.96	-	-	-
J132856.70+325244.0	1	-	24.73	-	-	-
J133213.68+265659.9	2	12.26	24.44	0.2	0.75	-0.72
J133306.57+330903.7	7	13.03	132.03	0.1	1.20	0.78
J133316.29+343213.2	88	14.12	227.99	0.8	1.22	-0.24
J133451.23+340319.8	88	14.12	146.82	0.4	0.62	0.65
J133457.27+340238.7	88	14.12	181.51	0.4	0.63	-1.05
J133538.40+255230.9	2	11.92	32.84	0.1	0.73	-0.68
J133619.63+332524.3	88	14.12	151.89	1.7	2.77	0.47
J133931.82+312657.8	3	12.84	44.68	0.2	1.01	0.80
J133933.35+295949.4	6	12.84	73.62	0.5	3.57	0.66
J133944.15+274635.2	2	11.41	22.44	0.1	0.74	0.78
J134017.95+262058.3	2	11.56	42.27	0.1	0.73	-0.73
J134018.24+320911.2	2	12.44	14.49	0.1	0.74	0.73
J134113.58+302327.4	6	12.44	120.53	0.2	2.11	-0.52
J134145.21+270016.9	4	11.86	55.10	0.1	0.45	0.61
J134229.72+341303.4	1	-	8.06	-	-	-
J134308.83+302015.8	3	12.09	78.26	0.2	0.65	-0.33
J141330.00+001109.0	1	-	9.10	-	-	-
J141605.26-011537.3	7	12.87	107.96	0.2	0.70	0.41
J141628.95-004437.9	2	11.52	49.30	0.2	0.77	0.77
J141658.36+013825.5	2	12.05	22.28	0.2	0.73	0.73
J142227.60+000332.5	1	-	12.75	-	-	-
J142433.17+011038.3	5	12.81	110.05	0.0	0.43	0.47
J142653.06+005746.3	4	12.24	63.89	0.3	1.80	1.48
J143042.33+015253.2	3	12.24	43.46	0.2	1.40	-0.87
J143643.42-003401.3	3	12.97	23.39	0.2	1.18	-1.14
J143816.50-002059.0	2	11.29	35.09	0.1	0.75	-0.73
J143842.98-000027.8	2	10.96	16.33	0.3	0.75	0.78
J144256.63-004839.0	1	-	3.56	-	-	-
J144307.78+010600.0	4	12.49	63.90	0.5	1.82	1.41
J144322.25+010553.2	1	-	20.57	-	-	-

Note: Δ is the velocity of the galaxy relative to the group center.

Bibliography

Ahn C. P., et al., 2014, ApJS, 211, 17

Bekki K., 2014, MNRAS, 438, 444

Bigiel F., Leroy A., Walter F., Brinks E., de Blok W. J. G., Madore B., Thornley M. D., 2008, AJ, 136, 2846

Blanton M. R., Moustakas J., 2009, ARA&A, 47, 159

Bolatto A. D., Wolfire M., Leroy A. K., 2013, ARA&A, 51, 207

Boselli A., Cortese L., Boquien M., Boissier S., Catinella B., Gavazzi G., Lagos C., Saintonge A., 2014, A&A, 564, A67

Butcher H., Oemler Jr. A., 1984, ApJ, 285, 426

Cayatte V., van Gorkom J. H., Balkowski C., Kotanyi C., 1990, AJ, 100, 604

Cayatte V., Kotanyi C., Balkowski C., van Gorkom J. H., 1994, AJ, 107, 1003

Chabrier G., 2003, PASP, 115, 763

Chamaraux P., Balkowski C., Gerard E., 1980, A&A, 83, 38

Corbelli E., et al., 2012, A&A, 542, A32

De Vis P., et al., 2017, preprint, (arXiv:1705.02340)

Downes D., Solomon P. M., 1998, ApJ, 507, 615

Genzel R., et al., 2010, MNRAS, 407, 2091

Giovanelli R., et al., 2005, AJ, 130, 2598

Gunn J. E., Gott III J. R., 1972, ApJ, 176, 1

Haines C. P., et al., 2012, ApJ, 754, 97

Haines C. P., et al., 2013, ApJ, 775, 126

Haynes M. P., et al., 2011, AJ, 142, 170

Holland W. S., et al., 2013, MNRAS, 430, 2513

Kenney J. D. P., Young J. S., 1989, ApJ, 344, 171

Lee J., 2017, ApJ, 839, 29

Leroy A. K., Walter F., Brinks E., Bigiel F., de Blok W. J. G., Madore B., Thornley M. D., 2008, AJ, 136, 2782

Lisenfeld U., et al., 2011, A&A, 534, A102

Martinez-Badenes V., Lisenfeld U., Espada D., Verdes-Montenegro L., García-Burillo S., Leon S., Sulentic J., Yun M. S., 2012, A&A, 540, A96

Mok A., et al., 2016, MNRAS, 456, 4384

Mok A., Wilson C. D., Knapen J. H., Sánchez-Gallego J. R., Brinks E., Rosolowsky E., 2017, MNRAS, 467, 4282

Moore B., Katz N., Lake G., Dressler A., Oemler A., 1996, Nature, 379, 613

Moore B., Lake G., Katz N., 1998, ApJ, 495, 139

Muzzin A., et al., 2014, ApJ, 796, 65

Navarro J. F., Frenk C. S., White S. D. M., 1997, ApJ, 490, 493

Noble A. G., Webb T. M. A., Yee H. K. C., Muzzin A., Wilson G., van der Burg R. F. J., Balogh M. L., Shupe D. L., 2016, ApJ, 816, 48

Peng Y.-j., et al., 2010, ApJ, 721, 193

Rigby E. E., et al., 2011, MNRAS, 415, 2336

Rosolowsky E., Leroy A. K., Usero A., Loeppky J., Walter F., Wilson C., Heracles Team N. T., 2015, in American Astronomical Society Meeting Abstracts. p. 141.25

Saintonge A., et al., 2011a, MNRAS, 415, 32

Saintonge A., et al., 2011b, MNRAS, 415, 61

Scoville N., et al., 2014, ApJ, 783, 84

Scoville N., et al., 2016, ApJ, 820, 83

Springob C. M., Haynes M. P., Giovanelli R., Kent B. R., 2005, ApJS, 160, 149

Tempel E., Tago E., Liivamägi L. J., 2012, A&A, 540, A106

Tempel E., et al., 2014, A&A, 566, A1

Thomas H. C., Alexander P., Clemens M. S., Green D. A., Dunne L., Eales S., 2004, MNRAS, 351, 362

Tonnesen S., Bryan G. L., 2009, ApJ, 694, 789

Wilson C. D., et al., 2012, MNRAS, 424, 3050

Yang X., Mo H. J., van den Bosch F. C., Pasquali A., Li C., Barden M., 2007, ApJ, 671, 153

da Cunha E., Charlot S., Elbaz D., 2008, MNRAS, 388, 1595

Chapter 5

Summary and Future Work

I present in this thesis an environmental analysis of the gas-rich, star-forming galaxies in the NGLS and JINGLE datasets. This work focuses on two important areas that have not been fully explored previously in the literature: the effects of the cluster environment on gas-rich galaxies, such as those in an early stage of infall, and constraining the star-formation and molecular gas properties for galaxies across a large range of environments.

In Chapter 2, I find an increase in the molecular gas fraction of the Virgo spirals in the H I-selected NGLS sample, compared to the non-Virgo sample (Mok et al., 2016). I also find an increase in the H_2-to-H I ratio, which indicates that these environmental effects are more efficient at removing the more diffuse and extended atomic gas compared to the centrally located molecular gas. Combined with Hα-derived star formation rates, there is an increase in the molecular gas depletion time for Virgo spirals compared to non-Virgo spirals. Finally, I find similar relationships between molecular gas and star formation rate, as well as between the molecular gas depletion time and stellar mass found in previous similar studies (e.g Saintonge et al., 2011b).

In Chapter 3, I measure the molecular gas, atomic gas, and star formation radial profiles for NGLS galaxies (Mok et al., 2017). I find that the molecular gas is enhanced near the centre for Virgo galaxies. In addition, Virgo galaxies have steeper total gas profiles (atomic + molecular gas), giving support to the theory that moderate ram pressure stripping can aid in the creation of high density gas near the centre while removing low density gas in the outskirts. I also find no trends in the radial profile of the molecular gas depletion time, but the overall increase in the mean molecular gas depletion time for Virgo galaxies is still present.

The main results from the analysis of the NGLS sample show the importance of using a gas-rich sample of spiral galaxies to look for differences between environments. The gas-rich criteria selects objects which are recently infalling into the group or cluster environment. Thus, the NGLS sample measures the environmental effects on a galaxy with a large amount of cold gas, instead of fully stripped, older infalling galaxies. I find similar results with both the integrated and resolved analysis, such as an increase in the molecular gas to atomic gas fraction and the molecular gas depletion time in the Virgo compared to the non-Virgo spirals. I suggest that moderate ram pressure stripping may be the cause of these variations, a scenario which is also seen in recent simulations of disk galaxies (Bekki, 2014; Tonnesen & Bryan, 2009).

One major difficulty with interpreting environmental variations is the varied sample selections used by past surveys. For example, the K-band (stellar mass) selected Herschel Reference Survey (HRS) and Herschel Virgo Survey (HeViCS) show many highly deficient objects in both H I and H_2 and a reduction in the molecular gas fraction for cluster galaxies (Corbelli et al., 2012; Boselli et al., 2014b). As stated previously, the main difference between our results appears to be in the sample selection; the NGLS does not have any heavily stripped, older cluster galaxies. Follow-up work can be performed to test the effects of an H I limit on the HRS and HeViCS samples or to combine these samples in a consistent manner.

A second difficulty lies in comparing radial profiles to previous surveys such as the HERA CO-Line Extragalactic Survey (HERACLES) (Leroy et al., 2008, 2013). One factor is that HERACLES is selected from a sample of interesting nearby galaxies, whereas the NGLS is a statistical sample selected based on the galaxy's H I-flux. A second factor lies in the CO line chosen. For example, the CO $J = 3-2$ line may not be tracing the same component of the ISM as the CO $J = 2-1$ and $J = 1-0$ lines, even though we have tried to compensate by using a CO $J = 3-2$ to CO $J = 1-0$ line ratio. A third reason may be the data reduction technique used by the NGLS, which results in many galaxies with large areas of blank pixels in their maps. I have attempted to correct for this using various techniques discussed in Mok et al. (2017), but more tests are needed and improvements can be made. In the future, I hope to compare these radial provides from the NGLS to other large, representative, and resolved surveys of gas-rich galaxies, such as the CALIFA-EDGE survey (Bolatto et al., 2017), once their data are available.

Finally, it remains difficult to disentangle the effects of environment from internal factors and determine which environment process (starvation, ram-pressure stripping, galaxy interactions) is the dominant one for the NGLS sample. I will discuss some methods of doing so in the section on future work.

In Chapter 4, I analyze the initial Data Release 1 (DR1) from the first half of the JINGLE sample of Herschel-selected galaxies. I find that the molecular gas mass estimates using the 850 μm continuum and the CO $J = 2-1$ line are well correlated. There is also a nearly linear correlation between the molecular gas mass estimated from the 850 μm continuum data and star formation rate. The molecular gas depletion time and the H_2-to-H I ratio shows no significant dependence on the galaxy's stellar mass and therefore appear to be potentially good tracers of environmental effects.

I also match the JINGLE sample with the group catalogue from Tempel et al. (2014) and measure parameters such as the host halo masses, the local environment density, and the location of galaxies in a phase-space diagram. No significant environmental variation is found for the DR1 JINGLE galaxies, but I hope to use this framework to analyze the full JINGLE sample once it is available, along with more accurate mass estimates from the full dust SED-fitting process. The larger sample size will also permit division of JINGLE galaxies into more categories, such as separating out central and satellite galaxies or creating a isolated sub-sample. Furthermore, the phase-space analysis can be divided up into more precise regions. For example, the environmental analysis in Noble et al. (2016) using phase-space diagrams included five different regions, such as central, intermediate, recently accreted, infalling, and field.

On the other hand, the lack of a significant environment signature using the current DR1 sample suggests that galaxies on the star-forming main sequence may be similar to each other in different environments. This result presents a different view of the effects of environment, compared to the NGLS results discussed above. Sample selection is once again an important factor. The Herschel 250 μm and 350 μm selected nature of the JINGLE survey means that all the JINGLE galaxies are on the star-forming main sequence, as opposed to the H I-selected NGLS sample. The natural next step is to compare only the main sequence galaxies from the NGLS, COLD GASS, and JINGLE surveys. In addition, potential differences in the scaling relations, such as the relationship between the molecular gas depletion time and stellar mass found in the JINGLE sample compared to the the COLD GASS survey, can be explored once the full sample is collected and the dust SED-fitting is complete.

5.1 Future Work

The most natural extension to this work is to incorporate the upcoming observations from the full JINGLE survey, which will double the number of galaxies with SCUBA-2 and RxA observations. The full sample will allow a determination of statistical trends with greater certainty. Furthermore, future Arcebio H I measurements will allow measurements of the atomic gas fraction and the important H_2-to-H I ratio for all of the JINGLE galaxies. In addition, a recently accepted JINGLE extension proposal using the JCMT will provide observations of 'green valley' galaxies. If no environment variations can be found in the full JINGLE sample for galaxies on the star-forming main sequence, then these transitioning objects may be better candidates.

Another natural extension is the creation of a theoretical framework to study the different environmental mechanisms. For example, to determine if ram-pressure stripping is the primary mechanism responsible for the change in the atomic-to-molecular gas ratios and the radial distribution of the gas, I can model its effects on the NGLS sample, taking into account the density of the Intercluster Medium (ICM) and the velocity of the galaxies moving through the cluster. Another opportunity is the use of the velocity information, including rotation curves and line widths. For example, one idea used to explain the difference in the molecular gas depletion time between Virgo and non-Virgo galaxies from Mok et al. (2016) is turbulent pressure, which can be tested using the velocity data. The H I data can also be used to test for the effects of interactions and close neighbours, since it is available to much larger radii, potentially allowing for a differentiation from the ram-pressure stripping scenario.

Next, I have written other observing proposals to further explore the effects of environment in a sample of gas-rich galaxies. One successful JCMT proposal obtained data for the CO $J = 3-2$ line for the H I-rich galaxies in the Fornax Cluster using HARP. I can perform the same analysis on the Fornax Cluster galaxies as done for the NGLS sample. Another successful JCMT proposal will observe the remaining galaxies from the VLA Imaging of Virgo in Atomic gas (VIVA) survey (Chung et al., 2009) without existing HARP CO $J = 3-2$ observations. The combination will allow me to perform analysis on the resolved maps and measure the radial profiles for a larger sample of galaxies, in order to determine if my results with the NGLS sample are verified.

There is also the potential to combine many of the samples of galaxies already collected, such as the NGLS (Wilson et al., 2012), HRS (Boselli et al., 2014a), COLD GASS (Saintonge et al., 2011a), HERACLES (Leroy et al., 2008), JINGLE, and CALIFA-EDGE (Bolatto et al., 2017). I would need to first homogenize the samples, taking into account differences in sensitivity, sample selection, spatial resolution, CO line chosen, and other factors. Once that process is complete, it is possible to create a large (> 1000) statistical sample. Environmental analysis with large H I surveys such as ALFALFA have opened up a new window into the effects of environment on atomic gas properties. Adding H_2 data to that analysis will improve the analysis greatly, especially when comparing to measurements of the star formation rate for these galaxies.

Another possible extension is to look at the redshift evolution of the ISM and star formation properties inside groups and clusters. There has been a great reduction in the cosmic star formation rate density since $z \sim 2$ (Madau & Dickinson, 2014), which has coincided with the buildup of the clusters that we see in the present day. Looking at the gas fraction and star formation efficiency of cluster and group galaxies as a function of redshift will help us understand the time-scale and effectiveness of various star-formation quenching mechanisms. The use of instruments like ALMA, combined with dust continuum measurements, allow efficient observations for a large sample of high-redshift galaxies and in a reasonable amount of time (Scoville et al., 2016).

Finally, while it is important to study the scaling relationships and radial profiles for cluster and non-cluster galaxies, star formation typically happens on much smaller scales. For example, inside the Milky Way and in nearby galaxies, we can observe filaments, giant molecular clouds, and the formation of protostars and star clusters. As astronomers build up the catalogue of galaxies with high resolution molecular gas data, it may be worthwhile to compare these small-scale structures for galaxies in different environments and determine if there are any significant variations in their properties.

Bibliography

Bekki K., 2014, MNRAS, 438, 444

Bolatto A. D., et al., 2017, preprint, (arXiv:1704.02504)

Boselli A., Cortese L., Boquien M., 2014a, A&A, 564, A65

Boselli A., Cortese L., Boquien M., Boissier S., Catinella B., Gavazzi G., Lagos C., Saintonge A., 2014b, A&A, 564, A67

Chung A., van Gorkom J. H., Kenney J. D. P., Crowl H., Vollmer B., 2009, AJ, 138, 1741

Corbelli E., et al., 2012, A&A, 542, A32

Leroy A. K., Walter F., Brinks E., Bigiel F., de Blok W. J. G., Madore B., Thornley M. D., 2008, AJ, 136, 2782

Leroy A. K., et al., 2013, AJ, 146, 19

Madau P., Dickinson M., 2014, ARA&A, 52, 415

Mok A., et al., 2016, MNRAS, 456, 4384

Mok A., Wilson C. D., Knapen J. H., Sánchez-Gallego J. R., Brinks E., Rosolowsky E., 2017, MNRAS, 467, 4282

Noble A. G., Webb T. M. A., Yee H. K. C., Muzzin A., Wilson G., van der Burg R. F. J., Balogh M. L., Shupe D. L., 2016, ApJ, 816, 48

Saintonge A., et al., 2011a, MNRAS, 415, 32

Saintonge A., et al., 2011b, MNRAS, 415, 61

Scoville N., et al., 2016, ApJ, 820, 83

Tempel E., et al., 2014, A&A, 566, A1

Tonnesen S., Bryan G. L., 2009, ApJ, 694, 789

Wilson C. D., et al., 2012, MNRAS, 424, 3050

This page intentionally left blank.